UNIVERSITÀ DEGLI STUDI DI ROMA
"TOR VERGATA"

Facoltà di Scienze Matematiche, Fisiche e Naturali

Dipartimento di Fisica

Minimum Bias Measurements with the ATLAS experiment at LHC: strangeness production and $\overline{\Lambda^0}$ to Λ^0 particle ratio

Roberto Di Nardo

Dottorato in Fisica, XXIII ciclo

Tutore:

Prof.ssa ANNA DI CIACCIO

Coordinatore:

Prof. PIERGIORGIO PICOZZA

ANNO ACCADEMICO 2009-2010

To my family

Introduction

In November 2009 the Large Hadron Collider started to deliver proton-proton collisions opening a new era on high energy physics. The LHC is the largest accelerator ever built and it is located at the European Organization for Nuclear Research (CERN) in Geneva. It is designed to reach the center of mass energy of 14 TeV at the luminosity of 10^{34} cm^{-2}s^{-1}. Four main experiments have been built in correspondence of the LHC interaction points: ALICE, ATLAS, CMS and LHCb.

By the end of 2009 the LHC has delivered to the ATLAS experiment 12μb^{-1} of collision data at the center of mass energy of 900 GeV. The accelerator has restarted the operation in March 2010 at the center of mass energy of $\sqrt{s}$ =7 TeV with the aim of of delivering, after the winter shutdown, up to 3 fb^{-1} of integrated luminosity to the ATLAS and CMS experiments by the end of 2011.

The physics goals of the LHC are very ambitious: further tests of the Standard Model of particle physics, understanding of the electroweak symmetry breaking mechanism and the possible discovery of the Higgs Boson; search for new physics beyond the Standard Model; the study of the CP violation in the B system.

In order to reach these goals, an optimal understanding of the detectors is required. At the LHC designed luminosity of 10^{34}cm^{-2}s^{-1}, every interesting rare signal and signature will be produced together with $\sim$ 23 soft interactions, therefore a good understanding of the bulk of the collisions is needed. In particular it is important to characterize the soft collisions called also minimum

bias events with the study of the track multiplicity, their momentum spectra, the yields of known particles, tuning at the same time the Monte Carlo generators that describe the soft proton-proton collisions.
The understanding of the basic properties of minimum bias events at the LHC energies is the subject of this thesis. In particular I have studied the identification and reconstruction of K^0_s, Λ^0 and $\overline{\Lambda^0}$ in the ATLAS experiment, showing the very good tracking performance of the Inner Detector already in the first period of data taking, a necessary step for the measurement of the yields of these particles. The final goal of the thesis is the measurement of the $\overline{\Lambda^0}$ to Λ^0 production ratio versus pseudorapidity, rapidity and transverse momentum. The importance of this measurement is related to the understanding of the transfer of baryon number from the beam to the relatively central rapidity range of the measured acceptance.

In the first chapter I give a short description of the Large Hadron Collider and of the ATLAS experiment: I present the main characteristics of the magnet system, the Inner Detector, the electromagnetic and the hadronic calorimeters, the Muon Spectrometer and the trigger chain. In the second chapter I describe the main features of the Minimum bias events, the Monte Carlo generators commonly used to model soft collisions and the charged particle distributions measured with ATLAS at the energies of $\sqrt{s} = 900$ GeV and $\sqrt{s} = 7$ TeV. In the third chapter I present in details the analysis steps to reconstruct the K^0_s meson and Λ^0 and $\overline{\Lambda^0}$ baryons with $190\mu b^{-1}$ of data collected. The measurements of the properties of these particles may be used to tune different Monte Carlo generators that model minimum bias events and have already allowed a deeper understanding of the tracking performance of the ATLAS Inner Detector. In the fourth chapter I describe the theoretical background on the baryon number transport in hadronic interactions and the results from other experiments. Finally in the fifth chapter I present the measurement of the $\overline{\Lambda^0}$ to Λ^0 production ratio with a detailed description of all the systematics uncertainties contributing to it.

Contents

Chapter 1

The Large Hadron Collider and the ATLAS Experiment

1.1 The Large Hadron Collider

The Large Hadron Collider (LHC) [1] is a two ring superconducting hadron collider installed in the existing LEP [2] machine tunnel at CERN in Geneva. It is 26.7 km long and it is located between 45 m and 170 m below the ground surface. Two transfer tunnels connect the LHC to the CERN accelerator complex that is used as injector. In Figure 1.1 is shown a schematic view of the LHC and the CERN accelerator complex. Aim of this accelerator is to provide proton-proton collisions at center of mass up to the energies of 14 TeV in order to study the still open issues of the Standard Model and eventually to reveal the physics beyond it. The number of events per second generated in the LHC collisions is related to the cross section of the event under study, σ_{event}, by the following relationship

$$N_{event} = L\sigma_{event} \tag{1.1.1}$$

with L representing the machine luminosity and depending only on the beam parameters. For a Gaussian beam distribution, it can be written as:

$$L = \frac{N_b n_b f_{rev} \gamma_r}{4\pi\epsilon_n \beta^*} F \tag{1.1.2}$$

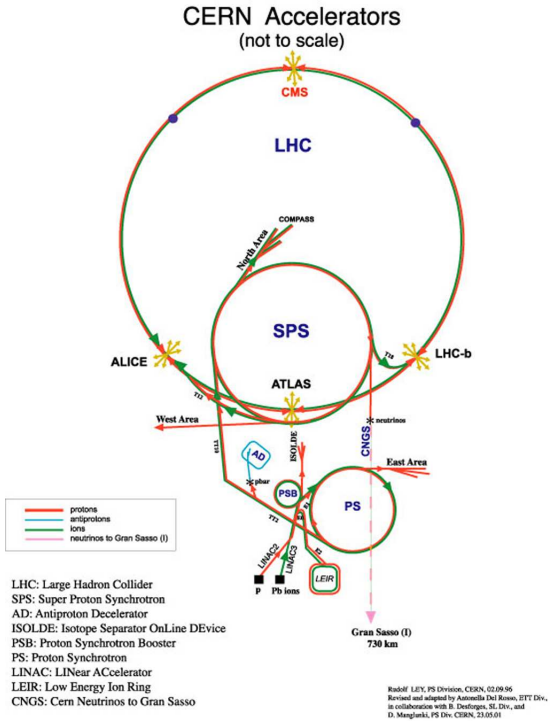

Figure 1.1: Schematic view of the Large Hadron Collider and the CERN accelerator complex

where N_b is the number of particle per bunch, n_b is the number of bunches per beam, f_{rev} the revolution frequency, γ_r the relativistic gamma factor, ϵ_n the normalized transverse beam emittance, β^* the beta function at the interaction point, and F is the geometric luminosity reduction factor due to the crossing angle at the interaction point. Having high beam energies and high beam intensities is the essential requirement for the exploration of rare events in the LHC collisions. The general LHC design parameters are reported in table 1.1. In order to bend the two proton beam trajectories 1232 dipoles are used . An LHC dipole has a length of 14.3 m and contains superconducting magnets which operate at a temperature of 1.9 K. These dipoles provide a magnetic field of 0.535 T in the injection stage (beam energy 450 GeV) up to 8.33 T for the nominal 7 TeV energy per beam corresponding to an average magnetic field of 5.3T along the 27 km . The beam acceleration and energy loss compensation

LHC General Parameters	
Energy at collision	7 TeV
Energy at injection	450 GeV
Dipole field at 7 TeV	8.33 T
Coil inner diameter	56 mm
Luminosity	10^{34} cm^{-2}s^{-1}
DC beam current	0.56 A
Bunch spacing	7.48 m
Bunch separation	24.95 ns
Number of particles per bunch	1.1*10^{11}
Normalized transverse emittance (r.m.s.)	3.75 μm
Total crossing angle	300 μrad
Luminosity lifetime	10 h
Energy loss per turn	7 keV
Critical photon energy	44.1 eV
Total radiated power per beam	3.8 kW
Stored energy per beam	350 MJ
Filling time per ring	4.3 min

Table 1.1: General LHC design parameters

is done using eight *RF cavities* that produce a field of 5.5 MV/m.
The experiments that operate along the LHC ring are:

- **ATLAS (A Toroidal LHC Apparatus)** [3] and **CMS (Compact Muon Solenoid)**[4] are two general purpose experiment that will cover the wide range of physics that can be studied at LHC. The main goal for these two experiments is to search for the Higgs boson and the physics beyond the Standard Model, like evidence for extra dimension models or the discovery of new heavy particle postulated for instance in supersymmetric theories.

- **LHCb (Large Hadron Collider beauty experiment)** [5] is an experiment that, using a lower luminosity at the interaction point ($L = 10^{32}$ cm^{-2} s^{-1}), will study the CP-symmetry violation in the heavy b-quark system.

- **ALICE (A Large Ion Collier Experiment)** [6] is the LHC experiment dedicated to the heavy ion physics and it is designed to study the phase transition to the quark-gluon plasma. For this kind of studies, LHC will provide lead-lead ion collisions with a peak luminosity of $L = 2 \times 10^{27}$ cm^{-2} s^{-1}.

- **TOTEM (TOTal Elastic and diffractive cross-section Measurement)** [7] measures the total proton proton cross-section, elastic scattering, and diffractive processes. This detector is placed near the CMS experiment interaction point.

- **LHCf (Large Hadron Collider forward experiment)** [8] will measure the forward particles created during the LHC collisions in order to provide a better understanding of high-energy cosmic rays. This detector is located close to the ATLAS experiment interaction point.

1.1.1 LHC startup and first collisions at $\sqrt{s} = 900$ GeV and at $\sqrt{s} = 7$ TeV

The LHC successfully started its operation on 10th September 2008 when a beam with the 450 GeV injection energy made a complete turn of the entire LHC ring in less than one hour after the first injection. The same day also the second beam in the opposite direction successfully passed around the ring. In a few days of work, a lot of progresses were made: in two days the RF was captured and the first circulating stable beam was achieved. Figure 1.2 shows the beam monitor image of the first bunch which made the first complete LHC round and the intensity profile of another bunches injected later on in its ∼300 turns. On 19th September 2008 an accident occurred during the 5 TeV magnet

commissioning without beam in the LHC sector 34 [20]. To repair the damage that occurred in the machine the sector had to be warmed up and many dipoles were changed. For this reason the LHC operations were delayed until the late Summer of 2009. On 20 November 2009, bunches of protons circulated again in the LHC and three days after the first proton proton collisions at the injection energy of 450 GeV per beam were recorded by the four LHC experiments. The bunch intensity for these first collisions was of $\sim 3 \times 10^9$ protons ("pilot bunches"). Moreover, on November 30th 2009, the LHC became the world's highest-energy accelerator when both beams were successfully accelerated to 1.18 TeV per beam. Up to the end of 2009, an amount of $12\mu b^{-1}$ of integrated luminosity at $\sqrt{s} = 900$ GeV was collected by the ATLAS experiment with a peak luminosity of $7{\times}10^{26}cm^{-2}s^{-1}$. After the winter shutdown, the LHC restarted in 2010 providing the first collision at $\sqrt{s} = 7$ TeV on March 30th with the plan to run at this energy in 2010 and in 2011 with the target to provide ~ 1 fb^{-1} of data.

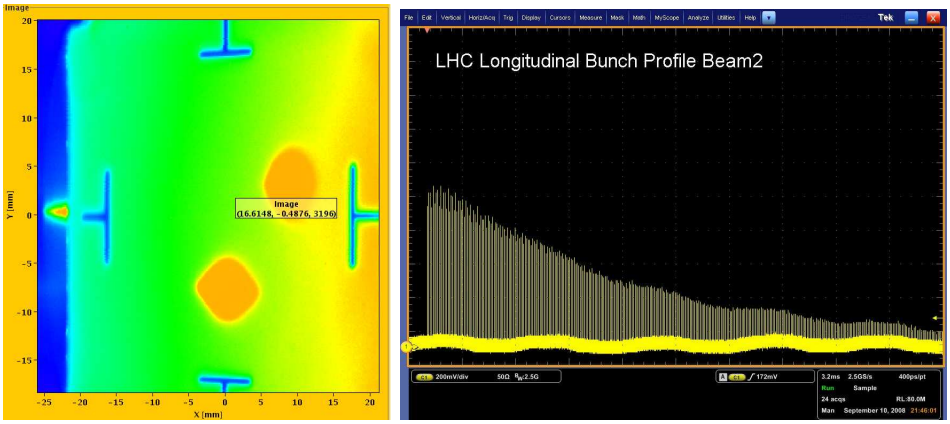

Figure 1.2: *(left)* LHC beam monitor image showing the first beam in LHC. The spots correspond to the position of the bunch at the injection and after one turn in the machine. *(right)* Longitudinal bunch profile for one of the first bunches injected in LHC.

1.2 The ATLAS Experiment

The design of the ATLAS experiment has been thought and realized in order to explore the high physics potential of the LHC proton-proton interactions. The main physics goals that ATLAS is aiming for are:

- A precise measurement of Standard Model parameters, with particular focus on the top quark properties. Measurement of production cross section of W and Z vector bosons at the new energy regime, precise measurement of the masses and the couplings and spin of the top quark could be achieved due to the very high production rates of the electroweak bosons as well as of the top quark. Moreover, a study of the CP violation using the B mesons decay could be also done.

- Exploration of the origin of the electroweak symmetry breaking mechanism: ATLAS will be able to discover or to exclude the Standard Model Higgs boson associated to the Higgs mechanism of the electroweak symmetry breaking up to its theoretical maximum mass of about 1 TeV.

- The search for physics beyond the Standard Model: the supersymmetric extensions of the Standard Model are of high interest because they give a possible dark matter candidate, the lightest supersymmetric particle. ATLAS will also search the existence of Extra Dimensions and the presence of new neutral (Z') and charged (W') vector bosons foreseen by the unification models that use extended gauge group (i.e. extra $U(1)$ in Kaluza-Klein Model)

Many of the processes mentioned have a small cross section and this is the reason why the LHC should provide a high luminosity. However, due to the inelastic proton-proton cross section that is of the order of $\sim$80 mb at 14 TeV, every interesting candidate event will be accompanied on average by 23 inelastic collisions at the design luminosity. So, the benchmark physics goals can be turned into a set of general requirements for the ATLAS experiment (and all the other LHC detectors) that can be summarized as follows:

- due to the high collision rate and the elevated number of particles created in the proton-proton interaction, the detectors should have a fast and radiation-hard electronics and a high granularity in order to reduce the effect of the overlapping events;
- an inner tracker with a good charged particle momentum resolution and reconstruction efficiency and a vertex detector close to the interaction point is necessary to perform an offline identification of τ leptons and b-jets observing secondary vertices;
- a performing electromagnetic calorimetry for electron and photon identification and energy measurement is needed;
- a hadronic calorimetry with a full coverage for an accurate jet and missing transverse energy measurement of fundamental importance in the study of supersymmetric events;
- a good muon identification and reconstruction in a wide range of their momentum is needed;
- an efficient trigger that is able to select only interesting events with a sufficient background rejection is mandatory.

In Figure 1.3 a drawing of the ATLAS experiment is shown: starting form the interaction point we find the inner detector, the magnet solenoid, the electromagnetic calorimeter, the hadronic calorimeter and the muon spectrometer immersed in the toroidal air-core magnetic system.
The ATLAS experiment uses a right-handed coordinate system. The origin of this coordinate system is centered to the nominal position of the interaction point. The beam direction defines the z-axis direction that have the same orientation of the counter-clock wise rotating beam while the x-y plane is transverse to the beam direction; the x-axis points from the interaction point towards the center of the LHC ring; the y-axis points upwards. The azimuthal angle ϕ is measured from positive x-axis in the clockwise direction when looking at the positive z direction. The polar angle θ is measured from the positive

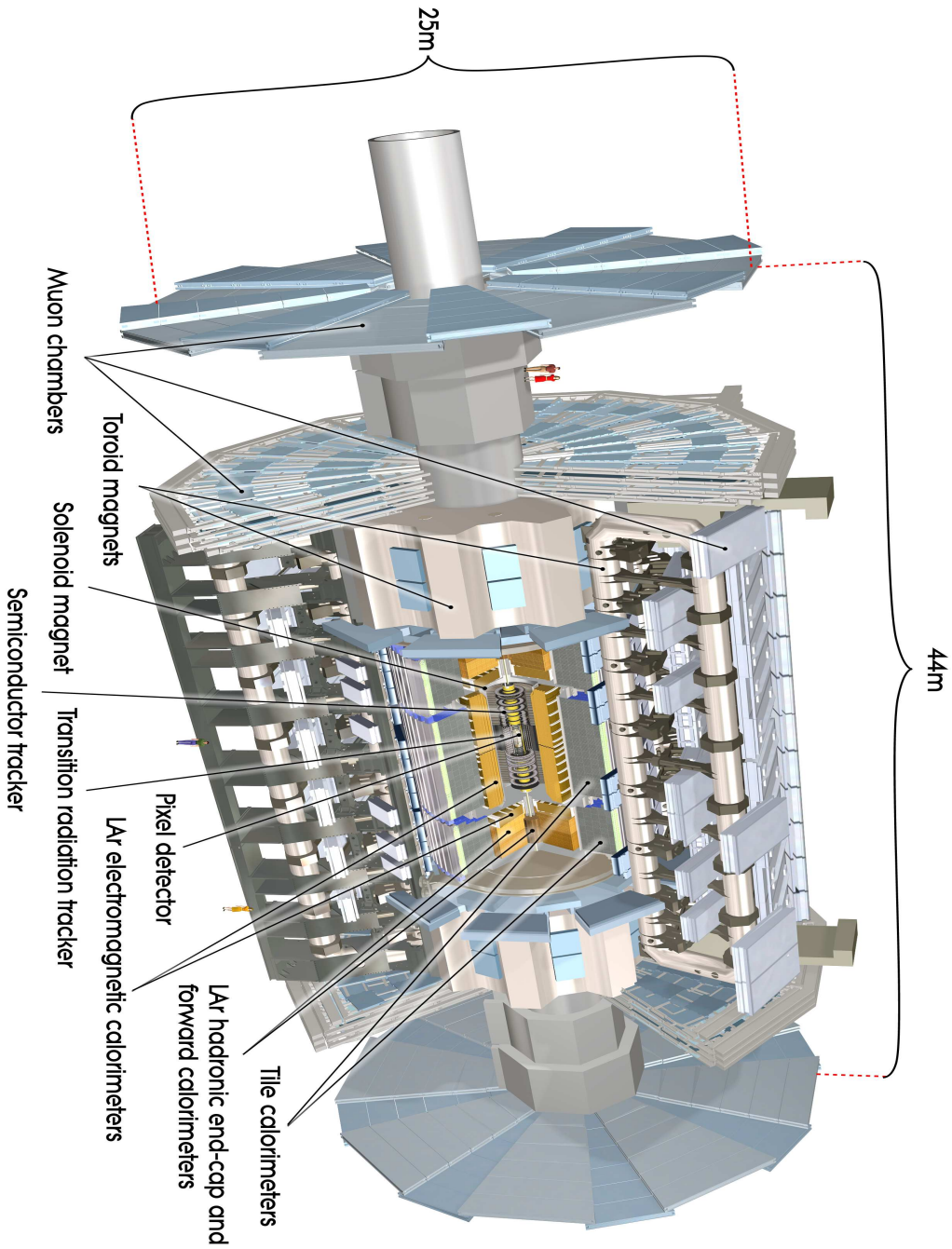

Figure 1.3: The ATLAS detector.

z-axis. The transverse momentum p_T of a particle corresponds to the momentum component orthogonal to the beam axis p_T =p$\cdot \sin\theta$. The pseudorapidity η is defined as

$$\eta = -\ln \tan\left(\frac{\theta}{2}\right) \tag{1.2.1}$$

In the following sections the different subsystems that compose the ATLAS detector are going to be described.

1.2.1 The Magnet System

Due to the huge dimension of the ATLAS experiment, the magnet system [9] is divided in four independent subsystem. In the Barrel region are located:

- a central superconducting solenoid [10] aligned with the beam axis that produces a 2 T magnetic field for the inner detector. The design of this magnet has been optimized to minimize the radiative thickness in front of the electromagnetic calorimeter resulting in a contribution of ~ 0.66 radiation lengths at normal incidence;
- an air-core toroidal magnet, composed by 8 coil (bobine) with an axial length of 25.3 m and a radial length of 11.3 m that can generate a toroidal magnetic field of 0.5 T for the muon detectors in the central region.

In the forward regions there are two other toroidal magnets that can generate a magnetic field up to 1 T for the muon detectors. Each end-cap toroid consists of a single cold mass built up from eight flat, square coil units and eight keystone wedges, bolted and glued together into a rigid structure to resist the Lorentz forces. These are located inside the toroidal magnet of the barrel region, in front of the two faces of the solenoid. A scheme of the ATLAS magnet system is shown in figure 1.4. In order to produce such intense magnetic field, the corresponding current needed is 20.5 kA for the toroidal magnets and 7.73 kA for the central solenoid. In order to work in the superconductive regime, all magnets are maintained inside a cryostat at a temperature of 4.5 K using liquid helium.

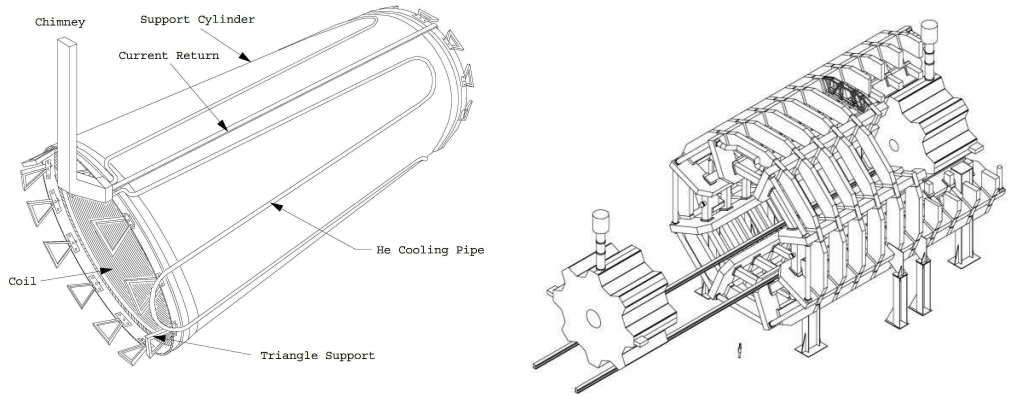

Figure 1.4: Scheme of the ATLAS magnet system: the central solenoid (left) and the toroidal magnet system (right). One of the end-cap toroid is shown in a shifted position with respect to the nominal one.

1.2.2 The Inner detector

The ATLAS inner detector [11, 12](shown in figure 1.5) is totally contained in the central solenoid that generates the 2T magnetic field oriented in the same direction of the beam axis, in order to bend the particles in the x-y plane. It also surrounds the LHC beam pipe that is fully contained in a radius of 36 mm.
The high track density that is expected for the collision events in the LHC imposes a high granularity for this detectors; in fact, at the LHC design luminosity of $L = 10^{34}$ cm^{-2} s^{-1}, $\sim$1000 particle will emerge from the interaction point every 25 ns. Moreover they have to work in a high-radiation environment. In order to satisfy this requirement with the minimum amount of material to limit the multiple scattering effect on the track momentum resolution, different kind of technologies are used: pixel and silicon microstrips (SCT) trackers together with the straw tubes of the transition radiation tracker (TRT).

To maintain an adequate noise performance after radiation damage, the silicon sensors is kept at low temperature (between -5° C and -10° C) with a cooling

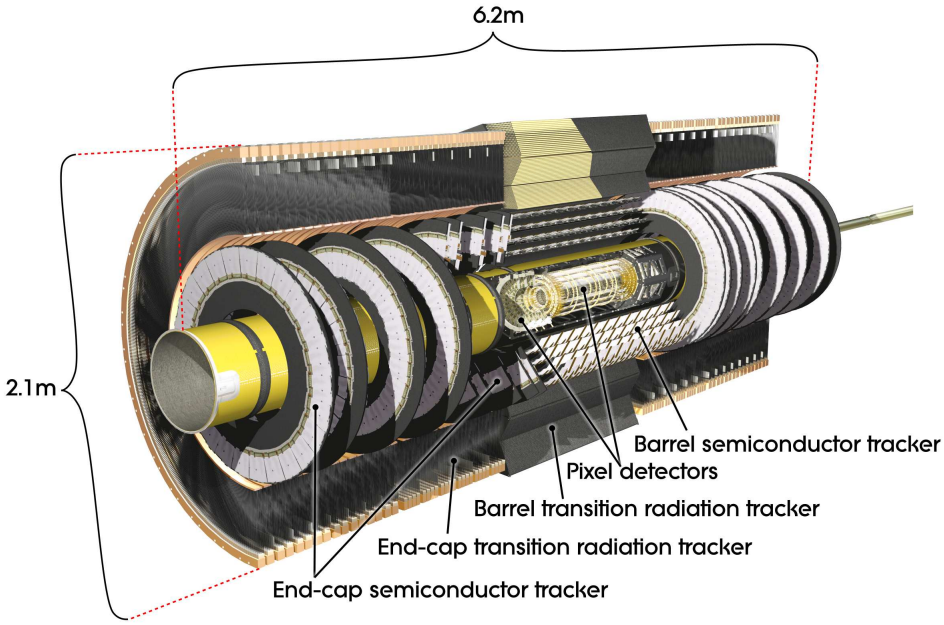

Figure 1.5: Scheme of the ATLAS inner detector

Item	**Intrinsic accuracy (μm)**	**Alignment tolerances (μm)**		
		(R)	**(z)**	**(R-ϕ)**
Pixel				
Layer-0	10 (R-ϕ) 115 (z)	10	20	7
Layer-1 and -2	10 (R-ϕ) 115 (z)	20	20	7
Disks	10 (R-ϕ) 115 (R)	20	100	7
SCT Barrel	17 (R-ϕ) 580 (z)	100	50	12
Disks	17 (R-ϕ) 580 (R)	50	200	12
TRT	130			30

Table 1.2: Intrinsic measurement accuracies and mechanical alignment tolerances for the Inner Detector sub-systems.

system that reaches the temperature of -25° C while the TRT operate at room temperature. The intrinsic measurement accuracy and mechanical alignment tolerances of the Inner Detector sub-system are summarized in table 1.2.

The Silicon Pixel detector

The Pixel Detector is composed by three cylindric layers (called ID layers 0-2) around the beam axis and by three disks on each of the forward region in order to cover the pseudorapidity range $|\eta| < 2.5$. The sensible area of the detector ($1.73\ \mathrm{m}^2$) is covered by 1744 identical modules, 1456 in the barrel and 288 in the endcaps. The barrel modules are arranged along carbon-fiber staves parallel to the beam axis and inclined by an azimuthal angle of 20°. This brings to a partial overlap of 200 μm of adjacent modules in each layer as shown in figure 1.6. A similar overlap is realized also in the Rz plane inclining the modules of 1.1° in order to ensure a full solid angle coverage with sensors. Each module is composed by a single silicon sensor with a sensitive area of $6.4 \times 60.8\ \mathrm{mm}^2$ and

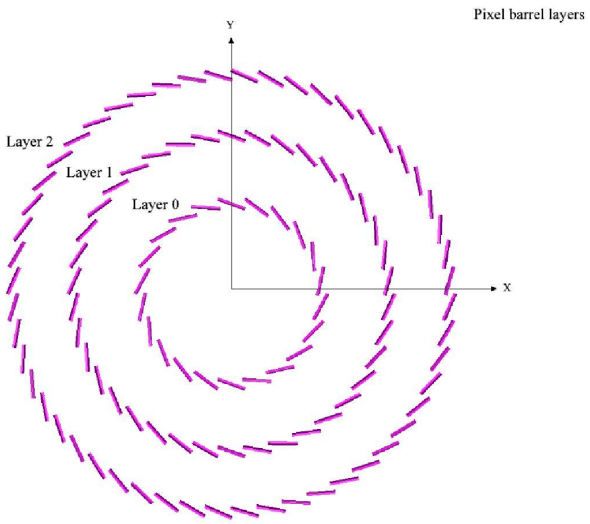

Figure 1.6: View of the Pixel modules of the barrel region in the transverse plane with respect to the beam axis.

250 μm of thickness. They have highly doped n^+ implants on a n^- substrate while the pn junction is located the back-side, with a multi-guard structure controlling the potential drop towards the cutting-edges. Moreover the single module does not exceed 1.2 X_0 and this low value is essential in order to minimize the multiple scattering effect on the particle trajectory. Each silicon wafer contains 47268 pixels which are connected to 16 front-end readout chips. A scheme of a pixel module is shown in figure 1.7.

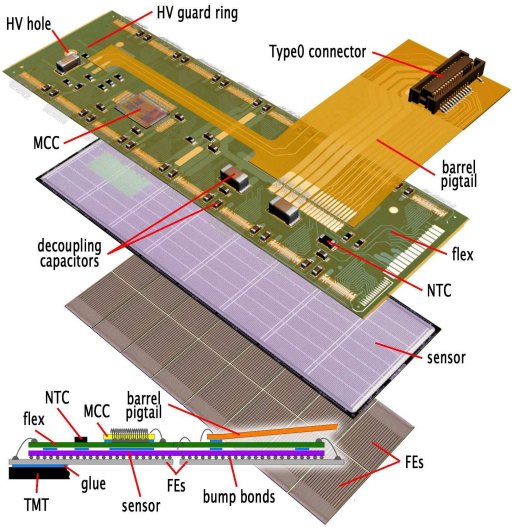

Figure 1.7: Schematic view of a barrel pixel module illustrating the major pixel hybrid and sensor elements.

The Silicon Microstrip detector

The SemiConductor Tracker (SCT) has been designed in order to provide precision track measurement in the intermediate radial region of the Inner Detector covering the pseudorapidity range $|\eta| < 2.5$. The SCT detector is composed by four cylindrical layers in the barrel region and nine discs in each side of the endcaps; both barrel layers and endcap discs are mounted on a carbon fiber structure. The total number of modules is 4088, 2112 in the barrel and 1976 in the endcaps. Also the SCT modules are mounted in the

barrel region in staves having a tilt angle of 11° corresponding to an overlap of 4 mm between the modules and a quite complex geometry is used for the SCT endcap. A single SCT module is made of two sensitive sensors based on strips that provide a position measurement in one dimension. Each side is formed by two wafers consisting of a high doped p^+ readout implants on a n^- silicon bulk with a thickness of 285μm and 768 parallel microstrips that have a rectangular shape and a width of 80 μm in the barrel region and a trapezoidal shape and a mean width of 80 μm in the endcaps. Moreover, both SCT module sides are glued together back-to-back at a 40 mrad stereo angle and the mechanical support structure, the TGP (*Thermal Pyrolytic Graphite*), ensure a high thermal conductivity between sensor and the cooling system as shown in figure 1.8. The readout is performed by means of 12 front-end chips and each chip reads 128 channels in order to read the signals from the 1536 microstrips of one module.

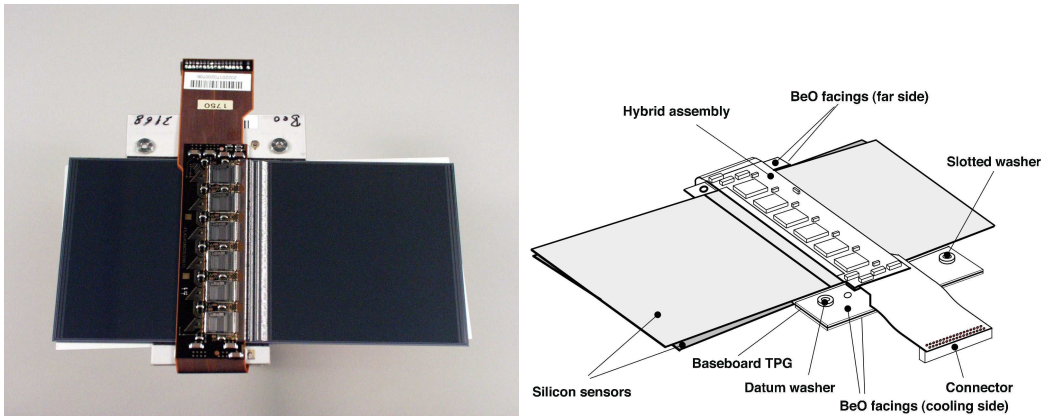

Figure 1.8: Photograph (left) and drawing (right) of a barrel module, showing its components. The thermal pyrolytic graphite (TPG) base-board provides a high thermal conductivity path between the coolant and the sensors.

The Straw Tubes of the TRT

The Transition Radiation Tracker (TRT) is located in the outer part of the inner detector and contains 73 layers of straw tubes interleaved with fibres

in the barrel and 160 straw planes interleaved with foils in the endcap which provide transition radiation for electron identification. The straw tubes are made of polyimide and have a diameter of 4 mm while the anode wire present in each tube is made of tungsten with a diameter of 31μm, plated with 0.5-0.7 μm gold and supported at the end of the straw by an end-plug. The anode wires are directly connected to the front-end electronics and kept at the ground potential. Each tube is filled with a gas mixture composed by $Xe/CO_2/O_2$ (70/27/3) in order to provide a gain of 2.5×10^4 with a 5-10 mbar overpressure for an operating voltage of -1530V for the cathodes. Low-energy transition radiation (TR) photons are absorbed in the gas mixture providing much larger signal amplitudes with respect to minimum-ionizing charged particles. The distinction between TR and tracking signals is performed using separate low and high thresholds in the front-end electronics. Charged tracks with $p_T > 0.5$ GeV and $|\eta| < 2.0$ traverse at least 36 straws (22 in the transition region $0.8 < |\eta| < 1.0$). Moreover, seven to ten high-threshold hits from transition radiation are expected for electrons with energies above 2 GeV. The intrinsic tube resolution is $\sim 130\mu$m in the $R\phi$ plane.

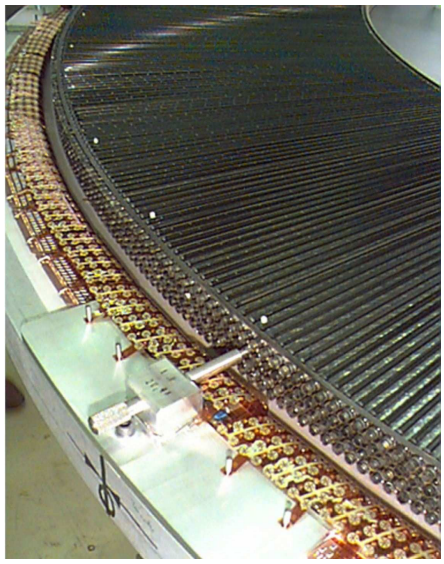

Figure 1.9: Photograph of a four-plane TRT endcap wheel during assembly.

1.2.3 The Calorimeters

The ATLAS calorimetric system is shown in figure 1.10. It is composed by an electromagnetic calorimeter [13] which covers the pseudorapidity range $|\eta| \leq 3.2$ and a hadronic calorimeter[14] that provides a pseudorapidity coverage up to $|\eta| \leq 4.9$.

- **The electromagnetic calorimeter**
  The calorimeter is composed by two identical half cylinders in the barrel region and by two coaxial wheels for each side in the endcap covering respectively the pseudorapidity range of $1.4 \leq |\eta| \leq 2.5$ the outer and $2.5 \leq |\eta| \leq 3.2$ the innermost.

  The electromagnetic calorimeter is a Liquid Argon detector with lead absorber plates and Kapton electrodes. For this detector, both in the barrel and in the endcap region, an "accordion" geometry has been chosen for the absorbers and the electrodes (figure 1.11). This kind of geometry naturally ensures a full coverage in *phi* without any cracks, and a fast

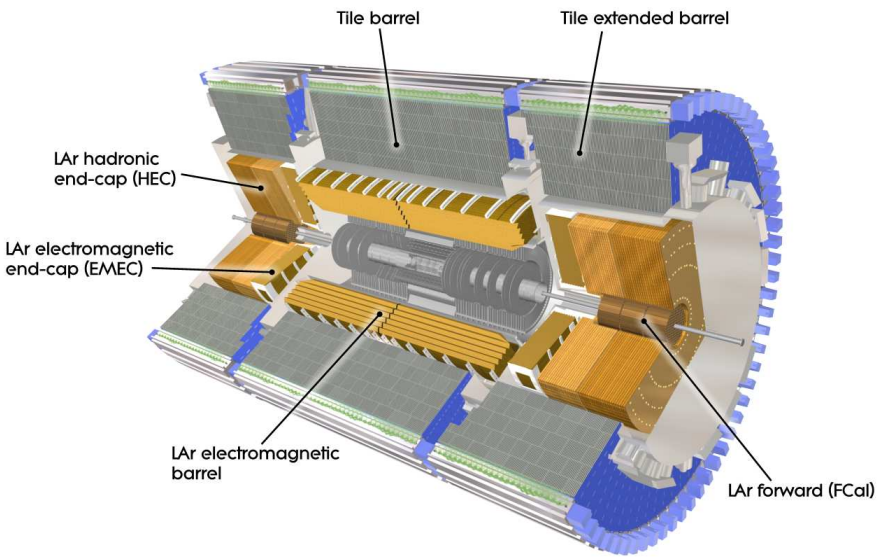

Figure 1.10: The ATLAS calorimetric system.

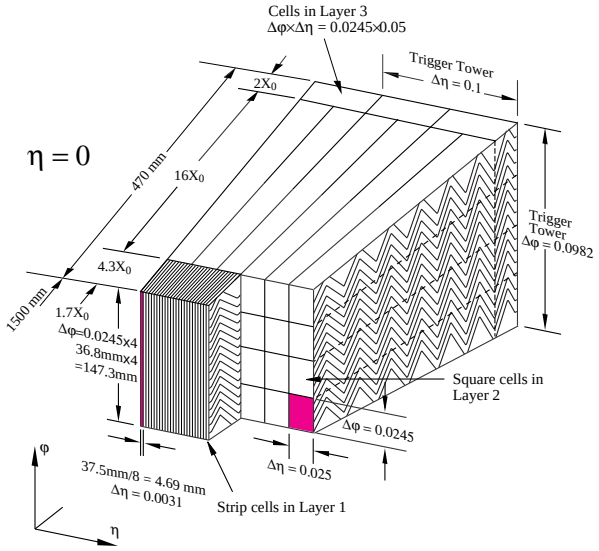

Figure 1.11: Sketch of a barrel module where the different layers are clearly visible with the ganging of electrodes in phi. The granularity in eta and phi of the cells of each of the three layers and of the trigger towers is also shown.

extraction of the signal at the rear or at the front of the electrodes. The position of the electrodes fixes automatically the calorimetric cells segmentation that corresponds to $\Delta\eta \times \Delta\phi = 0.025 \times 0.0245$ (4x4 cm^2 at $\eta = 0$). The thickness of the lead layers change as a function of η from 1.5 mm for $|\eta| \leq 0.8$ up to 2.2 mm for $0.8 \leq |\eta| \leq 3.2$; the radial thickness of the liquid argon volumes is 2.1 mm in the barrel and goes from 0.9 mm up to 3.1 mm in the endcaps. The total active thickness of a barrel module at least 22 radiation lengths (X_0), increasing from 22 X_0 to 30 X_0 for $0 \leq |\eta| \leq 0.8$ and from 24 X_0 to 33 X_0 between $0.8 \leq |\eta| \leq 1.3$ while, in the endcap, goes from 24 to 38 X_0. This structure allows to obtain both a good energy resolution and an almost full coverage along the azimuthal direction that is needed in order to have the maximum geometrical acceptance to reconstruct events with a very low cross section, like $H \rightarrow \gamma\gamma$. The energy resolution of an electromagnetic calorimeter is

given by the relationship

$$\frac{\sigma(E)}{E} = \sqrt{\left(\frac{a}{\sqrt{E}}\right)^2 + \left(\frac{b}{E}\right)^2 + c^2} \tag{1.2.2}$$

where a is the stochastic term, b takes into account the electronic noise and c is the constant term that reflects local non-uniformities in the response of the calorimeter. For the ATLAS electromagnetic calorimeter, $a = 10\%$, $b = 0.5\%$ and $c = 0.7\%$. In the energy range 15-180 GeV, the reconstructed energy response is linear within $\pm 0.1\%$.

- **The hadronic calorimeter**

  The ATLAS hadronic sampling calorimeter covers a pseudorapidity range of $|\eta| \leq 4.9$ using different technologies, depending on the η value. In the region $|\eta| \leq 1.7$ is installed a sampled calorimeter called *Tile Calorimeter* using steel layers with a thickness of 14 mm for the absorber and scintillator tiles for the active medium. The η-ϕ segmentation in this region is $\Delta\eta \times \Delta\phi = 0.1 \times 0.1$. In the endcaps ($1.5 \leq |\eta| \leq 3.2$) layers of copper are used as absorber due to higher radiation flux, alternated to volumes filled with liquid Argon. The thickness of these layers goes from 25 mm in the innermost part to 50 mm for the outer. Finally, in the forward regions ($3.1 \leq |\eta| \leq 4.9$), the technology chosen is liquid Argon volumes alternated to copper or tungsten layers. Material and total thickness of the hadronic calorimeter has been chosen in order to obtain a good hadronic calorimeter shower containment, to measure accurately the missing transverse energy E_T^{miss} and to reduce the *punch-through* in the muon spectrometer. As it is shown in figure 1.12, the amount of material at $\eta = 0$ corresponds to 11 interaction lengths (λ). The ATLAS hadronic calorimeter is characterized by two different energy resolution depending on the η region:

$$\frac{\sigma(E)}{E} = \frac{50\%}{\sqrt{E(GeV)}} \oplus 3\% \qquad |\eta| \leq 3 \tag{1.2.3}$$

$$\frac{\sigma(E)}{E} = \frac{100\%}{\sqrt{E(GeV)}} \oplus 10\% \qquad 3 \leq |\eta| \leq 5 \tag{1.2.4}$$

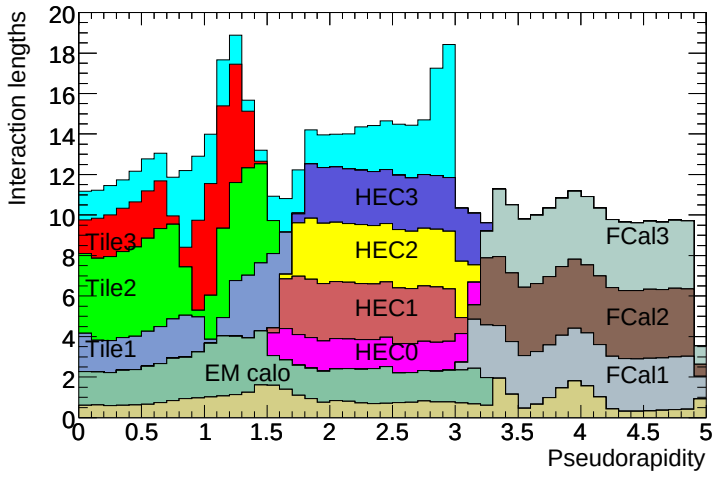

Figure 1.12: Cumulative amount of material, in units of interaction length, as a function of $|\eta|$, in front of the electromagnetic calorimeters, in the electromagnetic calorimeters themselves, in each hadronic compartment, and the total amount at the end of the active calorimetry. Also shown for completeness is the total amount of material in front of the first active layer of the muon spectrometer (up to $|\eta| < 3.0$).

1.2.4 The Muon Spectrometer

The muon spectrometer [15] is located in the outer part of the ATLAS detector and should allow a very precise tracking of the high p_T muons with a good transverse momentum resolution and provide a trigger for the experiment. The most important parameters that have been optimized in the design phase of this part of the ATLAS experiment are:

- **the resolution**: a good resolution for the p_T and mass measurement of the order of few percent is needed for a reliable muon charge identification (especially for very high p_T muons) and a good reconstruction of final state decays in two muons (i.e. $Z \to \mu^+\mu^-$) or four muons (i.e. $H \to ZZ^{(*)} \to 4\mu$). Moreover a uniform transverse momentum resolution is requested in the all the pseudorapidity range covered by the muon

spectrometer.

- **the second coordinate measurement**: in order to obtain a better track reconstruction, it is necessary to detect the muons also in the non bending direction. A resolution better than 1 cm is required.

- **the rapidity coverage**: a good rapidity coverage up to $|\eta| \sim 3$ is needed to study all the physics processes that have muons in the final states.

- **the bunch crossing identification**: the time interval between two bunch crossing at the nominal luminosity will be of 25 ns and this automatically sets a limit on the time resolution for the trigger.

The ATLAS muon spectrometer, that covers a surface of 5000 m^2, is designed to be able to detect particles that will pass the barrel and endcap calorimeters, to measure their momenta in the pseudorapidity range of $|\eta| < 2.7$, and trigger them in a pseudorapidity range of $|\eta| < 2.4$. In particular the performance goal is a standalone p_T resolution of $\sim$10% for 1 TeV tracks. Muons can be reconstructed in an independent way with respect to the inner detector from $\sim$3 GeV (that approximatively correspond to the energy loss in the calorimeters) up to 3 TeV. To reconstruct the muon transverse momentum, they are bent (along the η view) by the toroidal magnetic field generated by the air-core toroid magnets described in the section 1.2.1. In figure 1.13 a section of the ATLAS muon system in the x-y plane and z-y plane is shown.
In the barrel region, the muon subdetectors are mounted on three concentric cylinders with their axis that coincide with the beam axis at radii of about 5, 7.5 and 10 m. Groups of three chambers at different radius forms projective towers that point to the interaction position; with this geometry, muons coming from the interaction point will cross at least three precision chambers thus to measure the particle momentum from the measurement of the trajectory sagitta. In the endcap regions, the detector chambers are placed in four concentric disks located at 7, 10 14 and 21-23 m away from the interaction point.

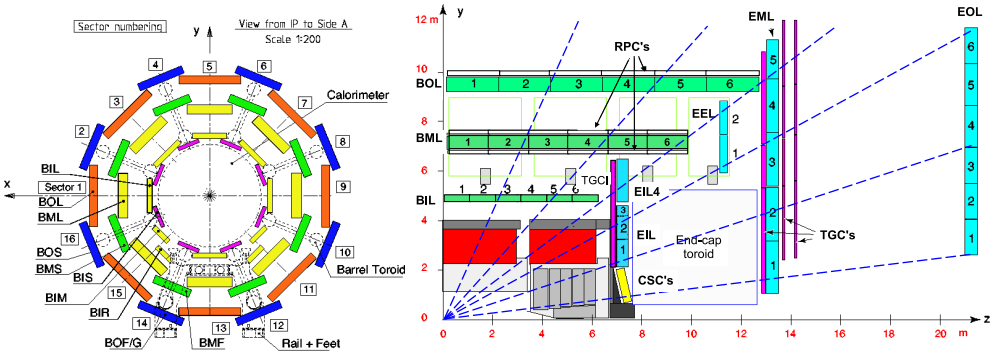

Figure 1.13: Transverse (left) and longitudinal (right) view of the ATLAS muon spectrometer.

Along the azimuthal direction the spectrometer is divided in 16 sectors and their dimension depends if they are between two coils of the toroidal magnet (Large Sectors) or if they contain only one of the coils (Small Sectors).
Taking into account all the requirements in terms of performance, rate capability, granularity, ageing properties and radiation hardness, Monitored Drift Chambers (MDTs) and Cathode Strip Chambers (CSC) have been chosen for the precision measurement of the muon track while the Resistive Plate Chambers (RPC) and the Thin Gap Chambers (TGC) are used in order to provide the muon trigger to the experiment. In table 1.3 the main parameters of the ATLAS muon chambers are reported.

- **Monitored Drift Chambers (MDT)** These precision chambers cover the rapidity region $|\eta| < 2.0$ of the muon spectrometer. The basic elements of these chambers are tubes with a diameter of 29.97 mm filled with Ar/CO_2 gas mixture (93/7) at the pressure of 3 bar. When a muon cross the tube, the electrons generated in the ionization of the gas are collected at the central tungsten-rhenium wire that has a diameter of 50 μm and is maintained at a potential of 3080 V in order to work in the avalanche regime. At this working point, the maximum drift time is around 700 ns. The gas mixture used for this detector has been chosen

Drift Tubes:	MDTs
- Coverage	$\|\eta\| < 2.0$
- Number of chambers	1170
- Number of channels	354 000
- Function	Precision measurement
Cathode Strip Chambers	
- Coverage	$2.0 < \|\eta\| < 2.7$
- Number of chambers	32
- Number of channels	31 000
- Function	Precision measurement
Resistive Plate Chambers	
- Coverage	$\|\eta\| < 1.05$
- Number of chambers	1112
- Number of channels	374 000
- Function	Triggering, second coordinate
Thin Gap Chambers	
- Coverage	$1.05 < \|\eta\| < 2.4$
- Number of chambers	1578
- Number of channels	322 000
- Function	Triggering, second coordinate

Table 1.3: Main parameters of the ATLAS muon chambers.

for the good ageing properties but has the disadvantage of a non linear space- drift time relationship; this leads to a reduction of the spatial resolution in a high counting rate that has been measured to be around 70-80 μm per tube.

The tubes are arranged in 2x4 monolayers for the inner stations and 2x3 for the outer stations to form a station that can be rectangular in the barrel and trapezoidal in the endcaps. A schematic view of the structure of an ATLAS MDT chamber is shown in figure 1.14. The two multilayers

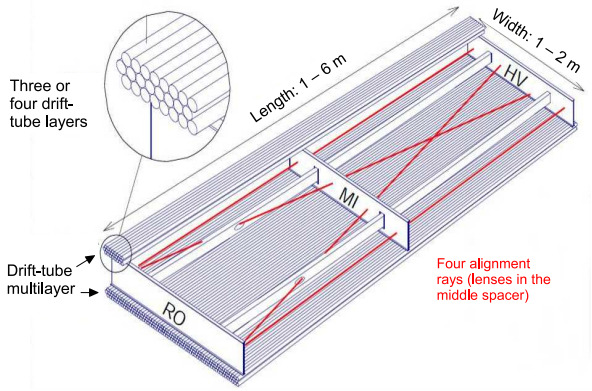

Figure 1.14: Mechanical structure of a MDT chamber. Four optical alignment rays, two parallel and two diagonal, allow for monitoring of the internal geometry of the chamber [16, 17]. RO and HV indicate the location of the readout electronics and high voltage supplies.

of each station are placed on either side of a special support structure (spacer), that ensure the accurate positioning of the tubes with respect to each other. In the case of non vertical chambers, the support structure also slightly bends the tubes of the chambers in order to compensate the gravitational sag of the wires which are not in a vertical position. Moreover deformation are expected to occur and may change with time (due to thermal gradients) and they will be monitored by an in-plane optical system that have its component mounted on the spacers.
In the operative scheme of this detector, a set of data for auto-calibration is needed to determine the r-t relation (drift-time drift-distance relation) for a tube, in order to correct small deviation from the radial drift due to magnetic effect and change of environmental parameters (temperature, humidity and so on).

- **Cathode Strip Chambers (CSC)** This detector, which combines high spatial, time and double track resolution with high-rate capability and low neutron sensitivity, substitute the MDT in the innermost layer of the endcap region in the pseudorapidity range of $2.0 < |\eta| < 2.7$ where rates

higher than the MDT rate capability (safe operation up to 150 Hz/cm^2) are reached. The whole CSC system consists of two disks with eight chambers each (eight small and eight large) as shown in figure 1.15 (left). The CSCs are multiwire proportional chambers with the wires oriented in the radial direction. The cathodes are segmented, one with the strips perpendicular and the other parallel to the wires. The cathode-anode spacing is equal to the anode wire pitch (2.54 mm). The position of the track is then obtained by interpolation between the charges induced on neighboring cathode strips. The read out pitch of 5.31 mm and 5.56 mm for the large and small chambers respectively in the bending direction allows to reach a 60 μm resolution for each CSC plane. In the non-bending direction the resolution is 5 mm. The operating voltage of this detector is 1900 V and it uses a gas mixture of Ar/CO_2 (80/20).

- **Resistive Plate Chambers (RPC)** The RPCs are gaseous detectors made of two resistive plates of phenoli-melaminic plastic laminate with a volume resistivity of 10^{10} Ωcm that are kept at an interdistance of 2 mm by insulating spacers and with the outside surface coated with a thin layer of graphite paint (100 k$\Omega/\Box$) to assure the HV and the ground connection of the resistive electrodes. The volume is filled with a

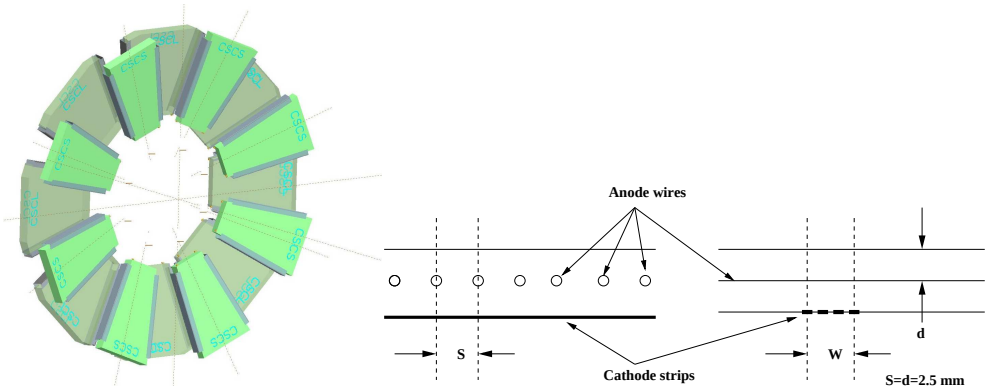

Figure 1.15: (left) Layout of a CSC end-cap with eight small and eight large chambers. (right) Schematic structure of the CSC cells.

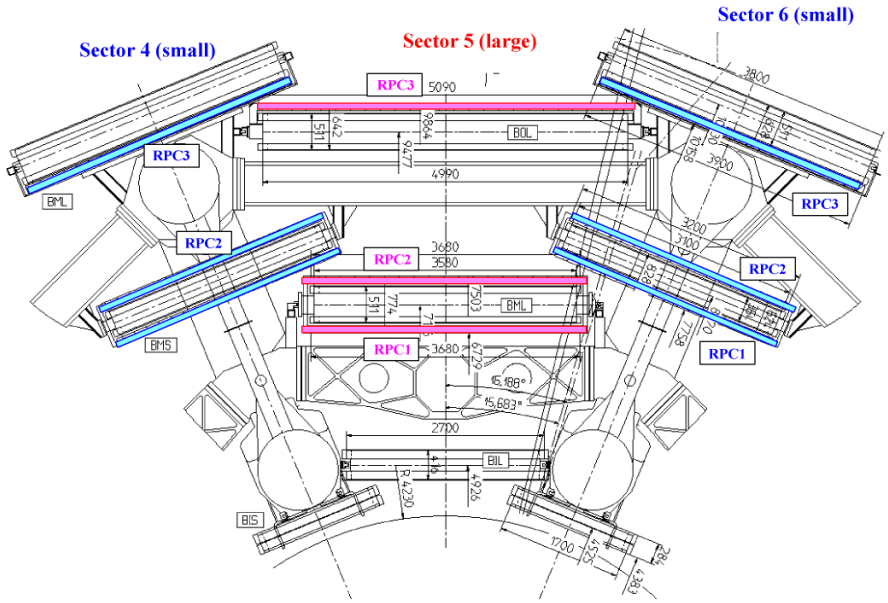

Figure 1.16: Cross-section through the upper part of the barrel with the RPCs marked in colour. In the middle chamber layer, RPC1 and RPC2 are below and above their respective MDT partner. In the outer layer, the RPC3 is above the MDT in the large and below the MDT in the small sectors.

gas mixture of $C_2H_2F_4$/Iso-C_4H_{10}/SF_6 (94.7/5/0.3) non flammable that permits to work in avalanche mode that offers the benefit of a high rate capability (the local rate capability is of the order of $\sim$ 1 kHz/cm^2). In order to have a formation of avalanche along the ionising track, an electric field of 4.9 kV/mm is applied. The signal produced is read out thanks to the capacitive coupling to copper strips that are mounted on the outer faces of the resistive plates. The RPCs are used in the barrel region $|\eta| < 1.05$ to provide the muon trigger and to measure the second coordinate in the non bending direction. They are arranged in three concentric cylindrical layers around the beam axis as it is shown in figure 1.16. The inter-distance between the middle and outer layers permits the trigger to select tracks with 9 $<p_T <$ 35 GeV while the two middle

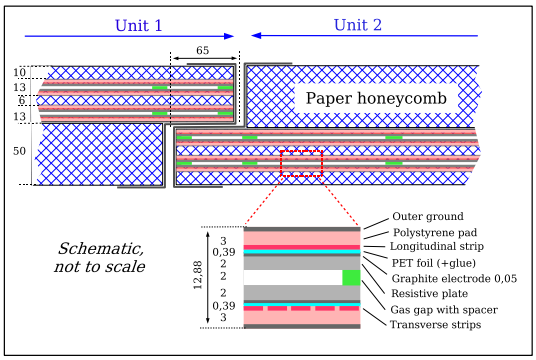

Figure 1.17: Cross-section of a RPC, where two units are joined to form a chamber. The phi-strips are in the plane of the figure and the eta-strips are perpendicular to it

chambers provide the low-p_T trigger ($6 < p_T < 9$ GeV). An RPC chamber is composed by two rectangular detector units that are contiguous to each other. Each unit is then composed by two independent detector layers (gas volumes) that have a structure that is shown in figure 1.17 and is identical for all the RPCs.

- **Thin Gap Chambers (TGC)** The TGCs are mounted in two concentric rings located in the endcap regions and covers the rapidity range between $1.05 < |\eta| < 2.0$. Like the RPCs in the barrel region, this detector will provide the muon trigger capability in the endcap regions and the determination of the second, azimuthal coordinate to complement the measurement of the MDT in the bending (radial) direction. The TGC have a structure very similar to the one of the multiwire proportional chamber, with the difference that the anode wire pitch (1.8 mm) is larger than the anode-cathode distance (1.4 mm) as shown in figure 1.18. The cathodic strips are separated from the gas volumes with graphite layers and have a pitch that goes from 14.6 and 49.1 mm with an orientation that is orthogonal to the anodic wires. The gas mixture used is CO_2 at 55% and $n-C_5H_{12}$ (n-pentane)at 45% thus to work in a quasi-saturated mode (gain $\sim$ 3x10^5) with the advantage to have a lower

sensibility to the mechanic deformations. The working point of the TGC is 2.9 kV

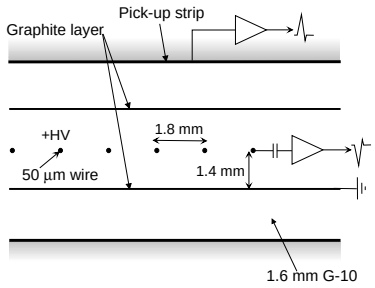

Figure 1.18: Schematic structure of a TGC

1.2.5 The Trigger System

At the design luminosity the proton-proton interaction rate will be of the order of 1 GHz, considering an interaction rate of 40 MHz and 23 interactions per bunch crossing. Due to the fact that most of the events are not interesting for physics analysis and to the limited storage capacity and computing power, a trigger system has been designed for the ATLAS experiment to trim this rate down to a more manageable data flow. It is organized in three level: each trigger level refines the decision made by the previous level and it is based on fast and crude reconstruction of physics object like muons, electrons, photons, jets.

- **L1 - Level 1 Trigger** The first level of the ATLAS trigger [18] chain is an hardware-based trigger and makes a first selection using the RPC and TGC chambers to identify muons with a high transverse momenta, the calorimeters for high E_T photons and electrons, jets, τ decaying in hadrons. Moreover, the calorimetric information (with reduced granularity) is used to measure the total and missing transverse energy. Cuts on the energy and p_T are applied and events that pass the L1 trigger selection are transferred to the next trigger level. The output rate of the

L1 trigger cannot exceed the 75 kHz with a maximum latency of 2.5 μs required to make the final decision. During this time, the information coming from all the detector is temporary saved in local memories with a limited extension (pipelines) that are mostly located in integrated circuits near the detectors. In addition the L1 trigger defines one or more Regions-of-Interest (RoIs) corresponding to $\eta - \phi$ region of the detector where the object that pass a certain trigger item is present, that will be given to the second level of the trigger.

- **L2 - Level 2 Trigger** The level two trigger [19] is a software-based trigger that is seeded by the RoI information provided by the L1 trigger. The information with full granularity and precision is used to reconstruct within a RoI and only the events that satisfy a certain set of selection on the measured quantities of physics object pass this trigger level. The trigger rate is reduced to approximately 3.5 kHz, with an event processing time of about 40 ms.

- **EF - Event Filter** The final stage of the trigger selection is carried on by the Event Filter, which roughly reduces the event rate to 200 Hz. Here only events that pass at least one of the L2 trigger algorithm are processed. This level have access to the whole event, using the full granularity and all the ATLAS detector information. The EF use the offline analysis procedure, such as detailed reconstruction algorithms and the mean processing time for one event at the event filter is $\sim$4 seconds. This last step of the ATLAS trigger runs on a dedicated computer farm that is located near the ATLAS cavern and the events that pass this final stage are written to the mass storage and available for the further offline analysis.

1.2.6 The Minimum Bias Trigger

The Minimum Bias Trigger Scintillator (MBTS) is one of the triggers that have being used in the very early phase of the data taking in order to select Minimum

Bias events generated in the proton proton collisions. The MBTS detector is formed by 2 disks placed one on each side of the ATLAS detector; each disk is composed by 16 scintillator counters with a tick of 2 cm and they are placed at $z = \pm 3650$ mm with the face perpendicular to the beam axis covering a pseudorapidity range of $1.9 < |\eta| < 3.8$ that corresponds to an overall acceptance of $\sim$80% for inelastic interactions. The single disk is separated into an inner and an outer ring organized into 8 independent ϕ sectors. The light produced by the scintillator counters is collected using optical fibers and guided to a photomultiplier tube (PMT) and the signals from the PMTs are readout by the Tile Calorimeter electronics. In figure 1.19 a schematic view of an MBTS ring is shown. The MBTS multiplicity is calculated for each

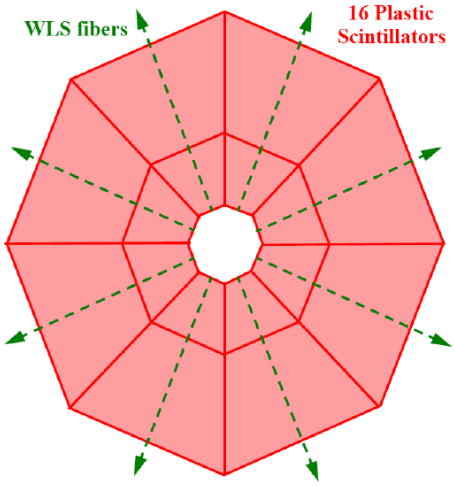

Figure 1.19: MBTS disc configuration

side independently. Using this information three L1 trigger items are formed: L1_MBTS_1, L1_MBTS_2 and the L1_MBTS_1_1. They require an ATLAS BPTX [1][21] signal, from either side, and the first also at least one MBTS hit,

[1]detector similar to the electrostatic beam pick-up system used by the LHC to monitor the transverse beam position in the beam pipe. They are located along the LHC, in both side of ATLAS at 175 m from the interaction point. Their trigger signals can be used and combined with other triggers in oder to ensure that a beam has passed through ATLAS.

the second also at least two MBTS hit and at third also at least one MBTS hit per side respectively.

Chapter 2

Minimum Bias Physics at LHC at $\sqrt{s} = 900$ GeV and $\sqrt{s} = 7$ TeV

2.1 QCD and soft proton-proton collisions

The gauge field theory that describes the interaction between colored quark and gluons is called Quantum Chromodynamics (QCD). In the high energy regime where the effective coupling is small it is possible to apply perturbative techniques in order to make predictions from this theory. At high energies the parton model, where protons are composed by point-like constituents called partons, is proved to be a good approximation (i.e. Bjorken scaling observation) describing parton-parton interactions at large momentum transfer but it is not appropriate to model all the aspects of particle production. According to this model, partons carry a fraction x of the hadron momenta with a probability defined by the Parton Distribution Function (PDF)

$$f(x)dx \equiv \mathcal{P}(x' \in [x, x+dx]) \qquad f = q, \bar{q}, g \tag{2.1.1}$$

In a hadron-hadron scattering (figure 2.1), the cross section can be factorized [22]in the following way

$$\sigma(h_1 h_2 \to cd)(Q^2) = \sum_{q,\bar{q},g} \int_0^1 dx_1 dx_2 f_{a/h1}(x_1, \mu_F^2) f_{b/h2}(x_2, \mu_F^2) \hat{\sigma}^{(ab\to cd)}(Q^2, \mu_F^2) \tag{2.1.2}$$

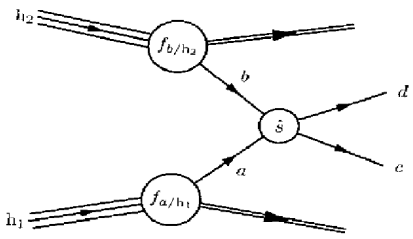

Figure 2.1: Schematic view of a hadron hadron scattering.

with a convolution between the PDFs and the partonic cross section $\hat{\sigma}$. The PDFs include all the phenomena that cannot be calculated with the perturbative techniques that dominate the low energy region (infrared region) while the partonic cross section includes only terms of the ultraviolet region and can be calculated applying the Feynman rules for the QCD. The factorization scale μ_F represent the limit between the infrared and the ultraviolet regions. Experimentally the cross section $\sigma(h_1 h_2 \rightarrow cd)(Q^2)$ can be measured and, when the renormalization scheme is fixed, it is possible to calculate the partonic cross section at each order. Moreover, for a fixed perturbative order and renormalization scheme used, the Parton Distribution Functions are universal in the sense that any other cross section for a process calculated using the same renormalization scheme and at the same perturbative order will depend from the same PDF. The parton distributions used in these hard-scattering calculations are solutions of the DGLAP equations [23]

$$\frac{\partial q_i(x,\mu^2)}{\partial \log \mu^2} = \frac{\alpha_S}{2\pi}\int_x^1 \frac{dz}{z}\Big\{P_{q_i q_j}(z,\alpha_S) q_j(\frac{x}{z},\mu^2) + P_{q_i g}(z,\alpha_S)\; g(\frac{x}{z},\mu^2)\Big\}$$
$$\frac{\partial g(x,\mu^2)}{\partial \log \mu^2} = \frac{\alpha_S}{2\pi}\int_x^1 \frac{dz}{z}\Big\{P_{g q_j}(z,\alpha_S) q_j(\frac{x}{z},\mu^2) + P_{gg}(z,\alpha_S) g(\frac{x}{z},\mu^2)\Big\} \quad (2.1.3)$$

where the splitting functions have perturbative expansions:

$$P_{ab}(x,\alpha_S) = P_{ab}^{(0)}(x) + \frac{\alpha_S}{2\pi} P_{ab}^{(1)}(x) + ... \quad (2.1.4)$$

The DGLAP equations determine the Q^2 dependence of the PDFs while the x dependence has to be obtained from fitting deep inelastic and other hard-scattering data. Figure 2.2 shows the predictions for some important Standard

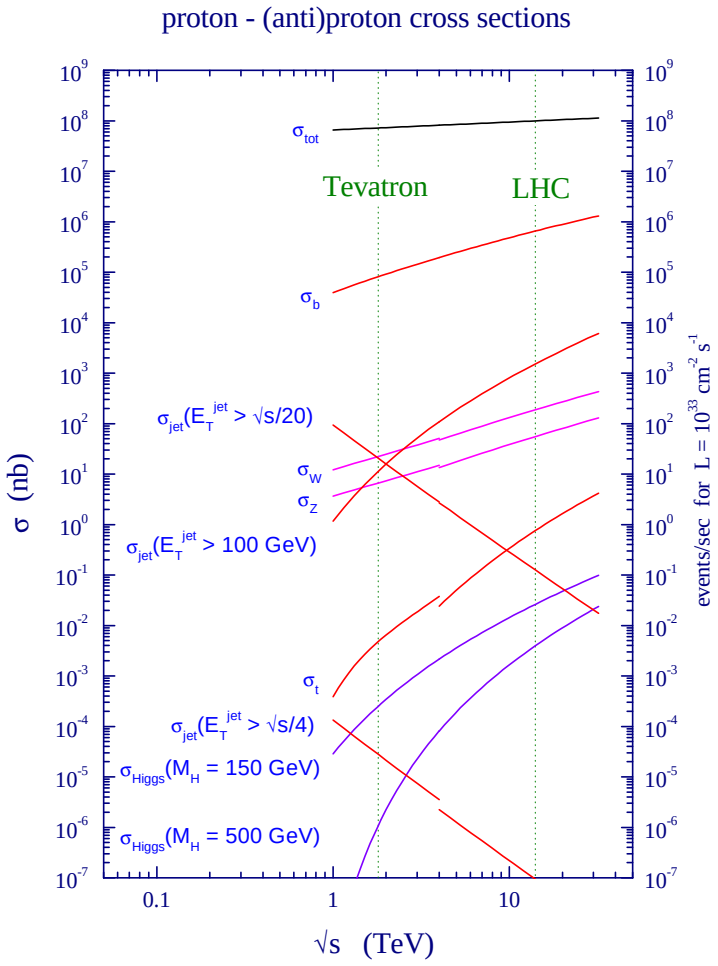

Figure 2.2: Standard Model cross sections at the Tevatron and LHC colliders.

Model cross sections at $\bar{p}p$ and pp colliders, calculated at the next-to-leading order in perturbation theory.

Measuring the characteristics of inelastic proton-proton collisions during early running at the LHC (minimum bias events) is useful for the understanding of the physics behind these processes and allows the characterization of the properties of the soft-part of the underlying event in high-p_T collisions. More-

over, they can provide the baseline for measurements in heavy-ion collisions.

The total proton-proton interaction cross section can be expressed as the sum of an elastic component and an inelastic component. Moreover, the inelastic component can be expressed in terms of diffractive (single diffractive, double diffractive) and non diffractive components as indicated in 2.1.5

$$\sigma_{tot} = \sigma_{elastic} + \sigma_{inelastic} = \sigma_{elastic} + \sigma_{SD} + \sigma_{DD} + \sigma_{ND} \tag{2.1.5}$$

A schematic view of the three inelastic components is shown in figure 2.3. The non-diffractive interactions are the inelastic processes with the largest cross section and they occur when there is a color exchange between the two protons of the colliding beams. In single or double diffractive events a single pomeron [1] is exchanged between the two interacting protons and one of the two (or both in the case of double diffraction) forms a diffractive system. Multiplicities and topologies of these three components are also different. Non-diffractive events, where a color charge exchange happens, are characterized by the production of a large number of particles mainly produced in central rapidity with the multiplicity that goes down at forward rapidities. In case of a single diffractive interaction, only one of the protons breaks with the production of particles in the high rapidity region while the other incoming proton is essentially undisturbed preserving the same rapidity of the beam. For double diffractive events, both colliding protons break producing particles symmetrically in the high rapidity regions with a few particles produced in

[1] The pomeron is an effective particle with vacuum quantum numbers. In Regge theory [24, 25] it is identified as a trajectory with the intercept $\alpha_{(0)} = 1 + \epsilon$ with $\epsilon = 0.08$ [26].

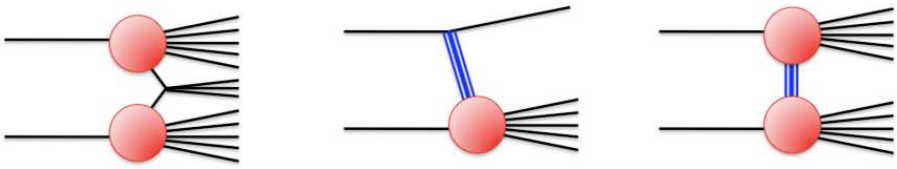

Figure 2.3: Schematic view of different inelastic scattering: non diffractive (left), single diffractive (center) and double diffractive (right).

the central region. In both non diffractive and double diffractive events the particles are produced symmetrically with respect to $\eta = 0$.

2.1.1 Monte Carlo generators

In order to simulate the particle production in proton-proton collisions different Monte Carlo generators can be used. They use both the perturbation theory of QCD to predict the behavior of the hard scattering interaction (characterized by large momentum transfer) and phenomenological models to describe the soft proton-proton interaction that characterize mostly of the pileup component in a hard scattering event and the so called underlying event. This phenomenological models have different parameters that can be tuned using the results of previous experiments in order to make prediction in a new energy regime. Thus different tuning can be considered in the comparison between data and Monte Carlo simulations. A short description of PYTHIA and PHOJET Monte Carlo generator follows.

PYTHIA

The PYTHIA [27] Monte Carlo generator describes the soft interaction between protons with a 2→2 QCD matrix element at the leading order adding also the multiple parton interaction and the initial and final state radiations. The separation between perturbative QCD and the phenomenological regime is regulated tuning a variable, ${p_T}^{min}$, corresponding to the momentum transfer in the hard interaction. This Monte Carlo generator also includes effects like color reconnection or the interactions with the beam remnants; the former, for example, makes possible the interaction between partons according to their color charge. The description of the parton shower in PYTHIA is made differently depending when a parton can start to shower: commonly partons can be ordered by virtuality or p_T. In case of p_T ordered showers, the hardest interactions come first. Most of the tunes use the most recently implemented model of multiple parton interactions [28, 29]. This kind of models permit multiple parton interactions to be interleaved with the parton showers, so that

interplay between the multiple parton interactions and the parton showers is described properly.

PHOJET

In PHOJET [30] the simulation of the transition between the hard and the soft scales is made using the Dual Parton Model (DPM) [31] where soft interactions are described by non topological expansion of the Quantum Chromodynamics. The hard interactions are calculated using the pQCD while both hadronization and parton fragmentation are described using the PYTHIA routines. Inelastic events are described using cut pomerons corresponding to the exchange of a soft gluon, which results in color string being drawn between the beam remnants. The uncut pomerons provide virtual corrections preserving unitarity. As the pomerons can be both hard and soft, PHOJET provides a smooth transition between the soft and hard scales.

2.1.2 Minimum Bias processes cross-section

Table 2.1 shows the predicted cross-sections by PYTHIA 6.4 and PHOJET for the different minimum bias processes (non-diffractive, single diffractive and double diffractive) at the three center of mass collision energies provided by the LHC (0.9, 2.36 and 7 TeV). The total cross section by PHOJET is 5-10% higher with respect to the one predicted by PYTHIA. The largest contribution for the total inelastic cross section at all the energies comes from the non diffractive components. Single diffractive and double diffractive events follow. PHOJET can simulate and predict also the central diffractive component [2] that in any case have a cross section that is three times smaller than the double diffractive one.

[2] Two pomerons are exchanged in Central Diffractive events.

Process Type	900 GeV [mb]	2.36 TeV [mb]	7 TeV [mb]
PYTHIA			
Non-diffractive	34.4	40.2	48.5
Single diffractive	11.7	12.7	13.7
Double diffractive	6.4	7.7	9.3
Total inelastic	52.5	60.6	71.5
PHOJET			
Non-diffractive	39.9	50.3	61.5
Single-diffractive	10.5	10.6	10.7
Double-diffractive	3.5	3.9	3.9
Central-diffractive	1.1	1.2	1.3
Total inelastic	55.0	66.0	77.4

Table 2.1: Cross-sections for the inelastic components of the minimum bias sample at $\sqrt{s}$ = 900 GeV, 2.36 TeV and 7 TeV as predicted by PYTHIA 6 and PHOJET.

2.1.3 Monte Carlo Generators tuning

Most of the generators use phenomenological models to describe soft hadronic interactions that have a lot of free parameters that need to be tuned using experimental measurements. One of the major problems is to extrapolate the parameters at different center of mass energies. The tuning of the PYTHIA parameters is needed to describe the following different phenomena:

- the hadronization and the final state radiation;
- the initial state radiation and primordial k_T;
- the underlying events, the beam remnants, the color reconnection;
- the energy scaling.

These parameters also depend on the parton distribution functions used by the Monte Carlo generator. The strategy used to tune the different parameters consists in making comparisons between the predicted and the measured distributions. The difference that can appear between tunings comes, for example, from the different sets of experimental results used to generate a particular tuning or the different procedure used to evaluate an optimal value. Different tools can be used to perform the tuning and the comparisons between data and MC like Rivet [32] that provides a library of experimental analyses and tools to calculate physical observables from an event record of a Monte Carlo generator, or the Professor [33] tool that parametrizes the generator response in each observable bin. These tools were used, for example, to produce the ATLAS MC09c tunes. The Perugia tunes [34] were produced tuning PYTHIA 6.4 with p_T-ordered shower using the minimum bias measurements from UA5 [35] and CDF. For this tuning, no underlying event measurement has been used.

The DW tune [36] was generated by tuning PYTHIA to CDF Drell-Yan data and measurements of the underlying event, without using minimum bias data. This tune uses the virtuality ordered parton showering from PYTHIA. The DW tune was based on a previous tune, Tune A, obtained from fits to the CDF Run I minimum bias and underlying event measurements, including also the Z boson p_T and the dijet $\Delta\phi$ measurement from D0 that corresponds to a total of 15 different tuned parameters.

A certain number of tunes based on PYTHIA are also produced by the ATLAS Collaboration using both minimum bias and underlying CDF measurements and the D0 measurement on the di-jet angular correlations with a total of 16 parameters tuned. In the MC09 [59] tuning, produced before the LHC data taking, the cut-off parameter of the multiple parton interaction model and its dependence on the center of mass energies had a large impact on the multiplicity distributions. The MC09c was produced to include the CDF measurements relative to the dependence of the p_T on n_{ch} that is sensitive to the color reconnection released after the MC09 tune was produced (essentially it brought

only to a different prediction for the p_T versus n_{ch} distribution).

Moreover, using the ATLAS measurements of charged particle multiplicity distributions at 900 GeV and 7 TeV in a reduced phase-space (with the diffraction contribution suppressed), the new tune ATLAS Minimum Tune 1 (AMBT1) has been produced [37].

2.2 Minimum Bias Results in ATLAS at $\sqrt{s} = 900$ GeV and $\sqrt{s} = 7$ TeV

The first minimum bias event measurements performed with the ATLAS experiment have exploited the full capability of the ATLAS inner detector in the reconstruction of charged particles [38, 39, 40, 41]. As previously stated, the importance of these measurements is related to the possibility of a better understanding of the soft component of the proton-proton collisions in order to tune the Monte Carlo generators and to have a coherent description of the underlying event in the hard scattering processes.

The data used for this analysis was recorded at the three different proton-proton collision energies provided by the LHC since the end of 2009: 900 GeV, 2.36 TeV and 7 TeV. The same analysis was repeated for these three energies with some small differences [3]. Moreover, different phase-spaces have been studied: these are defined by the cut on the number of charged particles and the p_T of the tracks. They are summarized as follows:

- Events with at least 1 primary charged particle ($n_{ch} \geq 1$) with $p_T > 0.5$ GeV and $|\eta| < 2.5$.

- Events with at least 6 primary charged particles ($n_{ch} \geq 6$) with $p_T > 0.5$ GeV and $|\eta| < 2.5$.

[3] For example, in the 2.36 TeV runs, the collisions happen in a situation of no stable beams. In this case the SCT was in stand-by mode with a reduced sensors bias voltage with the consequence of a lower detection efficiency

- Events with at least 2 primary charged particles ($n_{ch} \geq 2$) with $p_T > 0.1$ GeV and $|\eta| < 2.5$.

The diffractive component is larger going down to 0.1 GeV than for tracks above 0.5 GeV. In particular it is estimated with PYTHIA 6 and 8 Monte Carlo to be approximately 21-22% for the first phase-space while is of the order of 14% for the third phase-space. The second phase-space have a negligible diffractive contribution and in particular the results obtained with these cuts have been used to improve the knowledge of the non-diffractive component summarized in a new PYTHIA tune, the AMBT1 (ATLAS Minimum Bias Tune 1).

2.2.1 Event Selection

The events are selected requiring:

- at least one hit in the Minimum Bias Trigger Scintillators (MBTS);
- a reconstructed primary vertex with at least two tracks;
- no further primary vertex composed of 4 or more tracks (to veto pile-up events);
- at least 1, 2 or 6 good tracks depending on the phase-space used.

The good track definition is given by:

- $|\eta| < 2.5$ and $p_T > 100$ MeV or $p_T > 500$ depending on the phase-space considered;
- Pixel and SCT hits requirements;
- transverse and longitudinal impact parameters calculated with respect to the event primary vertex $|d_0| < 1.5$ mm and $|z_0| \cdot \sin\theta < 1.5$ mm, respectively.

The distribution at the particle level within the chosen kinematic range, starting from the one reconstructed, can be obtained with the knowledge of the trigger, vertex and tracking efficiencies.

2.2.2 Efficiencies and corrections

The ATLAS minimum bias trigger efficiency ε_{trig}^{BS} was measured using a random trigger in coincidence with colliding bunches while the primary vertex reconstruction efficiency ε_{vtx}^{BS} was determined from the ratio of events with a reconstructed primary vertex compared to all triggered events. Both of them are calculated directly on data and are studied versus the number of selected tracks. Since the trigger and vertex efficiency were determined without the vertex requirement, only cut on the impact parameter of tracks with respect to the beam-spot was possible. Trigger and vertex efficiency calculated from data at $\sqrt{s} = 7$ TeV corresponding to the most inclusive phase-space are shown in figure 2.4. Track reconstruction efficiency was estimated using the generated MC sample of non-diffractive events. The uncertainty on the tracking efficiency was calculated checking the agreement between data and simulation for various track reconstruction parameters. The largest uncertainty on the tracking efficiency comes from the material description of the tracking detec-

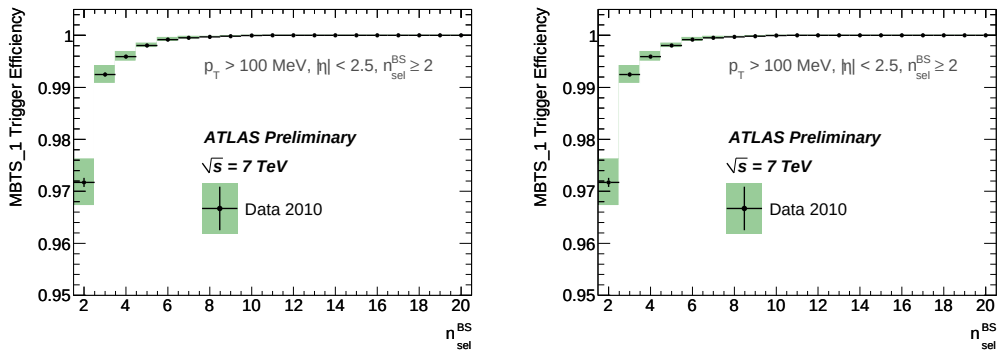

Figure 2.4: (left) The efficiency of the single MBTS trigger as a function of the number of pre-selected tracks for data at $\sqrt{s} = 7$ TeV. (right) The vertex reconstruction efficiency as a function of the number of pre-selected tracks for data at $\sqrt{s} = 7$ TeV. In both cases, the vertical bars represent the statistical uncertainty, while the green shaded areas represent the statistical and systematic uncertainties added in quadrature.

tor. In fact, the comparison between data and simulation gives a conservative uncertainty of 10% on the material description, and this results to a 3% of uncertainty in the tracking reconstruction efficiency. Figure 2.5 shows the tracking efficiency versus the pseudorapidity (left) and versus the transverse momentum. As expected, the efficiency is lower for lower momentum tracks and for high rapidity regions. In order to obtain the particle-level distributions in one of the described phase-space, corrections for detector effects are applied. The events lost due to trigger and vertex requirements are recovered using an event-by-event weight

$$w_{ev}(n_{sel}^{BS}) = \frac{1}{\varepsilon_{trig}(n_{sel}^{BS})} \cdot \frac{1}{\varepsilon_{vtx}(n_{sel}^{BS})} \tag{2.2.1}$$

Track distributions are further corrected with a track-by-track weight as function of p_T and η

$$w_{trk}(p_T, \eta) = \frac{1}{\varepsilon_{trk}(p_T, \eta)} \cdot (1 - f_{sec}(p_T, \eta)) \cdot (1 - f_{okr}(p_T, \eta)) \tag{2.2.2}$$

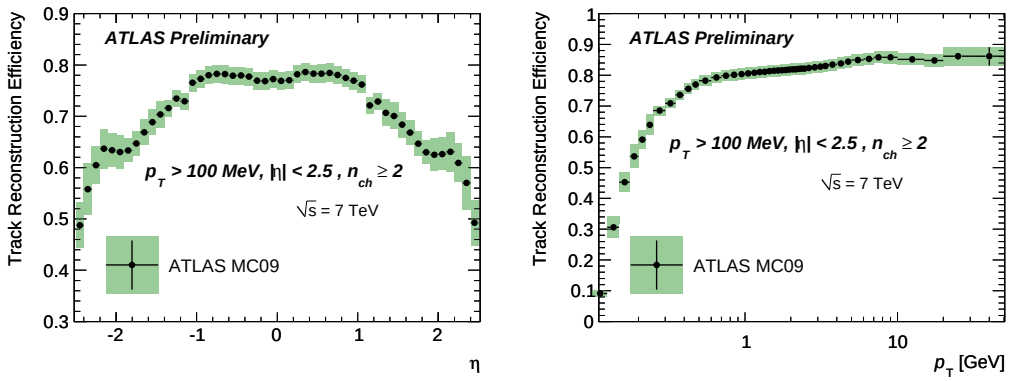

Figure 2.5: (left) Track reconstruction efficiency versus the pseudorapidity (left) and the transverse momentum (right) at $\sqrt{s} = 7$ TeV. (right) The vertex reconstruction efficiency as a function of the number of pre-selected tracks for data at $\sqrt{s} = 7$ TeV. In both cases, the vertical bars represent the statistical uncertainty, while the green shaded areas represent the statistical and systematic uncertainties added in quadrature.

where f_{sec} is the fraction of secondary tracks (eg. charged particles coming from the decay of long lived neutral particles) that pass the selection cuts applied and f_{okr} is the fraction of reconstructed selected tracks for which the corresponding primary particle is outside the kinematic range. Finally an unfolding matrix, filled using simulated data (PYTHIA 6 with ATLAS MC09 tune), with dimensions n_{ch} (number of the generated particles) times n_{sel} (number of selected tracks) is used to express the probability that a specific value of selected tracks was due to a certain number of charged particles. This matrix was applied to data to obtain the final n_{ch} distribution.

2.2.3 Charged particle distributions of minimum bias events

In the following paragraphs are reported final results of the charged particle multiplicity distributions for the most inclusive phase-space ($n_{ch} \geq 2$ with $p_T > 0.1$ GeV) at $\sqrt{s} = 900$ GeV and $\sqrt{s} = 7$ TeV. Data is compared with the predictions coming from a set of Monte Carlo models; these includes, in addition to the one produced before the LHC results, also the ATLAS Mimimum Bias Tune 1 (AMBT1). Moreover, since the data are presented as inclusive distributions, no correction to remove the single diffractive component was made (no model dependent correction) with the possibility to make easier the comparison to the different MC predictions and to provide a better constraint on diffraction models. The charged particle multiplicity at central pseudorapidity versus the center of mass energy of the collisions is also presented for both the phase spaces $n_{ch} \geq 1$ with $p_T > 0.5$ GeV and $n_{ch} \geq 2$ with $p_T > 0.1$ GeV for the different center of mass energies provided by the LHC in 2009 and 2010.

Charged particles distributions at $\sqrt{s} = 900$ GeV

The distributions of primary charged particles for events with $n_{ch} \geq 2$ in the kinematic range $p_T > 100$ MeV and $|\eta| < 2.5$ are shown in figure 2.6 for data

at $\sqrt{s} = 900$ GeV.

Figure 2.6a shows the charged particle multiplicity as a function of the pseudorapidity. This is approximately flat with a smooth dip in the central pseudorapidity region and decreasing at forward pseudorapidity (starting from $|\eta|$ <1.5). The charged-particle multiplicity at $\sqrt{s} = 900$ GeV per event and unit of pseudorapidity at $|\eta| = 0$ is $3.486 \pm 0.008(stat.) \pm 0.077(syst.)$. All the Monte Carlo tunes predict a charged particle multiplicity 15 - 20% lower than the measured multiplicity, except PHOJET that provides a good description of this distribution. The other tunes predict in any case correctly the shape of the pseudorapidity distribution apart DW that predicts a more pronounced dip in the multiplicity at central pseudorapidity.

Figure 2.6b shows the charged particle multiplicity as a function of p_T at $\sqrt{s} = 900$ GeV. Discrepancies between the measured and predicted multiplicity are observed both at low and high p_T regions. The best agreement with data is obtained by AMBT1 and PHOJET, which describe the p_T spectrum to within 20%. The ATLAS MC09 tune predicts too many particles at high p_T, while DW and PYTHIA8 predict too few.

The charged particle multiplicity distribution is shown in figure 2.6c. The PYTHIA-based models predict more events with n_{ch} =1 than in data (except PYTHIA8 that predicts less events with n_{ch} =1 but with an excess at around n_{ch} ∼10), but fewer events for n_{ch} >20, resulting in an average number of charged particle lower than in data. PHOJET and AMBT1 describe better the n_{ch} spectrum.

Figure 2.6d shows the average p_T as a function of n_{ch}. The average transverse momentum increases with the number of charged particles with the slope of the distribution that changes around $n_{ch} = 10$. The PYTHIA8 and AMBT1 models describe the data well within 5%, while the other models have discrepancies at the 10-20% level. The other PYTHIA-based models predict too large average transverse momentum in high multiplicity events, while PHOJET predicts small a smaller average p_T. The lower part of this spectra is particularly sensible to the diffractive components; moreover the average p_T as a function of

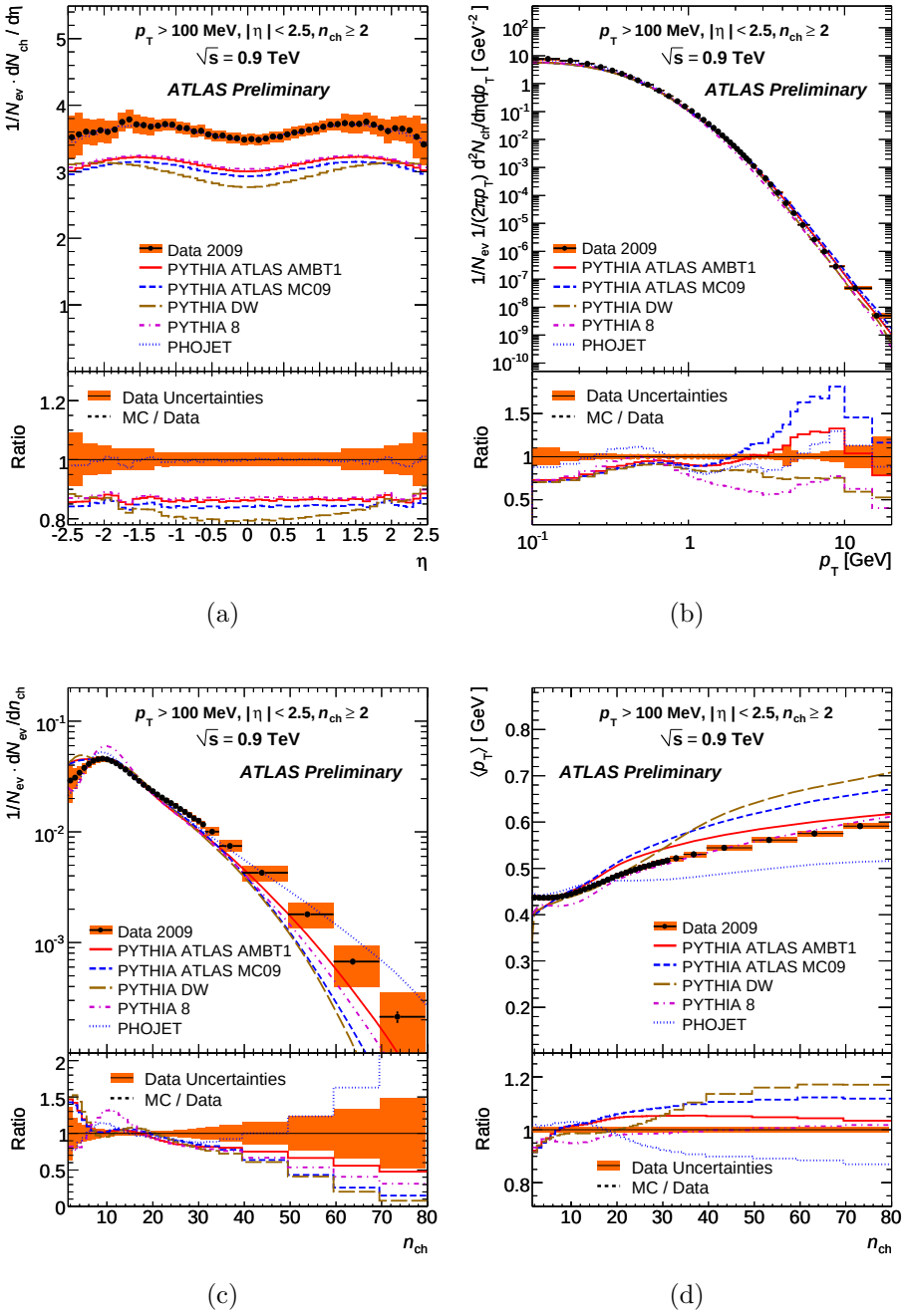

Figure 2.6: Charged particle multiplicities for events with $n_{ch} \geq 2$ within the kinematic range $p_T > 100$ MeV and $|\eta| < 2.5$ at $\sqrt{s} = 900$ GeV. The panels show the charged particle multiplicity as a function of the pseudorapidity (a) the charged particle multiplicity as a function of the transverse momentum (b), the charged particle multiplicity (c), and the average transverse momentum as a function of the number of charged particles in the event (d). The markers represent the data and the curves predictions from different Monte Carlo models. The vertical bars represent the statistical uncertainties, while the red shaded bands show the statistical and systematic uncertainties added in quadrature.

n_{ch} is particularly sensitive to the values of the color reconnection parameters in the models.

Charged particles distributions at $\sqrt{s} = 7$ TeV

The distributions of primary charged particles for events with $n_{ch} \geq 2$ in the kinematic range $p_T > 100$ MeV and $|\eta| < 2.5$ are shown in figure 2.7 for data at $\sqrt{s} = 7$ TeV.

Figure 2.7a shows the charged particle multiplicity as a function of the pseudorapidity. This quantity shows a similar behavior like in the 900 GeV data with an approximately flat shape with a smooth dip in the central pseudorapidity region and decreasing at forward pseudorapidity (starting from $|\eta| < 1.5$). The charged-particle multiplicity at $\sqrt{s} = 7$ TeV per event and unit of pseudorapidity at $|\eta| = 0$ is $5.635 \pm 0.002(stat.) \pm 0.149(syst.)$. All the Monte Carlo tunes predict a charged particle multiplicity 10 - 25% lower than the measured multiplicity. The different tunes have little differences in shapes, but all consistent with the shape in data.

Figure 2.7b shows the charged particle multiplicity as a function of p_T at $\sqrt{s} = 7$ TeV. The p_T spectra agree well with the AMBT1 tune at intermediate p_T from 0.5 to 3 GeV and all MC models agree with the data to within 20% at high p_T (with the exception of ATLAS MC09 tune that reaches 70%) and within 35% at low p_T (with the exception of PYTHIA DW tune that reaches 45%). The largest contribution from diffractive events is expected to be in the lower p_T region.

The charged particle multiplicity distribution per event is shown in figure 2.7c. None of the MC models seems to be able to describe properly the low multiplicity region while for $n_{ch} \geq 20$ AMBT1 agrees well with the data distribution within 10%.

Figure 2.7d shows the average p_T as a function of n_{ch} at $\sqrt{s} = 7$ TeV. The average transverse momentum increases with the number of charged particles, with the slope of the distribution that changes around $n_{ch} = 10$ as in the 900 GeV data. Again the AMBT1 slope is very similar to data and this is

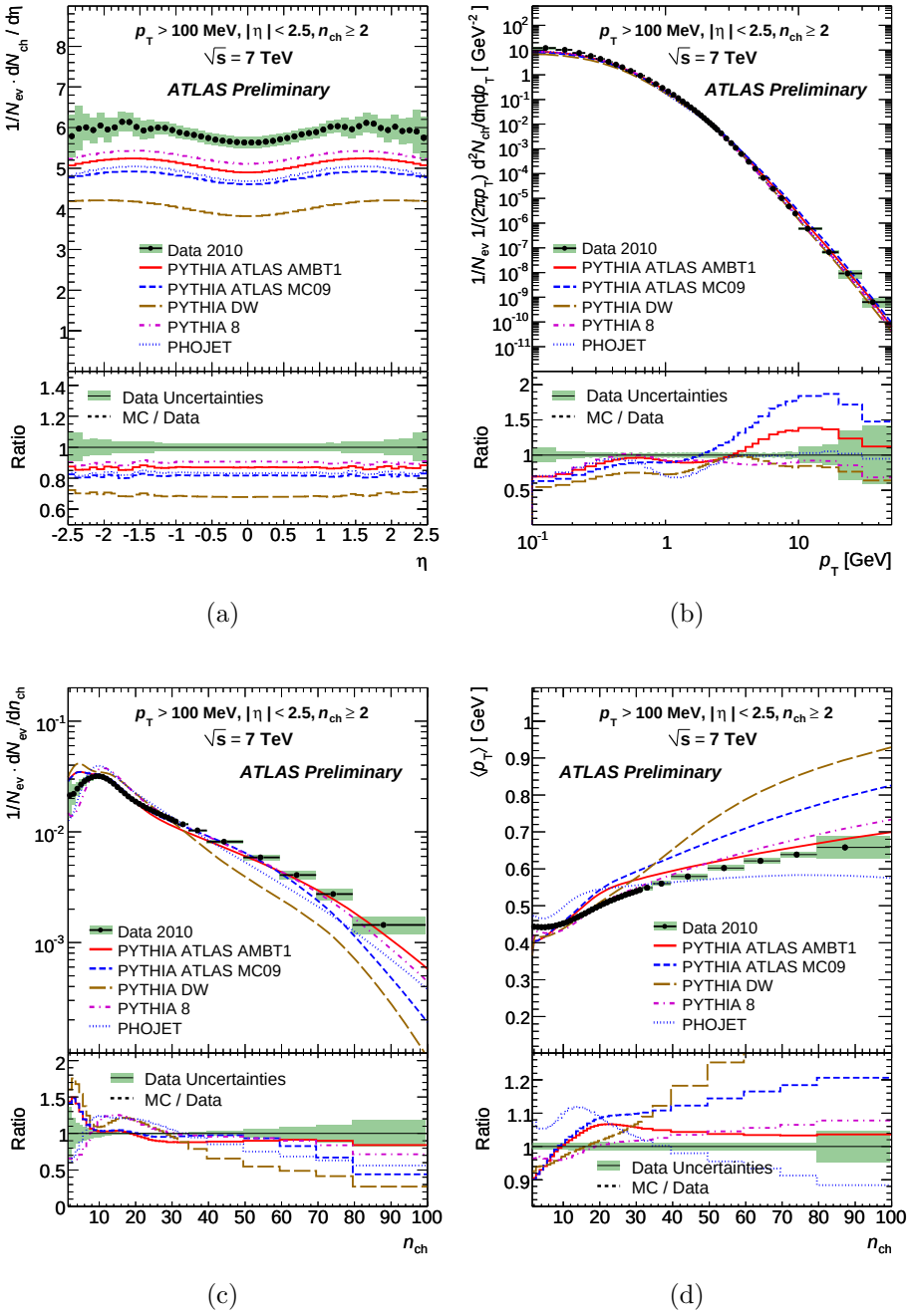

Figure 2.7: Charged particle multiplicities for events with $n_{ch} \geq 2$ within the kinematic range p_T >100 MeV and $|\eta| < 2.5$ at $\sqrt{s} = t$ TeV. The panels show the charged particle multiplicity as a function of the pseudorapidity (a) the charged particle multiplicity as a function of the transverse momentum (b), the charged particle multiplicity (c), and the average transverse momentum as a function of the number of charged particles in the event (d). The markers represent the data and the curves predictions from different Monte Carlo models. The vertical bars represent the statistical uncertainties, while the green shaded bands show the statistical and systematic uncertainties added in quadrature.

valid also for PYTHIA8 Monte Carlo. This effect is strictly correlated in how the diffraction is described in MC simulation models; in fact PYTHIA6 has no hard diffraction included (no tracks produced above 3 GeV and no events with more than 27 charged particles), while PYTHIA8 and PHOJET have this component included.

Multiplicity vs the center of Mass Energy

Figure 2.8 shows the comparison of the charged particle multiplicity at central pseudorapidity versus the center of mass energy of the collisions measured in data with different models, for both the phase-space regions considered. Considering the less inclusive one (n_{ch} $\geq$1 and $p_T > 0.5$ GeV) where the measurements at $\sqrt{s} = 0.9$, 2.36 and 7 TeV are available, all the three ATLAS

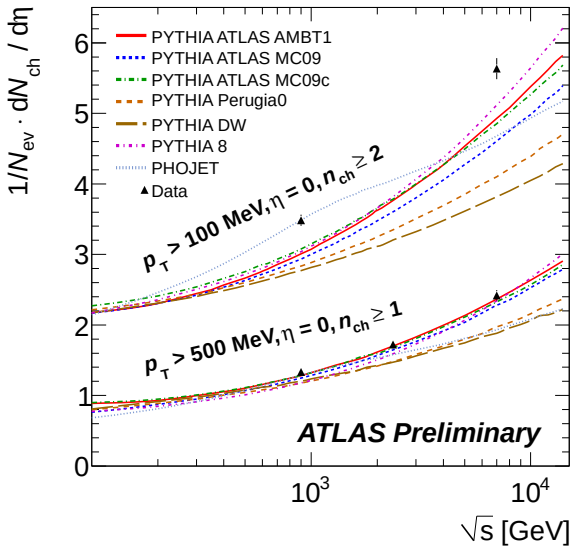

Figure 2.8: Comparison of the ATLAS charged particle multiplicity measurements as a function of the center of mass energy with different Monte Carlo tunes. The result at $\sqrt{s} = 2.36$ TeV is measured using the pixel track method. Both the results from the charged particle multiplicity measurement with the p_T threshold at 500 MeV and at 100 MeV are shown.

PYTHIA tunes describe in an appropriate way the increase of the multiplicity with center of mass energy, with the most accurate description that is given by the AMBT1 tune. DW and Perugia0 tunes and also PHOJET show a slower increase in the multiplicity with the center of mass energy with none of the models that predicts correctly the data multiplicity; only PHOJET gives a correct prediction at $\sqrt{s} = 0.9$ TeV but a lower prediction at $\sqrt{s} = 7$ TeV. In the case of the most inclusive phase-space ($n_{ch} \geq 1$ and $p_T > 0.5$ GeV), all the Monte Carlo generators estimate a lower charged particle multiplicity at central pseudorapidity versus the center of mass energy of the collisions giving still space for further improvements of the tunings. Only PHOJET seems to be in agreement with the point at $\sqrt{s} = 0.9$ TeV, while underestimating the multiplicity at $\sqrt{s} = 7$ TeV.

50 Minimum Bias Physics at LHC at $\sqrt{s} = 900$ GeV and $\sqrt{s} = 7$ TeV

Chapter 3

Reconstruction of K^0_{S} and Λ^0 particles in $\sqrt{s} = 7$ TeV minimum bias data

3.1 Dataset used and event selection

The data used to perform the analysis on K^0_s and Λ^0 correspond to a sample of around 11 million events recorded by the ATLAS detector during the LHC proton-proton runs at the center of mass energy of 7 TeV between March and April 2010 using a minimum bias trigger. These data are equivalent to an integrated luminosity of $190\mu\mathrm{b}^{-1}$. The events, in order to be selected for the analysis, should satisfy the following requirements:

- have all the Inner Detector (ID) sub-systems at the nominal conditions (green data quality flags) and stable beam condition declared by the LHC;

- have passed the Level 1 Minimum Bias Trigger Scintillator (MBTS) single arm trigger;

- have a reconstructed primary vertex;

- not have more than one reconstructed primary vertex in the same bunch crossing (pile-up removal). The events with a second vertex with more than 3 associated tracks are rejected. An example of a pile-up event is show in figure 3.1;

- have at least one track in the event with a Pixel Hit.

The list of runs and the corresponding ranges of good luminosity blocks[1] used for this analysis are reported in table 3.1. The same event selection was applied to the Monte Carlo sample consisting of 20 million non diffractive minimum bias events generated using PYTHIA 6.4.21 generator with the default ATLAS MC09 PYTHIA tune [59] and simulated using the full ATLAS GEANT4 [60] and reconstructed in the identical way of the data. The parameters for this tune are obtained from tuning to the minimum bias and underlying event Tevatron data at 630 GeV and 1.8 TeV. Moreover the MC simulation was

[1] The smallest unit of time for which luminosity is determined in ATLAS is a luminosity block, during which detector conditions are not supposed to change.

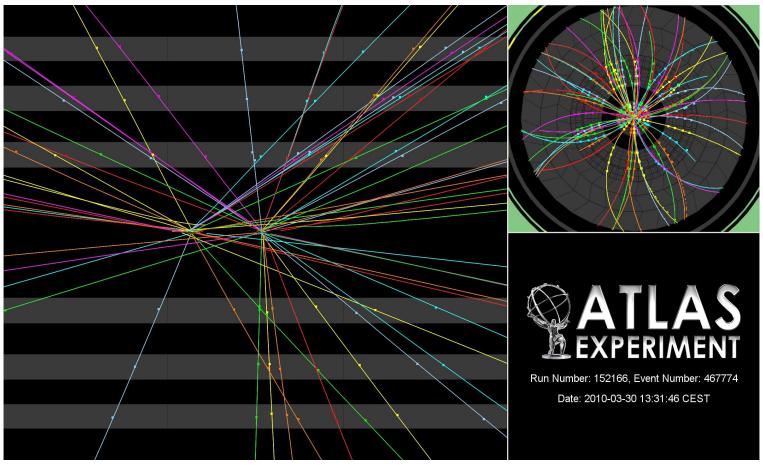

Figure 3.1: A 7 TeV collision event with two reconstructed primary vertices (pileup), collected in the first 7 TeV fill on 30 March 2010 (run 152166). The longitudinal distance between the two vertices amounts to approximately 2.5 cm.

Run Number	lbn range
152166	206-300
152214	159-202
152221	5-167
152345	128-207
152409	124-716
152441	309-671
152508	196-261

Table 3.1: List of the runs and the corresponding range of good luminosity blocks used.

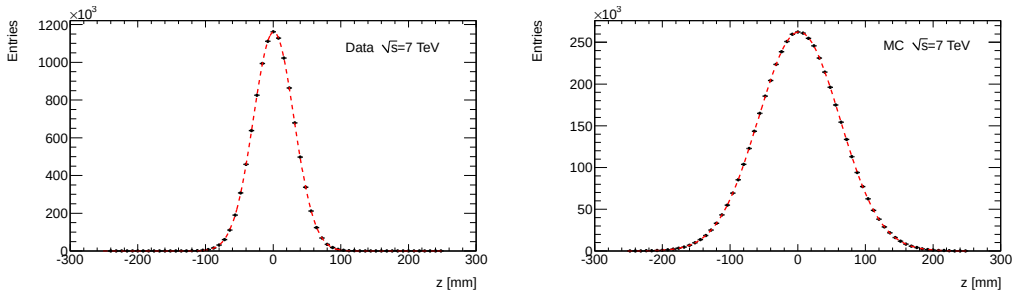

Figure 3.2: Distribution of the longitudinal position (z) for the primary vertex in data (left) and MC (right). The histograms are both fitted with a Gaussian distribution.

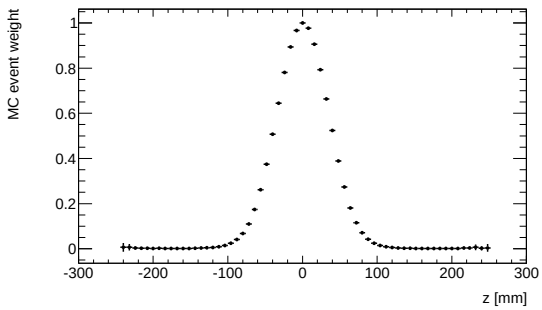

Figure 3.3: Relative MC weight applied in order to reproduce the same distribution for the longitudinal position of the primary vertex.

reweighted due to the fact that the distributions of the longitudinal position (z) for the primary vertex is different between data and MC. The z distribution of the primary vertex in data and MC are shown in figure 3.2 and the relative weight applied is shown in figure 3.3. Both the histograms are fitted with a Gaussian distribution. For data $\sigma = (30.087 \pm 0.007)$ mm while for Monte Carlo simulation $\sigma = (60.04 \pm 0.02)$ mm.

3.2 The Armenteros-Podolanski plot in proton proton collisions at $\sqrt{s} = 7$ TeV

The dynamics of two-body neutral particle decays (commonly defined V^0) can be studied with the Armenteros-Podolanski plot [61]. This method can provide a unique identification of two-body decaying particles by studying the division of the parent's momentum vector between the daughters. Let us consider the decay of a V^0 particle in the laboratory frame and in the V^0 centre-of-mass frame as shown in figure 3.4. The momentum components in the centre-of-mass

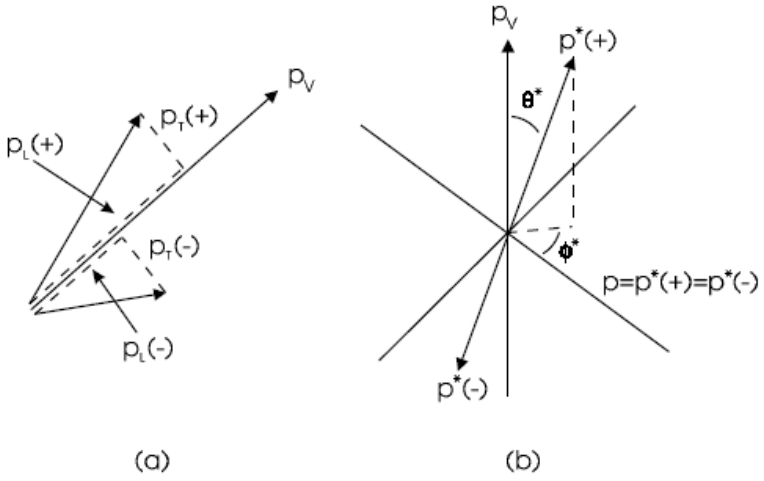

Figure 3.4: Schematic representation of a V^0 particle decay in the laboratory frame and in the V^0 centre-of-mass frame

frame are

$$\begin{aligned} p_L^*(+) &= p^* \cos(\theta^*) \\ p_T^*(+) &= p^* \sin(\theta^*) \\ E^*(+) &= \sqrt{p^{*2} + m^2(+)} \end{aligned} \tag{3.2.1}$$

In order to transform these in the laboratory frame, we can use Lorentz transformations that can be expressed in their matrix form

$$\begin{pmatrix} E \\ p_L \end{pmatrix} = \begin{pmatrix} \gamma & \gamma\beta \\ \gamma\beta & \gamma \end{pmatrix} \begin{pmatrix} E^* \\ p_L^* \end{pmatrix} \qquad p_T = p_T^* \tag{3.2.2}$$

with $\gamma = 1/\sqrt{1-\beta^2}$, being β the velocity of the laboratory in the centre-of-mass rest frame. We get:

$$\begin{aligned} E^{Lab}(+) &= \gamma E^*(+) + \gamma\beta p_L^*(+) \\ p_L^{Lab}(+) = \gamma p_L^*(+) + \gamma\beta E^*(+) &= \gamma p^* \cos(\theta^*) + \gamma\beta E^*(+) \\ p_T^{Lab} = p_T^* &= p^* \sin(\theta^*) \end{aligned} \tag{3.2.3}$$

from which we can write:

$$\begin{aligned} p_L^{Lab}(+) &= \gamma p^* \cos(\theta^*) + \gamma\beta E^*(+) \\ p_L^{Lab}(-) &= -\gamma p^* \cos(\theta^*) + \gamma\beta E^*(-) \end{aligned}$$

$$\begin{aligned} p_L^{Lab}(+) - p_L^{Lab}(-) &= 2\gamma p^* \cos(\theta^*) + \gamma\beta(E^*(+) - E^*(-)) \\ p_L^{Lab}(+) + p_L^{Lab}(-) &= p_L^{Lab} = p_{V^0} = \beta\gamma m_{V^0} \sim \gamma m_{V^0} \end{aligned}$$

The Armenteros-Podolanski variable is than defined as:

$$\alpha = \frac{p_L^{Lab}(+) - p_L^{Lab}(-)}{p_L^{Lab}(+) + p_L^{Lab}(-)} = \frac{2p^* \cos\theta^*}{m_{V^0}} + \frac{E^*(+) - E^*(-)}{m_{V^0}} = \zeta \cos\theta^* + \phi \tag{3.2.4}$$

$$\text{with } \zeta = \frac{2p^*}{m_{V^0}} \text{ , } \phi = \frac{E^*(+) - E^*(-)}{m_{V^0}}$$

and, considering the two relations for $\cos\theta^* = \frac{\alpha-\phi}{\zeta}$ and $\sin\theta^* = \frac{p_T^*}{p^*}$, we find

$$\cos^2\theta^* + \sin^2\theta^* = 1 = \left(\frac{\alpha-\phi}{\zeta}\right)^2 + \left(\frac{p_T^*}{p^*}\right)^2 \tag{3.2.5}$$

The equation 3.2.5 is the equation of an ellipse with center in (ϕ,0) and a semi-axis length ζ in α and of length p^* in p_T. The values for these parameters for $\Lambda^0 \to p^+\pi^-$, $\overline{\Lambda^0} \to p^-\pi^+$ and $K^0_s \to \pi^+\pi^-$ decays are shown in table 3.2.

Decay	ζ	p^* [GeV]	α_{min}	α_{max}	ϕ
$K^0_s \to \pi^+\pi^-$	0.8282	0.206	-0.828	0.828	0.
$\Lambda^0 \to p^+\pi^-$	0.179	0.101	0.515	0.873	0.694
$\overline{\Lambda^0} \to p^-\pi^+$	0.179	0.101	-0.873	-0.515	-0.694

Table 3.2: Armenteros-Podolanski quantities for K^0_s, Λ^0 and $\overline{\Lambda^0}$ decays.

Using the $\sim 190\mu b^{-1}$ minimum bias proton-proton collision data taken at $\sqrt{s} = 7$ TeV, the Armenteros-Podolanski plot has been reconstructed. In order to produce this plot, all reconstructed V^0 candidates fulfilling the following requirements have been used:

- transverse flight distance of the V^0 greater than 4 mm;
- the chi-square of the V^0 vertex fit (with one degree of freedom) should satisfy the condition $\chi^2 < 15$;
- the cosine of the angle $\theta_{pointing}$ between the reconstructed V^0 momentum vector and V^0 flight direction in the transverse plane should satisfy the condition $\cos(\theta_{pointing}) < 0.999$.

while, for the tracks fitted into a common secondary decay vertex, the following quality criteria should be satisfied:

- transverse momentum of the track p_T >100 MeV;

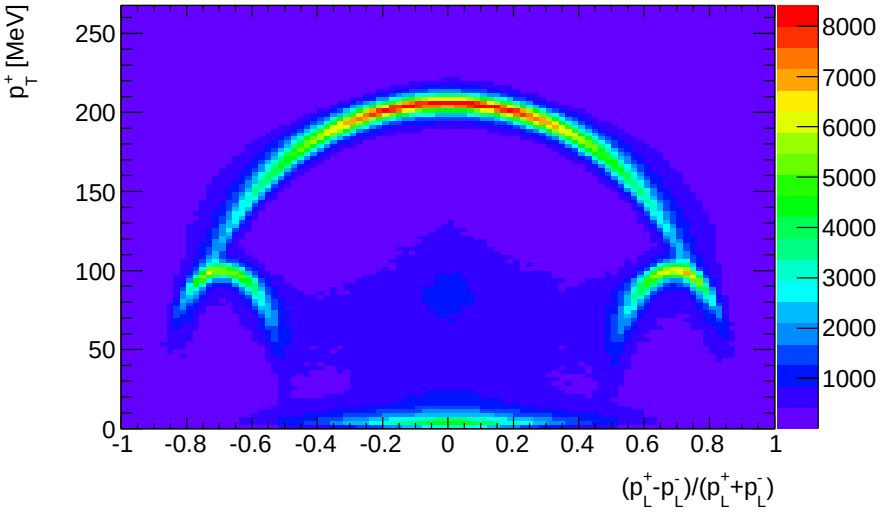

Figure 3.5: Podolanski-Armenteros plot for the reconstructed V^0 candidates in $\sim 190\mu\text{b}^{-1}$ proton proton collisions at $\sqrt{s} = 7$ TeV.

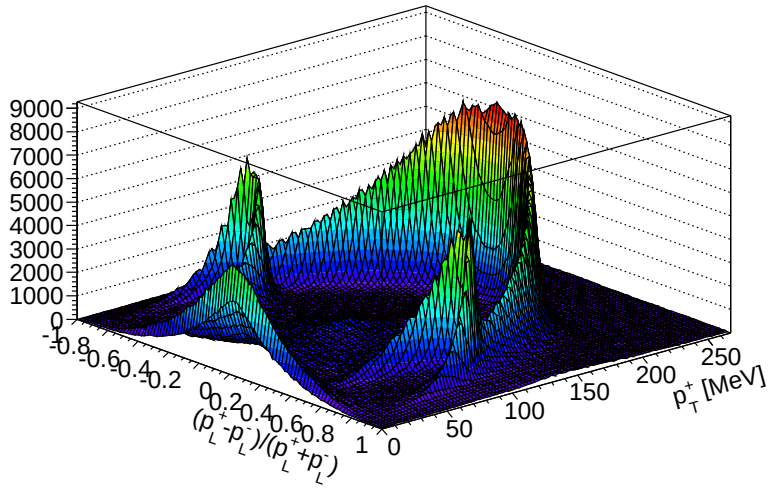

Figure 3.6: 3-D version of the Podolanski-Armenteros plot for the reconstructed V^0 candidates in $\sim 190\mu\text{b}^{-1}$ proton proton collisions at $\sqrt{s} = 7$ TeV.

- at least two silicon hits (Pixel hits + SCT hits).

Figures 3.5 and 3.6 shows the Armenteros-Podolanski plot: the transverse momentum of the positive tracks is plotted versus the asymmetry of longitudinal momenta of both tracks. Transverse and longitudinal momenta are defined with respect to the momentum sum of the two tracks (i.e. the momentum direction of the V^0 candidate), and are given in the laboratory frame. The K^0_s, the Λ^0 and the $\overline{\Lambda^0}$ ellipses are clearly visible. The maximum value for p_T is reached when the decay products are perpendicular to the direction of the parent particle in rest frame. For K^0_s, that have identical mass daughters, this happens at $\alpha = (p_L(+) - p_L(-))/(p_L(+) + p_L(-)) = 0$ Moreover the reconstructed photon conversions $\gamma \to e^+e^-$ that populate the region at low-p_T centered at $\alpha = 0$ are also visible in the plot.

3.3 Monte Carlo matching between track and particle

To evaluate the reconstruction efficiency or to discriminate at the reconstruction level in MC simulation between the signal and the background component for the V^0 candidates, it is necessary to associate the reconstructed daughter track coming from a V^0 candidate with the MC truth particle generated from a V^0 decay. Unfortunately there is not a unique one-to-one relation between a reconstructed track and a generated particle because tracks can be formed using hits produced in the detector by different particles; in addition, a bad tracking resolution can be a further drawback in the track to particle matching. The techniques commonly used in ATLAS for the association between tracks and particles are three: a hit based matching, a cone matching and a hybrid cone-hit matching technique.

Hit Matching

The hit based matching technique uses an association between the hits and the truth charged particles done at the digitization level; in particular it compares the hits on the track in each sub-detector of the ATLAS Inner Detector and the number of hits produced by the truth particle forming a matching probability. Moreover, since the number of the hits that contributes to the reconstructed track parameters and the average number of hits per track varies a lot between the different sub-detectors, they are weighted according to the following formula:

$$P = \frac{10 \cdot N_{\text{Pix}}^{\text{common}} + 5 \cdot N_{\text{SCT}}^{\text{common}} + 1 \cdot N_{\text{TRT}}^{\text{common}}}{10 \cdot N_{Pix}^{\text{track}} + 5 \cdot N_{SCT}^{\text{track}} + 1 \cdot N_{TRT}^{\text{track}}} \tag{3.3.1}$$

where

- $N_{\text{det}}^{\text{common}}$ corresponds to the number of hits in a specific sub-detector which are part of both the truth and reconstructed track;
- $N_{\text{det}}^{\text{track}}$ is the number of hits in a specific sub-detector which are part of the reconstructed track.

This method is independent from the detector resolutions, but does not take into account tracks that are formed by hits from the decay product of a primary charged particle even if the track describes perfectly the momentum of this particle. Moreover, P is a discrete variable and it is more difficult to interpret it, especially for low momentum tracks.

Cone Matching

The cone based matching requires that the truth particle and the reconstructed track propagate in the same direction. The relevant quantity in this case is the ΔR distance that is defined as

$$\Delta R = \sqrt{\Delta\eta^2 + \Delta\phi^2} \tag{3.3.2}$$

where $\Delta\eta$ and $\Delta\phi$ corresponds to the difference between the truth particle and the reconstructed track in η or in the azimuthal angle ϕ. The matching

is performed if in a certain ΔR distance a reconstructed track is found for a given truth particle. If there is an ambiguity in the matching of a truth particle to a track or vice versa, the closest match is taken. In some cases, there could be a fake matching, especially for reconstructed track with low transverse momentum ($p_T < 500$ MeV) and , in this case, there will be no hit in common between the truth particle and the reconstructed track.

Hybrid Hit-Cone Matching

Using a larger cone for the matching, as it is needed for low p_T tracks, the number of fake matching increase. In order to reduce this fake contamination, a further requirement on a common hit between the track and the truth particle can be made. It has to be noticed that most of the tracks that have an hybrid hit-cone matching and not a hit matching are pions that decay in flight to muons.

The simple cone matching is not straightforward for secondary particles that are produced far away from the primary vertex (like the pions coming from a K^0_s decay). This is due to the fact that the ϕ value of a track depends on the point where the particle is produced for the presence of the magnetic field. For a secondary particle, the ΔR should be evaluated at the production vertex of the truth particle instead of the primary vertex. So, in this case, a simple hit matching is better for the truth particle to track matching.

3.4 K^0_s Reconstruction

In order to reconstruct K^0_s candidates decaying into two opposite charged pions, pairs of tracks with opposite charge that are not used for the primary vertex fit are refitted together to establish a common secondary decay vertex. The tracks quality requirements applied to both tracks are:

- transverse momentum of the track p_T >100 MeV;

- at least two silicon hits (Pixel hits + SCT hits).

Moreover, in order to reduce the combinatorial background, a set of requirements are also applied to the K^0_s candidate:

- the chi-square of the vertex fit (with one degree of freedom) has to satisfy the condition $\chi^2 < 15$. That corresponds to a cut on the probability of 0.01%;

- the transverse flight distance is required to be bigger than 4 mm. This is the distance in the x-y transverse plane (orthogonal to the beam axis) between the reconstructed collision vertex and the K^0_s candidate decay point (secondary vertex);

- the point angle $\theta_{pointing}$, defined as the angle in the transverse plane between the reconstructed K^0_s momentum vector and K^0_s flight direction, has to satisfy the condition $\cos(\theta_{pointing}) > 0.999$.

All these cuts are applied also to the non diffractive minimum bias Monte Carlo sample. Moreover, in the analysis on the simulated sample, a hit based matching was applied. Thus it is possible to check if two tracks associated to a K^0_s candidate decay are matched to a true generated π^+ and π^- pair coming from a $K^0_s \to \pi^+\pi^-$ decay. This allows to distinguish in the MC simulation the signal and the background component in the invariant mass and kinematic distributions of the K^0_s candidates. Figure 3.7 shows the transverse flight distance and the $\cos(\theta_{pointing})$ distributions using a limited part of the MC statistics available for signal ($K^0_s \to \pi^+\pi^-$ decays reconstructed and matched with the Monte Carlo truth) and the background ($K^0_s \to \pi^+\pi^-$ candidates reconstructed and unmatched with the Monte Carlo truth) when all the other cuts (as listed before) are applied.

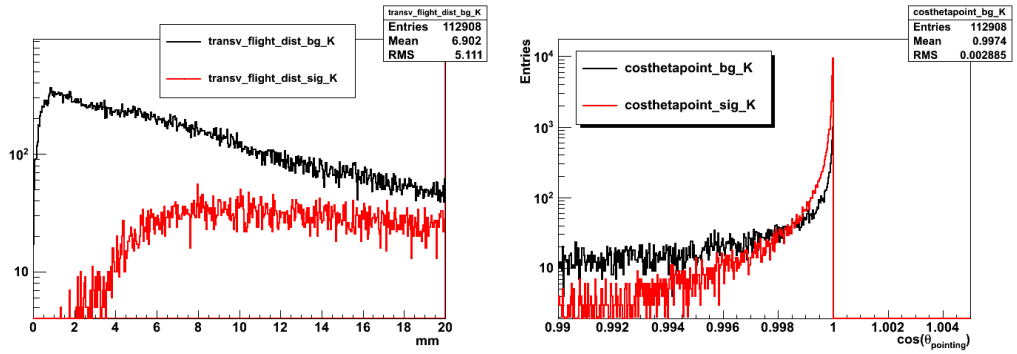

Figure 3.7: (left) Transverse flight distance distribution for reconstructed K^0_s candidate matched (red) and unmatched (black) with the MC truth with all the other cuts applied. (right) $\cos(\theta_{pointing})$ distribution for reconstructed K^0_s candidate matched (red) and unmatched (black) with the MC truth with all the other cuts applied.

3.4.1 K^0_s Mass distribution

For all the $K^0_s \to \pi^+\pi^-$ decay candidates that pass the event selection described in section 3.1 and the specific K^0_s selection, the invariant mass of the two tracks coming out from the reconstructed secondary vertex has been computed assuming the pion mass hypothesis for both tracks. Figure 3.8 show the distribution of the invariant mass for the reconstructed K^0_s candidate in data and Monte Carlo simulation. In this plot, the truth-matched signal and background candidates are separately normalized in order to match the different signal-to-background ratio in the data: the background level has been fixed using the number of candidates in two sidebands (400-440 MeV and 550-600 MeV) and then the MC signal has been normalized using the difference between the data and the MC background component previously fixed in a mass window region of ± 20 MeV around the K^0_s PDG mass value. Invariant mass distributions are also obtained separately for the barrel and the endcap regions requiring that both pions associated to a K^0_s candidate have $|\eta(\pi)| < 1.2$ (barrel) or $|\eta(\pi)| > 1.2$ (endcap). They are shown in figure 3.9. A fit has been done in order to evaluate the position of the signal mass peak and its width.

The function used to fit the mass distributions is the following

$$p_0 \cdot e^{\left(-\frac{1}{2}\left(\frac{x-p_1}{p_2}\right)^2\right)} + p_3 \cdot e^{\left(-\frac{1}{2}\left(\frac{x-p_1}{p_4}\right)^2\right)} + p_5 + p_6 \cdot x + p_7 \cdot x^2 + p_8 \cdot x^3 \quad (3.4.1)$$

that corresponds to a combination of two Gaussian for the signal component and a third-order polynomial function for the combinatorial background description. The means of the two Gaussian are constrained to be the same. In table 3.3 the results of the fit in terms of mean position and width at half maximum divided by 2.35 (in order to obtain the equivalent σ assuming a simple Gaussian distribution) are reported. The uncertainties reported for the mean are purely statistical. As expected the endcap regions have a lower momentum resolution and this is reflected in the size of the width that is higher with respect to the barrel region. The mean and width obtained fitting the data are consistent with MC simulation; moreover the mean of the mass peak is also consistent with the PDG [62] value. This level of agreement demonstrates a good accuracy of the track momentum scale and an excellent modeling of the 2T solenoidal magnetic field in the Inner Detector that has been mapped with a precision of $\sim$ 0.4 mT [63].

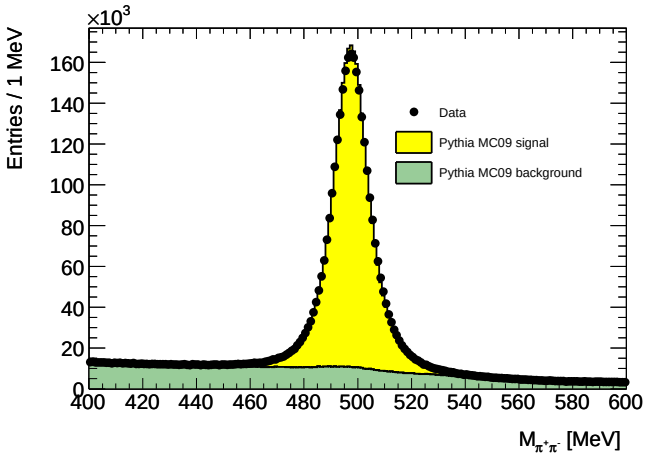

Figure 3.8: Invariant mass distribution for reconstructed K^0_s candidate compared between data and MC simulation. Black circles are data, the histograms show Monte Carlo simulation (normalized to data) .

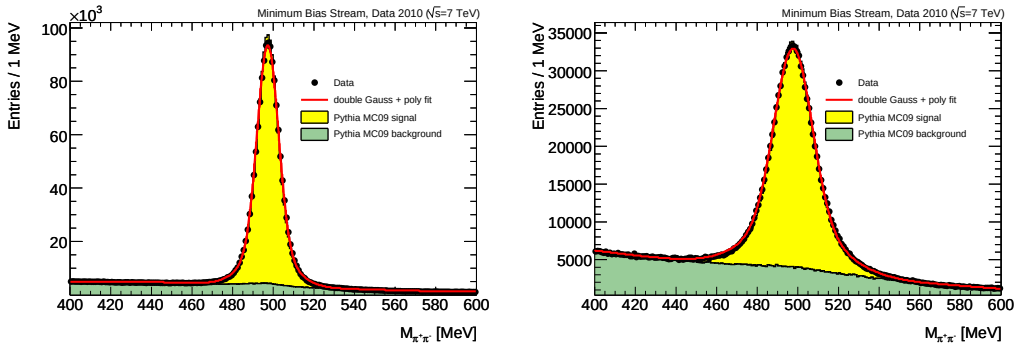

Figure 3.9: Invariant mass distribution for reconstructed K^0_s candidate compared between data and MC simulation in the barrel region (left) with both tracks satisfying $|\eta| < 1.2$ and and in the endcap regions with both tracks satisfying $|\eta| > 1.2$. Black circles are data, the histograms show Monte Carlo simulation (normalized to data) while the red line is the line-shape function fitted to data.

	Barrel		Endcap		PDG
	mean [MeV]	width [MeV]	mean [MeV]	width [MeV]	mass [MeV]
K^0_s Data	497.427 ± 0.006	5.60	497.797 ± 0.016	10.45	497.614 ± 0.024
K^0_s MC	497.329 ± 0.006	5.42	497.868 ± 0.016	10.14	497.614 ± 0.024

Table 3.3: Fit results for data and Monte Carlo sample for both K^0_s invariant mass distributions in barrel and endcap regions. The "width" in the table correspond to the full width at half maximum divided by 2.35.

3.4.2 K^0_s Kinematic distributions

The kinematic distributions (pseudorapidity, azimuthal angle, proper decay time, transverse momenta) for K^0_s candidates have been obtained looking at the kinematic properties of candidates in the mass window $|M_{K^0_s} - M_{PDG}| < 20$ MeV and compared with the MC simulation expectations. The MC distributions of the truth matched signal and the unmatched (background) candidates

have been normalized using the signal-to-background ratio extracted from the invariant mass distribution in the equivalent mass window, without splitting the barrel and endcap regions. No correction for detector effects like efficiency or resolution are applied.

Pseudorapidity distribution

Figure 3.10 shows the pseudorapidity distribution of the momentum reconstructed for K^0_S candidates in data and Monte Carlo simulation in the mass window $|M_{K^0_s} - M_{PDG}| < 20$ MeV. The distribution is consistent with MC simulation within a few percent in most of the bins that correspond to different detector regions and the overall agreement is within 10%.

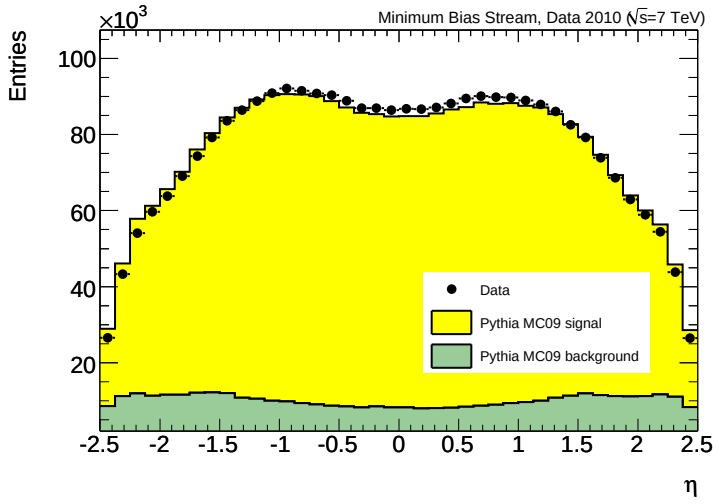

Figure 3.10: Pseudorapidity distribution of the vector momentum of K^0_s candidate reconstructed in data and MC simulation in the invariant mass window $|M_{K^0_s} - M_{PDG}| < 20$ MeV. Signal and background components in MC simulation are normalized to data.

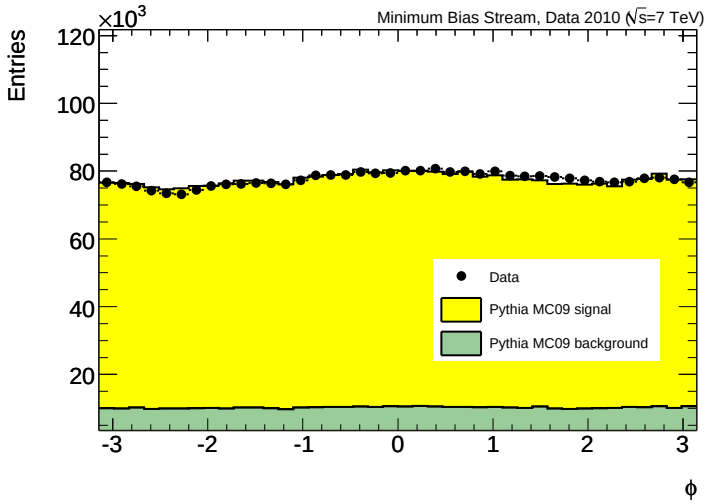

Figure 3.11: Distribution of the azimuthal angle (ϕ) of the vector momentum of K^0_s candidate reconstructed in data and MC simulation in the invariant mass window $|M_{K^0_s} - M_{PDG}| < 20$ MeV. Signal and background components in MC simulation are normalized to data.

Azimuthal angle distribution

In figure 3.11 is shown the azimuthal angle ϕ of the vector momentum for reconstructed K^0_s candidate in the $|M_{K^0_s} - M_{PDG}| < 20$ MeV mass window for data and MC simulation. The agreement between data and simulation is within few percent. A modulation of the ϕ distribution is visible in both data and MC: this is mainly a geometrical effect due to the beamspot displacement in the transverse plane.

Proper decay time distribution

Figure 3.12 shows the proper decay time distribution for K^0_s candidate in the $|M_{K^0_s} - M_{PDG}| < 20$ MeV mass window for data and simulation in linear and

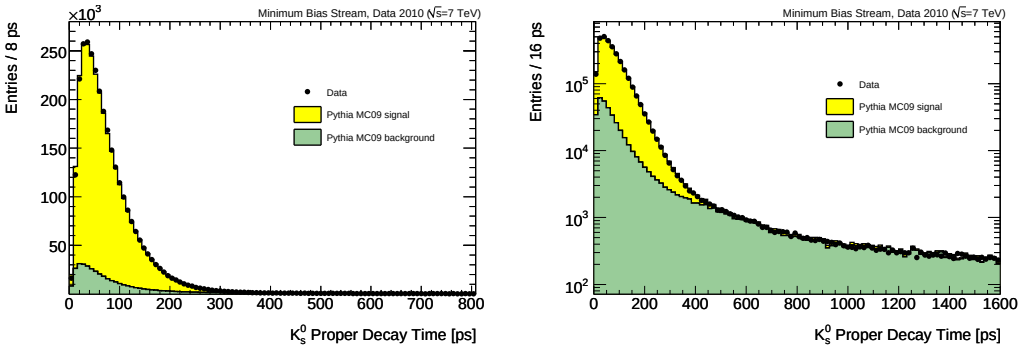

Figure 3.12: Distribution of the proper decay time for K^0_s candidate reconstructed in data and MC simulation for the invariant mass window $|M_{K^0_s} - M_{PDG}| < 20$ MeV. Signal and background components in MC simulation are normalized to data. Normal scale (left) and log scale (right) demonstrate good agreement between data and simulation.

logarithmic scale. The proper decay time for K^0_s is defined as

$$t = \frac{l}{c\beta\gamma} \qquad \gamma \equiv \frac{1}{\sqrt{1-\beta^2}} \tag{3.4.2}$$

with l that corresponds to the three dimensional decay length, $c\beta$ is the K^0_s velocity and γ is the Lorentz boost of the K^0_s in the lab frame. Since $\beta\gamma = p_{K^0_s}/M_{K^0_s}$, it can be rewritten as

$$t = \frac{l \cdot M_{K^0_s}}{c \cdot p_{K^0_s}} \tag{3.4.3}$$

The distribution in data events is in good agreement with MC simulation, also in the background dominated region. The same level of agreement is obtained using the two-dimension information replacing the flight distance in the equation 3.4.3 with the transverse flight distance and the K^0_s momentum with the transverse momentum p_T.

Transverse Momentum distribution

The distributions of the transverse momentum of K^0_s candidate reconstructed in the mass window $|M_{K^0_s} - M_{PDG}| < 20$ MeV in linear and logarithmic scale

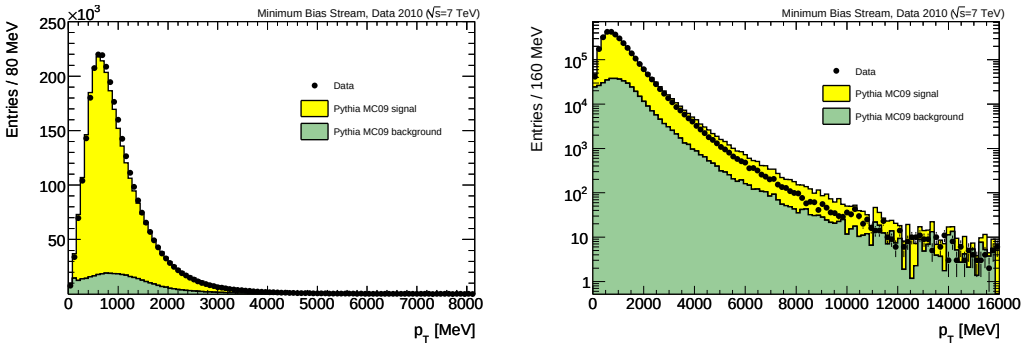

Figure 3.13: Distribution of transverse momenta for K^0_s candidate reconstructed in data and MC simulation for the invariant mass window $|M_{K^0_s} - M_{PDG}| < 20$ MeV. Signal and background components in MC simulation are normalized to data. Normal scale (left) and log scale (right) demonstrate good agreement between data and simulation.

are shown in figure 3.13. The MC simulation shows a harder p_T spectra compared to the data. Given the pretty good agreement of the proper decay time distribution between data and MC simulation in which are involved both the momentum and the flight distance of K^0_s candidates, the disagreement in the p_T spectrum seems mostly related to a non accurate description of the K^0_s transverse momentum distribution in MC generator.

3.5 Λ^0 and $\overline{\Lambda^0}$ reconstruction

The reconstruction of the $\Lambda^0 \to p^+\pi^-$ and $\overline{\Lambda^0} \to p^-\pi^+$ has been performed using, as in the K^0_s reconstruction, tracks with opposite charge refitted together into a common decay vertex. The track quality requirements applied to both tracks are:

- transverse momentum of the track p_T >100 MeV;
- at least two silicon hits (Pixel hits + SCT hits).

The same cut on the chi-square of the vertex fit $\chi^2 < 15$ as in the K^0_s candidate reconstruction has been applied. The other cuts used in order to reduce the combinatorial background are:

- the flight distance is required to be bigger than 30 mm;
- the pointing angle $\theta_{pointing}$, defined as the angle in the transverse plane between the reconstructed Λ^0 ($\overline{\Lambda^0}$) momentum vector and Λ^0 ($\overline{\Lambda^0}$) flight direction, should satisfy the condition $\cos(\theta_{pointing}) > 0.9998$.

Figure 3.14 shows the flight distance and the $\cos(\theta_{pointing})$ distributions for reconstructed Λ^0 candidate matched and unmatched with MC truth in a mass window of 30 MeV around the PDG Λ^0 mass value (1115.683 MeV).

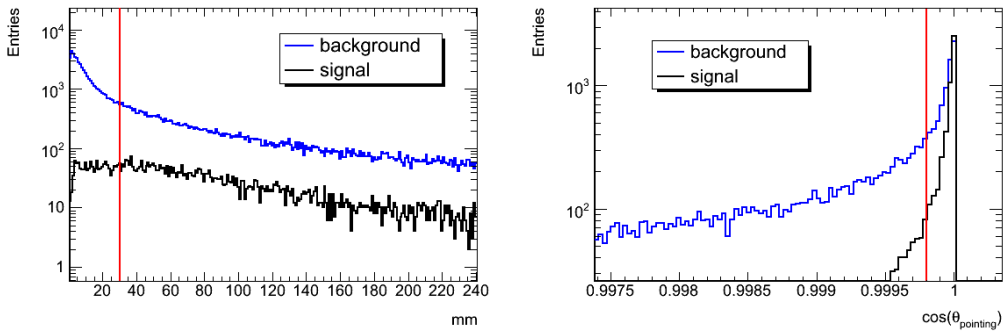

Figure 3.14: (left) Flight distance distribution for reconstructed Λ^0 candidate matched (black) and unmatched (blue) with the MC truth with all the other cuts applied. (right) $\cos(\theta_{pointing})$ distribution for reconstructed Λ^0 candidate matched (red) and unmatched (black) with the MC truth with all the other cuts applied.

3.5.1 Λ^0 and $\overline{\Lambda^0}$ Mass distributions

For all the candidates that pass the cuts described in the previous section, the invariant mass has been computed. Moreover, for each candidate the mass is calculated with two hypotheses: the proton-pion or the pion-proton

hypothesis for the two daughter tracks. In order to separate $\Lambda^0 \to p^+\pi^-$ from $\overline{\Lambda^0} \to p^-\pi^+$ decays, the track associated to a selected secondary vertex with the highest transverse momentum is taken as proton and the other one is taken as pion. In fact, since the proton is much more massive than the pion, it almost always has at least three times the momentum of the pion. This allows to choose the correct hypothesis while the charge of the highest transverse momentum track is used to distinguish the Λ^0 from the $\overline{\Lambda^0}$ candidates. Figures 3.15 and 3.16 show respectively the invariant mass distribution of Λ^0 and $\overline{\Lambda^0}$ candidates in data and Monte Carlo simulation. The truth-matched signal and background candidate are separately normalized to data using the same procedure adopted for the K^0_s candidates using a mass window of ± 7 MeV around the Λ^0 PDG mass value. Figures 3.17 shows the Λ^0 invariant mass distribution separately for barrel and endcap regions requiring that both p^+ and π^- tracks are reconstructed with $|\eta(p^+, \pi^-)| < 1.2$ and $|\eta(p^+, \pi^-)| > 1.2$ respectively. Similar invariant mass distributions with the same condition applied to the p^- π^+ tracks from reconstructed $\overline{\Lambda^0}$ candidates in data and

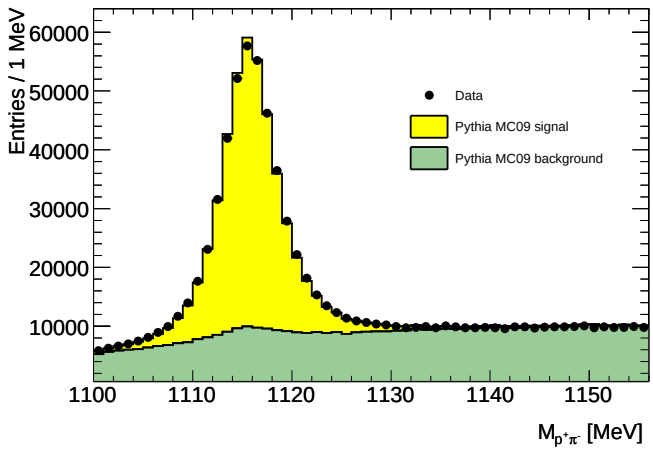

Figure 3.15: Invariant mass distribution for reconstructed Λ^0 candidate in p-p collision at $\sqrt{s} = 7$ TeV compared between data and MC simulation. Black circles are data, the histograms show MC simulation (normalized to data).

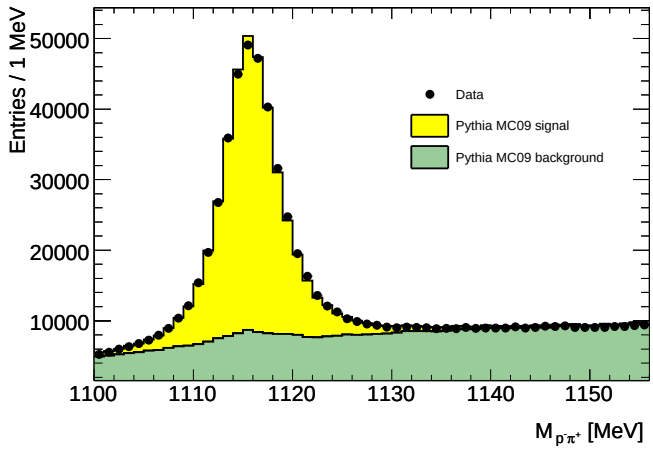

Figure 3.16: Invariant mass distribution for reconstructed $\overline{\Lambda^0}$ candidate in p-p collision at $\sqrt{s} = 7$ TeV compared between data and MC simulation. Black circles are data, the histograms show MC simulation (normalized to data).

simulation are shown in figure 3.18. The function defined in 3.4.1 is used to fit both the data and MC invariant mass distribution for Λ^0 and $\overline{\Lambda^0}$ candidates reconstructed in the barrel and in the endcap region. The results of the fits are shown in the table 3.4. The mean and width for both Λ^0 and $\overline{\Lambda^0}$ obtained fitting the data are consistent with MC simulation; moreover the mean of the mass peaks are also consistent with the PDG [62] value.

	Barrel		Endcap		PDG
	mean [MeV]	width [MeV]	mean [MeV]	width [MeV]	mass [MeV]
Λ^0 Data	1115.73 ± 0.01	2.28	1115.78 ± 0.02	3.84	1115.683 ± 0.006
Λ^0 MC	1115.68 ± 0.01	2.18	1115.78 ± 0.02	3.68	1115.683 ± 0.006
$\overline{\Lambda^0}$ Data	1115.79 ± 0.01	2.32	1115.79 ± 0.02	3.87	1115.683 ± 0.006
$\overline{\Lambda^0}$ MC	1115.71 ± 0.01	2.19	1115.79 ± 0.02	3.69	1115.683 ± 0.006

Table 3.4: Fit results for data and Monte Carlo sample for both Λ^0 and $\overline{\Lambda^0}$ invariant mass distributions in barrel and endcap regions. The "width" in the table correspond to the full width at half maximum divided by 2.35.

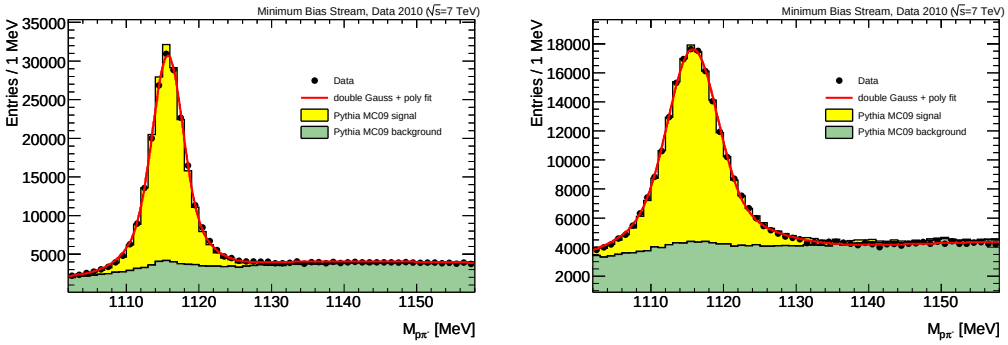

Figure 3.17: Invariant mass distribution for reconstructed Λ^0 candidate compared between data and MC simulation in the barrel region (left) with both tracks satisfying $|\eta| < 1.2$ and and in the endcap regions (right) with both tracks satisfying $|\eta| > 1.2$. Black circles are data, the histograms show Monte Carlo simulation (normalized to data) while the red line is the line-shape function fitted to data.

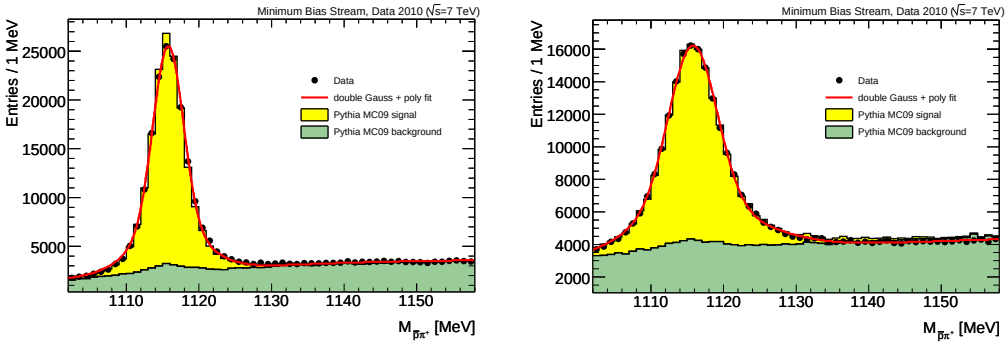

Figure 3.18: Invariant mass distribution for reconstructed $\overline{\Lambda^0}$ candidate compared between data and MC simulation in the barrel region (left) with both tracks satisfying $|\eta| < 1.2$ and and in the endcap regions (right) with both tracks satisfying $|\eta| > 1.2$. Black circles are data, the histograms show Monte Carlo simulation (normalized to data) while the red line is the line-shape function fitted to data.

3.5.2 Λ^0 and $\overline{\Lambda^0}$ Kinematic distributions

The kinematic distributions (pseudorapidity, ϕ, proper decay time and p_T) for both Λ^0 and $\overline{\Lambda^0}$ baryons candidates reconstructed in data within a mass window of ± 7 MeV around the Λ^0 ($\overline{\Lambda^0}$) mass PDG value have been studied and compared with the Monte Carlo simulation. The MC distributions of the truth matched signal and the unmatched (background) candidates have been normalized using the signal-to-background ratio extracted from the invariant mass distributions in the equivalent mass window, without splitting the barrel and endcap regions, applying the same procedure used for K^0_s candidates. No correction of detector effects like efficiency or resolution is applied.

Pseudorapidity distribution

Figure 3.19 shows the pseudorapidity distribution of the momentum reconstructed for Λ^0 and $\overline{\Lambda^0}$ candidates in data and Monte Carlo simulation in the mass window $|M_{\Lambda^0} - M_{PDG}| < 7$ MeV. The distribution is consistent with MC simulation within a few percent in most of the bins that correspond to different detector regions and the overall agreement is within 10%.

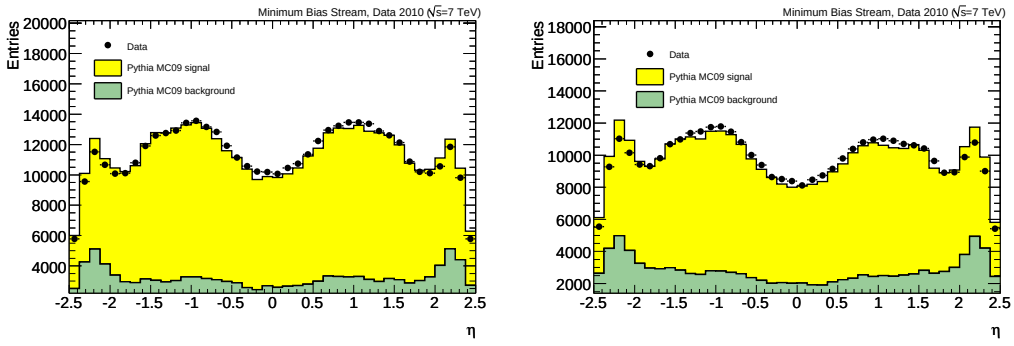

Figure 3.19: The pseudorapidity of the momentum vector of Λ^0 (left) and $\overline{\Lambda^0}$ (right) candidates with reconstructed invariant mass within 7 MeV of the PDG value for data and the MC sample, normalized to the data.

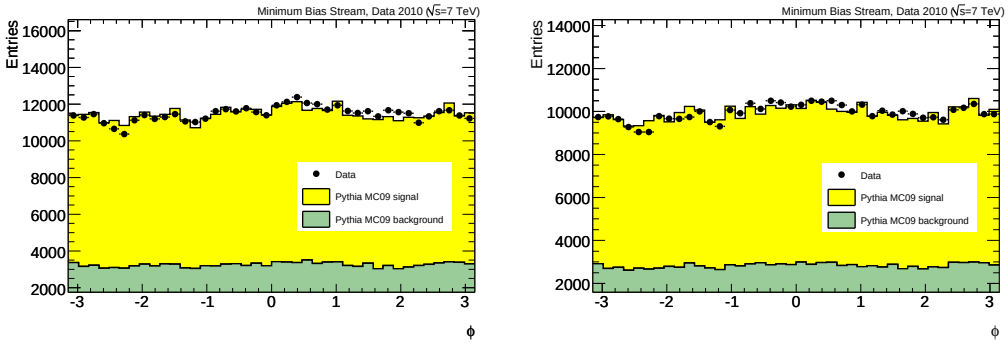

Figure 3.20: Distribution of the azimuthal angle (ϕ) of the vector momentum of Λ^0 (left) and $\overline{\Lambda^0}$ (right) candidate reconstructed in data and MC simulation for the invariant mass window $|M_{\Lambda^0} - M_{PDG}| < 7$ MeV. Signal and background components in MC simulation are normalized to data.

Azimuthal angle distribution

In figure 3.20 are shown the azimuthal angle ϕ of the vector momentum for reconstructed Λ^0 and $\overline{\Lambda^0}$ candidates in the $|M_{\Lambda^0} - M_{PDG}| < 7$ MeV mass window for data and MC simulation. The agreement between data and simulation is within few percent. A similar modulation of the ϕ distribution is visible as in the K^0_s case in both data and MC: this is mainly a geometrical effect due to the beamspot displacement on the transverse plane.

Proper decay time distribution

The proper decay time distribution for Λ^0 and $\overline{\Lambda^0}$ in data and MC are shown respectively in figures 3.21 and 3.22. The distributions in data in both cases are in good agreement with MC simulation in the signal dominated region (up to ∼500 ps) while the agreement is worse in the background dominated region. Also using the transverse quantities (transverse flight distance and p_T) for the proper decay time evaluation, the conclusions are the same in terms of agreement between data and simulation.

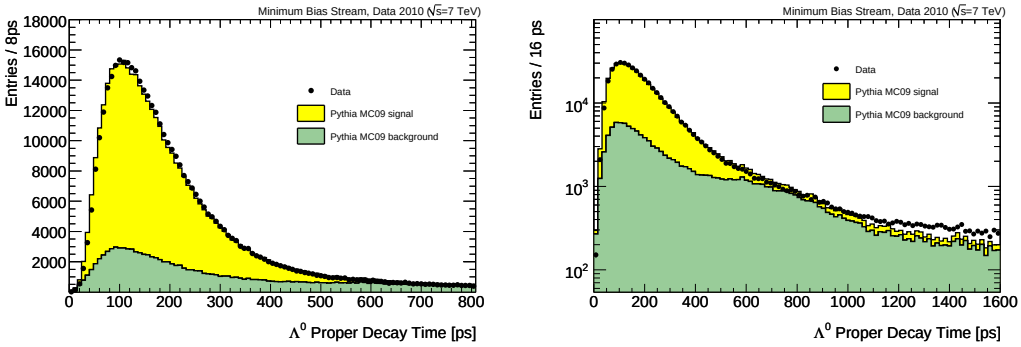

Figure 3.21: Distribution of the proper decay time for Λ^0 candidate reconstructed in data and MC simulation in the invariant mass window $|M_{\Lambda^0} - M_{PDG}| < 7$ MeV in normal scale (left) and log scale (right). Signal and background components in MC simulation are normalized to data.

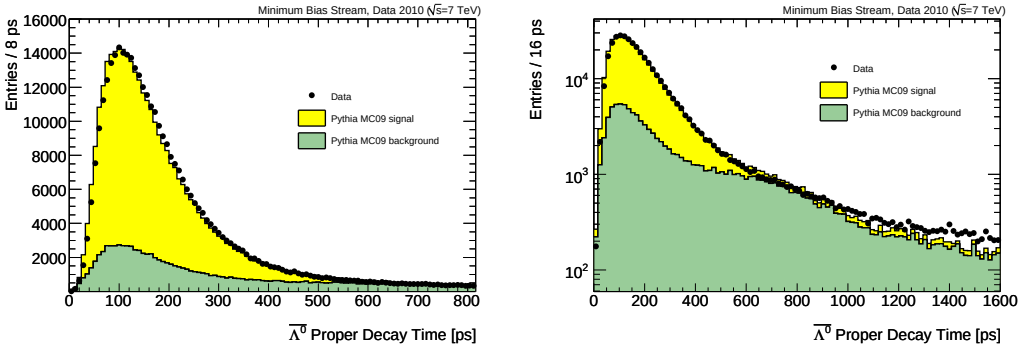

Figure 3.22: Distribution of the proper decay time for $\overline{\Lambda^0}$ candidate reconstructed in data and MC simulation for the invariant mass window $|M_{\overline{\Lambda^0}} - M_{PDG}| < 7$ MeV in normal scale (left) and log scale (right). Signal and background components in MC simulation are normalized to data.

Transverse Momentum distribution

The distributions of the transverse momentum of Λ^0 and $\overline{\Lambda^0}$ candidate in linear and logarithmic scale are shown in figure 3.23 and 3.24. The MC simulation shows a harder p_T spectra with respect to data for both Λ^0 and $\overline{\Lambda^0}$, like in the case of the K^0_s. The conclusion on how well the spectra is described in MC

simulation is less straightforward than in K^0_s case since the proper decay time distribution for Λ^0 and $\overline{\Lambda^0}$ do not have the same level of agreement between data and MC.

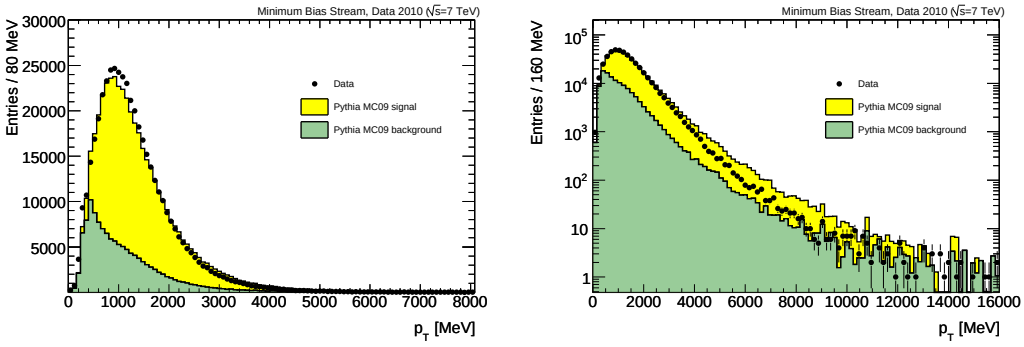

Figure 3.23: Distribution of transverse momenta for Λ^0 candidate reconstructed in data and MC simulation in the invariant mass window $|M_{\Lambda^0} - M_{PDG}| < 7$ MeV. Signal and background components in MC simulation are normalized to data.

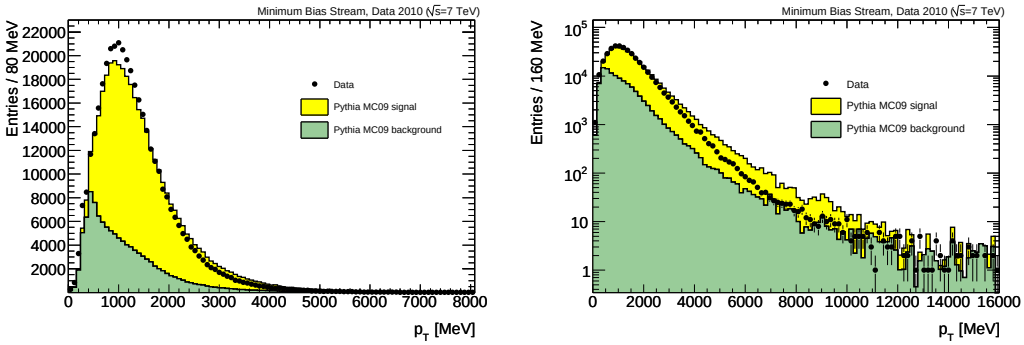

Figure 3.24: Distribution of transverse momenta for $\overline{\Lambda^0}$ candidate reconstructed in data and MC simulation in the invariant mass window $|M_{\overline{\Lambda^0}} - M_{PDG}| < 7$ MeV. Signal and background components in MC simulation are normalized to data.

3.6 Correlations between strangeness production and charged multiplicity distributions

Some additional information related to the strangeness production processes in proton proton collisions at $\sqrt{s} = 7$ TeV can be extracted looking at the correlation with some general properties of the minimum bias events like the charged particle multiplicity.
The "good track" definition used to calculate the number of the charged tracks for each event is the same of the one used in the minimum bias multiplicity studies:

- $p_T > 100$ MeV and $|\eta| < 2.5$,
- reconstructed by the initial NEWT inside-out (appendix A) or subsequent low-p_T tracking algorithms,
- at least one Pixel b-layer (that correspond to the innermost Pixel layer) hit if expected,
- at least one Pixel hit,
- at least two ($p_T > 100$ MeV), four ($p_T > 200$ MeV) or six ($p_T > 300$ MeV) SCT hits,
- longitudinal transverse and distance of closest approach with respect to the primary vertex of $z_0 \cdot \sin\theta < 1.5$ mm and $d_0 < 1.5$ mm respectively,
- for $p_T > 10$ GeV the probability of the track fit is required to be ≥ 0.01.

The events having at least two "good tracks" are selected. Figure 3.25 shows the mean p_T of the K^0_s candidates reconstructed with p_T (K^0_s) > 500 MeV within a mass window of $\pm$ 20 MeV around the PDG K^0_s mass value as function of the number of charged tracks reconstructed in the event. Black points represent the data, the red point corresponds to the Monte Carlo simulation considering the reconstructed candidates in the same mass window while the

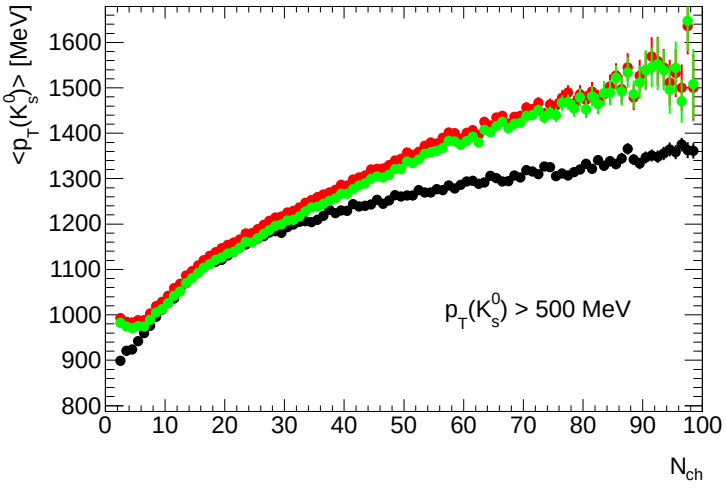

Figure 3.25: Mean p_T of the K^0_s candidates reconstructed within a mass window of $\pm$ 20 MeV around the PDG mass value versus the number of reconstructed charged tracks. Black points are data, red points are MC simulated data while green points represent reconstructed candidates in simulation matched with the Monte Carlo truth.

green points represent reconstructed candidates in simulation matched with the Monte Carlo truth (no background contamination). Both for data and MC simulation, the $<p_T>$ of K^0_s candidates increases with the number of the charged particle in the event. This indicates that in events with higher activity the K^0_s are produced with a higher p_T. From the comparison between the behavior of all reconstructed candidates in the Monte Carlo sample and the ones that are matched to the truth, it appears that the only effect of the background is shifting down the $<p_T>$ versus N_{ch} curve. Comparison with data shows that, for events with high multiplicity, the MC simulation with the tuning MC09 predicts a higher $<p_T>$ mean value than the one observed in the data, with the deviation that becomes higher for higher multiplicity events. Also a discrepancy for events with a low value of the number of charged tracks is observed, where the structure with a minimum at around $N_{ch} = 6$ present in the simulation is not observed in data.

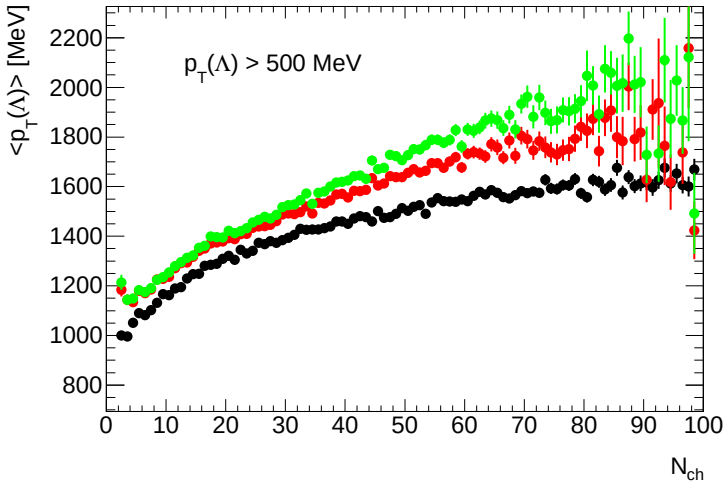

Figure 3.26: Mean p_T of the Λ^0 candidates reconstructed within a mass window of $\pm$ 7 MeV around the PDG mass value versus the number of reconstructed charged tracks. Black points are data, red points are MC simulated data while green points represent reconstructed candidates in simulation matched with the Monte Carlo truth.

Figure 3.26 shows $<p_T>$ versus N_{ch} for Λ^0 candidates reconstructed in data in a mass window within 7 MeV to the PDG mass value (black points) compared with the one for candidates reconstructed in Monte Carlo simulation (red points) and matched with the Monte Carlo truth (green). Like in the K^0_s case, the MC simulation with the tuning MC09 predicts a higher $<p_T>$ of the Λ^0 candidates for events with a high multiplicity than in data and a similar discrepancy is visible in the low N_{ch} region.
Figure 3.27 shows the mean number of K^0_s candidates reconstructed in the invariant mass window $|M_{K^0_s} - M_{PDG}| < 20$ MeV normalized to the number of charged tracks versus the number of reconstructed charged tracks N_{ch}. Black points represent data, red points represent the Monte Carlo simulation and the green points are reconstructed K^0_s in simulation matched with the truth. Even if in the counting of Monte Carlo reconstructed candidates (in the mass window) are entering also fake candidates, there is no effect on the shape

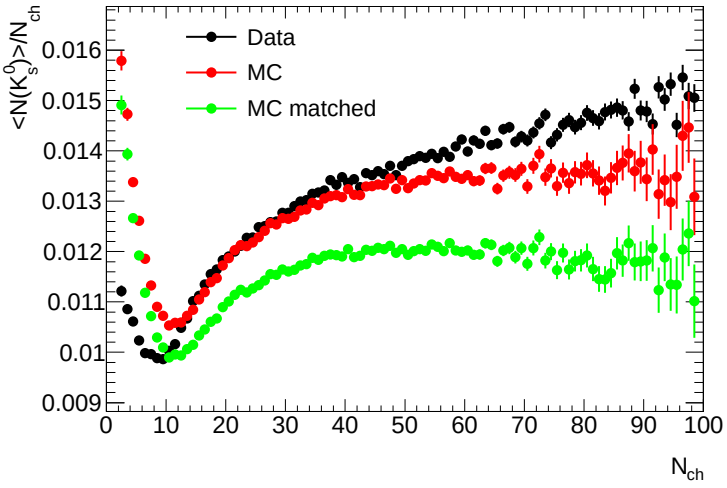

Figure 3.27: Mean number of K^0_s candidates reconstructed within a mass window of $\pm$ 20 MeV around the PDG mass value divided by the number of charged multiplicity versus the event charged multiplicity N_{ch}. Black points are data, red points are MC simulated data while green points represent reconstructed candidates in simulation matched with the Monte Carlo truth.

of the mean number of K^0_s candidates reconstructed divided by the number of charged multiplicity versus the event charged multiplicity N_{ch}. In Monte Carlo simulation, for $N_{ch} > 40$, the mean number of K^0_s increases linearly with the number of the charged particles in the event while in data it increases more than linearly with the multiplicity of the event. Also the minimum that for simulation is at around $N_{ch} = 12$, for data it is shifted to a lower value ($N_{ch} = 8$).

3.7 Summary

A good agreement between data and simulation samples in most of the kinematical distributions has been found, demonstrating an excellent modeling of the detector response in the Monte Carlo simulations. The discrepancy seen at high values in the p_T spectrum can be due to generator modeling, since the dis-

tributions of the proper decay time tend to have a better agreement. This work will be used as a foundation for the production measurements for these decays in the near future. Moreover the correlations between strangeness production and charged multiplicity distributions have been studied; these distributions seems to be sensible to the description of the strangeness production in Monte Carlo generators and can be further used to constrain the simulation (for this scope a full unfolding of both tracks and of the K^0_s (Λ^0 or $\overline{\Lambda^0}$) candidates is required).

Chapter 4

The Baryon number transport

4.1 Introduction

In the Standard Model of particle physics the baryon number B is a conserved quantity in all interactions: baryons and and antibaryons have baryon number $B = 1$ and $B = -1$ respectively. Particle yields together with the ratios of the particle production in hadronic interactions are important indicators of the collision dynamics. In particular, the antibaryon to baryon ratios (or baryon antibaryon asymmetry) can allow to distinguish among different models describing the baryon number transport away from the beam remnant to the mid-rapidity region. Moreover these measurements allow to determine the carrier of the baryon number, in particular if the baryon number is carried by the valence quarks or by the gluon field. A short description of theoretical models (quark-gluon string model, string junction models) is given in the next two sections.

4.1.1 The Quark Gluon String Model (QGSM)

The quark-gluon string model (QGSM) [42] can both describe elastic scattering of hadrons and multiple production of particles in high-energy processes. This model is based on the Gribov-Regge theory of the hadronic and partonic interactions; the subprocesses with quark annihilation and quark exchange is

described as a reggeon exchange in the t-channel while a subprocess with a color exchange can be represented with one or more pomeron exchange in elastic amplitude. The QGSM describes also the string fragmentation, the formation of resonances and the hadronic rescattering (stable hadron or resonances can further interact with other hadrons). In this approach the baryons are considered as a bound quark-diquark state. A baryon number transport implies the breaking of the diquark pair; in this conventional approach the baryon number cannot be transported over large rapidity gaps, even at LHC energies. This brings to a zero net-baryon density at mid-rapidity from the fragmentation region.

4.1.2 String Junction Model

The String Junction Model is another mechanism that can bring to a baryon number transport from the fragmentation region to the midrapidity region. In the junction model, the baryon number is traced using a topological "Y-shape" junction of three gluons, each one connected originally with a valence quark. If one considers an excited baryonic state, there is the possibility for the strings connecting the valence quark to fragment via $q\bar{q}$ generating mesons,

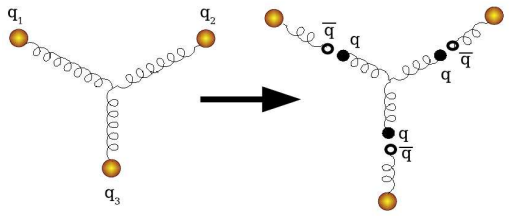

Figure 4.1: Schematic view of a baryon junction. On the left are shown the three valence quark (q_1, q_2, q_3) bounded by a gluon string junction. When the three strings are stretched and broken, as shown on the right, they generates three $q\bar{q}$ pairs, leaving a new baryon and three mesons carrying the original valence quarks.

leaving now three sea quarks around the junction. This process is schematized in figure 4.1. Based on this model two kind of approaches were developed:

- a picture in which the baryon number (B) is carried by the three valence quarks ($B/3$ for each quark) that are connected by a string junction [43]. In this picture the baryon number transport to the mid rapidity region is allowed, but it is exponentially suppressed.
- a picture where the baryon number is carried by the gluonic field (namely associated to the center of the junction)[44]. In this case the baryon number transport probability is constant and higher.

4.2 Experimental results from other experiments

In order to obtain information on the baryon number transport mechanism, the ratio (or the asymmetry[1]) between baryon and anti-baryon has been studied so far. A review on the existing results coming from RHIC and HERA and the latest results from the ALICE and LHCb experiments at LHC will be presented in the next sections.

4.2.1 Results from RHIC

Data from BRAHMS [45] and STAR [46] experiments collected from proton-proton and heavy ion Au-Au collision at RHIC have been used to study the baryon number transport mechanism.
The BRAHMS collaboration has measured the antiproton-proton ratio for proton-proton collision at the center-of-mass energy of $\sqrt{s} = 200$ GeV and compared with Monte Carlo expectations and with the same measurement performed using data from 20% central[2] Au-Au ion collisions [47]. Figure 4.2

[1] defined as $A = \frac{N_B - N_{\bar{B}}}{N_B + N_{\bar{B}}}$

[2] In heavy ion collisions collisions are categorized by their centrality, because the system created in a head-on collisions is different from that in a peripheral collisions. Theoretically,

shows the antiproton to proton ratio versus the transverse momentum at the extreme measured rapidities ∼0 and ∼3. The ratio is flat within the uncertainties and becomes on average smaller at higher rapidity. In figure 4.3 is shown

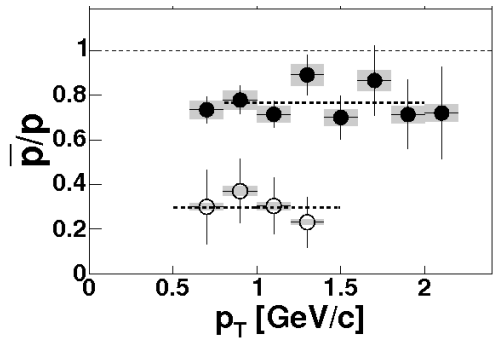

Figure 4.2: Antiproton to proton ratio versus p_T at $y = 0$ (solid circles) and y $\sim$ 3 (open circles). The lines show the result of fitting a constant to the data, over the indicated range. The shaded area shows the estimate of the systematic uncertainty.

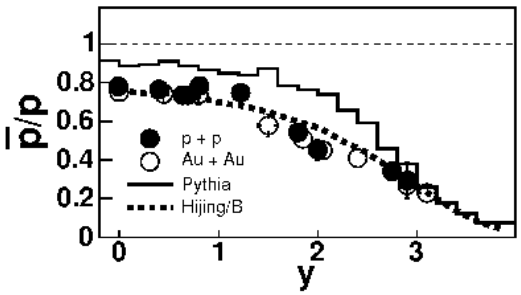

Figure 4.3: Antiproton to proton ratio versus y from p-p collisions at $\sqrt{s} = 200$ GeV (solid points) and Au-Au collisions (open points). Also the predictions from PYTHIA (solid line) and HIJING/B (dashed line) are shown.

the antiproton to proton yields as a function of rapidity. Up to $y \sim 1.5$ the ratio is almost flat while for higher rapidity it starts to decrease. This value sets

the centrality is characterized by the impact parameter **b** which is the distance between the centers of two colliding heavy ions. Lower value of centrality means a head-on collision

a limit between the string breaking dominated regime and the fragmentation region. Moreover the result coming from Au-Au collision data are compatible with the proton-proton one. Data are also compared with two different model predictions. PYTHIA overestimates the ratio and this is related to the fact that it uses only the quark-diquark breaking for the colliding protons without baryon number transport from the beam. HIJING/B [48] shows a better agreement with data: in this MC generator an additional mechanism for an easy transport of baryon number toward midrapidity is added and it is based on the baryon string junction implementation.
A similar analysis in Au-Au collisions at $\sqrt{s_{NN}} = 130$ GeV was performed by the STAR collaboration showing a similar lower antiproton to proton ratio with respect to the hypothesis of no baryon number transport at mid-rapidity from the beam at RHIC energies [49].

4.2.2 Results from HERA

The H1 collaboration [50] has shown evidence of baryon-antibaryon asymmetry for protons and antiprotons with small momentum in the laboratory frame produced in electron-proton interaction at HERA. A preliminary result was presented [51] showing an asymmetry of $\sim 8\%$ at $\Delta y \sim 7$ [3] but it was never published due to the large systematic uncertainties caused by the high beam-gas rate.
In a more recent paper the same collaboration reported the result on the asymmetry in the production Λ^0 with respect to $\overline{\Lambda^0}$. Figure 4.4 shows the asymmetry of the differential production cross section of the Λ^0 and $\overline{\Lambda^0}$ baryons versus the transverse momentum p_T and versus the pseudorapidity η. A Λ^0-$\overline{\Lambda^0}$ asymmetry that deviates from zero would indicate a transfer of the baryon number from the proton beam to the final state strange particles. The measured distributions of the asymmetry A are observed to be compatible with

[3] $\Delta y = y_{beam} - y_{baryon}$ with $y_{beam}(y_{baryon})$ the rapidity of the incoming beam (outcoming baryon). For y=0 (longitudinal momenta $p_z = 0$) the equivalent rapidity interval corresponds to ($\Delta y = \ln \frac{\sqrt{s}}{m_p}$)

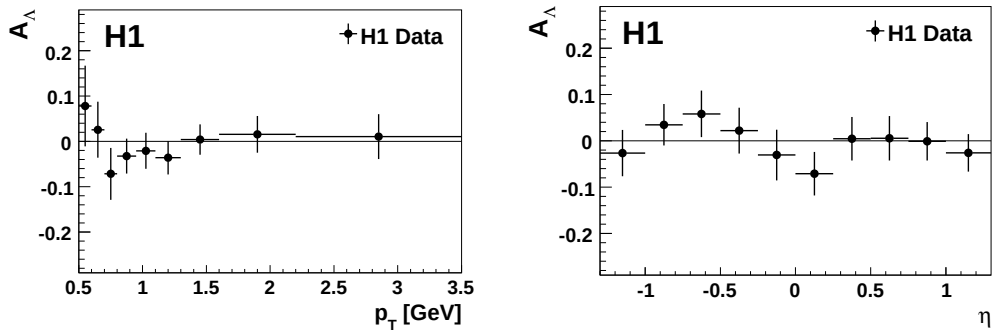

Figure 4.4: The asymmetry A_Λ of the differential production cross sections of the Λ^0 and $\overline{\Lambda^0}$ baryons in the laboratory frame as a function of the transverse momentum p_T (left) and pseudorapidity η (right). The asymmetry is defined as $A_\Lambda = \left[\sigma(ep \to e\Lambda X) - \sigma(ep \to e\bar{\Lambda}X)\right] / \left[\sigma(ep \to e\Lambda X) + \sigma(ep \to e\bar{\Lambda}X)\right]$. The error bars show the statistical uncertainty.

zero within errors so no evidence of baryon number transfer is visible in the measured data from H1.

4.2.3 Results from LHC

Since LHC is the highest energy proton-proton accelerator built so far, data coming from collisions can be used to study the baryon number transport over large rapidity intervals. In particular the ALICE experiment has measured the $\bar{p}/p$ ratio [53] using the $\sqrt{s} = 900$ GeV and the $\sqrt{s} = 7$ TeV LHC collision data ($\Delta y \sim 6.9 - 8.9$). Using the TPC detector immersed in a 0.5 T magnetic field, ALICE performs both the particle identification (with the dE/dx) and the measure of the momentum. The $\bar{p}/p$ measurement is performed in the rapidity range $|y| < 0.5$ and $0.45 < p < 1.05$ GeV in order to have a high proton purity, a uniform geometrical acceptance and a high reconstruction efficiency. The biggest systematical effect comes from the difference in the interaction cross section of protons and antiprotons with the material and the non negligible background of secondary production of protons and antiprotons while most of the systematics related to the acceptance, to the resolution and

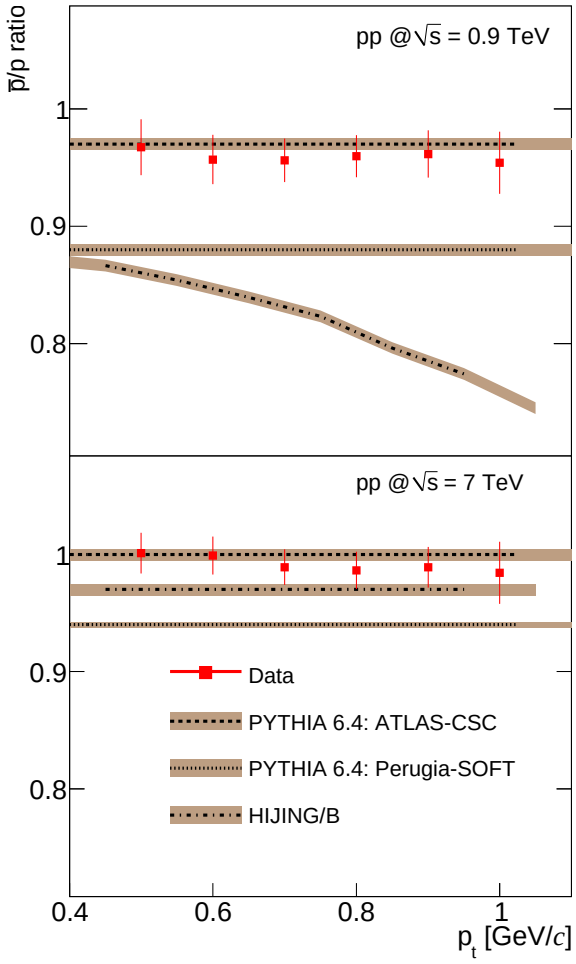

Figure 4.5: The p_T dependence of the $\bar{p}/p$ ratio integrated over $|y| < 0.5$ for pp collisions at $\sqrt{s} = 0.9$ TeV (top) and $\sqrt{s} = 7$ TeV (bottom) measured by ALICE. Only statistical errors are shown for the data; the width of the Monte Carlo bands indicates the statistical uncertainty of the simulation results.

to the reconstruction efficiency are identical for protons and antiprotons and they cancel out in the ratio. The measured $\bar{p}/p$ ratio R integrated in rapidity and p_T is $R_{|y|<0.5} = 0.957 \pm 0.006(stat) \pm 0.014(syst)$ at $\sqrt{s} = 900$ GeV and $R_{|y|<0.5} = 0.991 \pm 0.005(stat) \pm 0.014(syst)$ at $\sqrt{s} = 7$ TeV. This ratio has no dependence on p_T as shown in figure 4.5 or rapidity. Experimental data

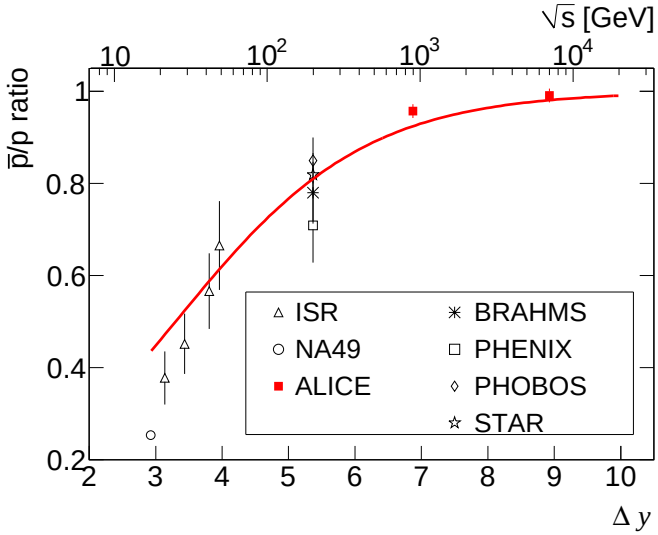

Figure 4.6: Central rapidity $\bar{p}/p$ ratio as a function of the rapidity interval Δy (lower axis) and center-of-mass energy (upper axis). Error bars correspond to the quadratic sum of statistical and systematic uncertainties for the RHIC and LHC measurements and to statistical errors otherwise.

are compared to different Monte Carlo predictions. In particular in figure 4.5 the result is compared with two different PYTHIA tunes, ATLAS-CSC and Perugia-0 (that include an enhanced baryon transfer) and the HIJING/B, which includes a particular gluonic string junction model to enhance the baryon number transport. At $\sqrt{s} = 7$ TeV both PYTHIA tunes agree with data while the HIJING/B underestimates the ratio; in $\sqrt{s} = 900$ GeV data both Perugia-0 tune and HIJING/B underestimate the ratio while PYTHIA ATLAS-CSC agrees well also at this lower energy. Figure 4.6 shows the $\bar{p}/p$ measurement in proton-proton collisions done at different experiments (ISR, SPS) versus the center of mass energy and the rapidity interval (Δy). The curve comes from the parametrization of the ratio R versus the rapidity interval given by the

Regge model[4] that predicts

$$\frac{1}{R} = 1 + C \cdot e^{[(\alpha_J - \alpha_P)\Delta y]} \tag{4.2.1}$$

The experimental data are fitted using α_P =1.2 [54] as the value of pomeron intercept and $\alpha_J = 0.5$ [55] for the string junction intercept. The only free parameter is C, representing the relative contribution of the two diagrams. The LHCb experiment at LHC have also performed a preliminary measurement both of the $\bar{p}/p$ ratio and of the $\overline{\Lambda^0}/\Lambda^0$ ratio using data collected at $\sqrt{s} = 900$ GeV and $\sqrt{s} = 7$ TeV. The results have been compared to the Monte Carlo expectations [56, 57]. LHCb is a forward spectrometer with a pseudorapidity acceptance of approximately 2< η <5. Figure 4.7 shows the $\overline{\Lambda^0}/\Lambda^0$ ratio at $\sqrt{s} = 900$ GeV (left) and at $\sqrt{s} = 7$ TeV versus the rapidity compared with LHCb Monte Carlo and PYTHIA6 with the Perugia0 tune. While the result at $\sqrt{s} = 7$ TeV is in agreement with Monte Carlo predictions, the $\overline{\Lambda^0}/\Lambda^0$ ratio at $\sqrt{s} = 900$ GeV is lower than in MC expectations. Moreover the same results can be also shown as a function of $\Delta y = y$(beam)-$y(\Lambda)$, allowing a

[4]The baryon pair production is governed by the pomeron exchange and the baryon transport by the string-junction exchange

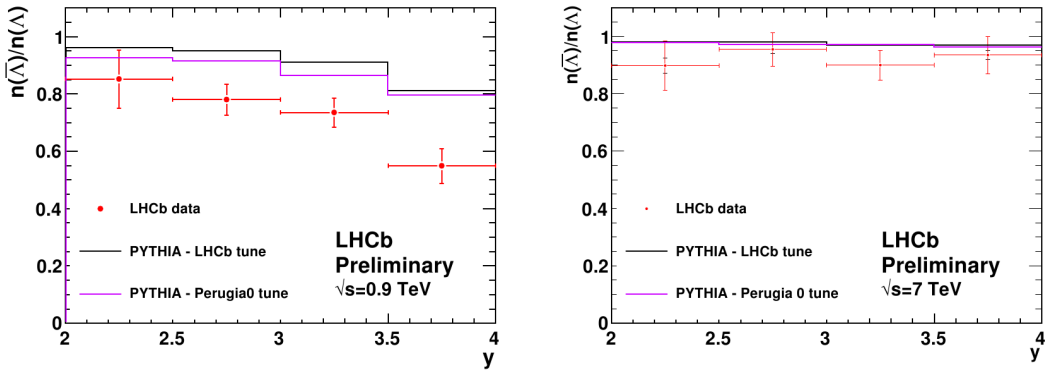

Figure 4.7: LHCb results on the $\overline{\Lambda^0}/\Lambda^0$ ratio at $\sqrt{s}$=0.9 TeV (left) and $\sqrt{s}$=7 TeV (right). Data are compared to the LHCb Monte Carlo with standard settings and the PYTHIA6 MC generator with the Perugia0 tune.

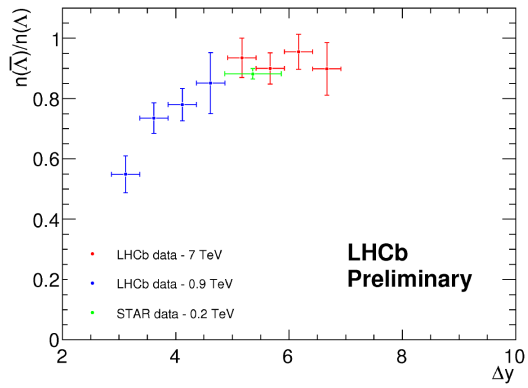

Figure 4.8: The LHCb $\overline{\Lambda^0}/\Lambda^0$ ratio versus Δy compared to a single data point measured from the STAR collaboration [58].

direct comparison between results at different energies. Figure 4.8 shows the comparison between the LHCb and the STAR measurement measurement [58] done for proton-proton collisions at $\sqrt{s}$=200 GeV. A good agreement can be seen between the two measurements.

Chapter 5

$\overline{\Lambda^0}/\Lambda^0$ ratio measurement

5.1 Introduction to the measurement

The production ratio between $\overline{\Lambda^0}$ and Λ^0 baryons is related to the transfer of the baryon number from the beam remnant to the central rapidity range of the measured acceptance, as already explained in chapter 4. Deviation from the unity of this ratio indicate a transfer of baryon number from the beam to the central region. Previous p-pbar colliders like Tevatron or the Sp$\bar{\text{p}}$S had a symmetric configuration (net baryon number zero) and it is difficult to study this effect with their data (especially versus p_T).
Due to the insufficient experimental results, the different models that have been developed strongly disagree from each others; thus an experimental input is required in order to distinguish between them.
Figure 5.1 shows the $\overline{\Lambda^0}$-to-Λ^0 ratio at the center of mass energy proton proton collision of $\sqrt{s} = 900$ GeV and $\sqrt{s} = 7$ TeV calculated at generator level for different tunes of the PYTHIA Monte Carlo Generators [64].

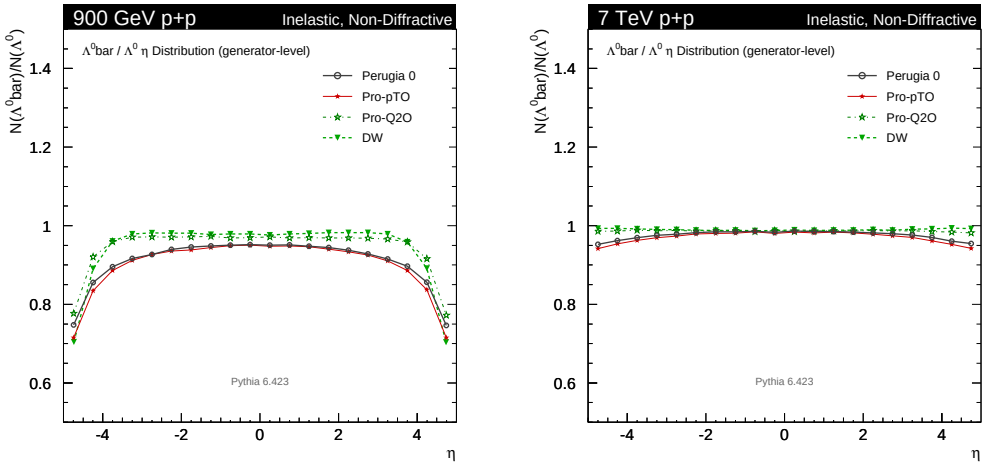

Figure 5.1: Generated $\overline{\Lambda^0}$-to-Λ^0 ratio as a function of pseudorapidity at the energy of $\sqrt{s} = 900$ GeV (left) and $\sqrt{s} = 7$ TeV (right) for different PYTHIA tunings.

5.2 Dataset and event selection

The dataset used to perform this analysis in ATLAS is the same as for the K^0_s and Λ^0 reconstruction but some luminosity blocks are further excluded in order to avoid the period during the run where there were van der Meer orbit scans [65](also called beam-separation or luminosity scans). This is needed because of the large variation of the beam spot position in these luminosity blocks. The list of runs and luminosity blocks used is reported in table 5.1 The event selection used for this measurement is identical to the one used for the analysis of charged-particle multiplicities in proton-proton interactions at $\sqrt{s} = 7$ TeV. Data were selected using the Level 1 (L1) single-arm minimum bias trigger scintillator (MBTS) trigger denoted as L1_MBTS_1. Luminosity blocks were selected with the criteria previously described. Tracks were reconstructed down to a transverse momenta of 50 MeV. These events were required to have at least one reconstructed primary vertex including two or more tracks and the beam spot position. The primary vertex preselection uses tracks with:

Run Number	lbn range
152166	206-300
152214	159-202
152221	5-167
152345	128-207
152409	124-209
	286-716
152441	309-370
	372-405
	411-670
152508	196-204
152508	241-261

Table 5.1: List of runs, corresponding range of good luminosity blocks used.

- $p_T > 100$ MeV,
- transverse distance of closest approach with respect to the beam spot of $|d_0^{BS}| < 4$ mm,
- transverse and longitudinal errors of $\sigma(d_0^{BS}) < 5$ mm and $\sigma(z_0^{BS}) < 10$ mm respectively,
- at least one Pixel and four SCT hits,
- at least six Pixel and SCT hits in total.

The primary vertices reconstructed are ordered according to the sum of the p_T of the tracks used in the vertex fit. The vertex with the highest p_T sum is selected in case of multiple primary vertices. Also pileup removal has been applied. Events are further selected requiring at least 2 tracks that satisfy the following requirements:

- $p_T > 100$ MeV and $|\eta| < 2.5$,
- at least one Pixel b-layer (that correspond to the innermost Pixel layer) hit if expected by the extrapolated track,
- at least one Pixel hit,

- at least two ($p_T > 100$ MeV), four ($p_T > 200$ MeV) or six ($p_T > 300$ MeV) SCT hits,
- longitudinal transverse and distance of closest approach with respect to the primary vertex of $z_0 \cdot \sin\theta < 1.5$ mm and $d_0 < 1.5$ mm respectively,
- for $p_T > 10$ GeV the probability of the fit is required to be ≥ 0.01.

The total number of events selected using these cuts is ∼10 million. Identical requirements were applied to the MC sample consisting of 20 million events generated using PYTHIA 6.4.21 generator with the default ATLAS MC09 PYTHIA tune [59] and simulated with GEANT4 in which the longitudinal position of the primary vertex has been reweighed in the simulation in order to be consistent with the data (more details already given in chapter 3). This can be done because the generated size of the primary vertex distribution is wider than the real one.

5.2.1 Λ^0 and $\overline{\Lambda^0}$ selection

Charged tracks with opposite charge and $p_T > 100$ MeV with at least two silicon hits and fitted to a common vertex are used to reconstruct Λ^0 and $\overline{\Lambda^0}$ candidates. Moreover, these candidates have to satisfy the following criteria:

- the chi-square of the vertex fit (with one degree of freedom) $\chi^2 < 15$;
- $\cos(\theta_{pointing}) > 0.9998$ for the point angle $\theta_{pointing}$ between the momentum vector and the flight direction;
- the transverse flight distance of the candidate bigger than 17 mm.

As described in the previous chapter, the track with the highest p_T of the two associated to a Λ^0 or a $\overline{\Lambda^0}$ candidate is assumed to be a proton or an antiproton depending on its charge. This assumption has been verified in the MC sample

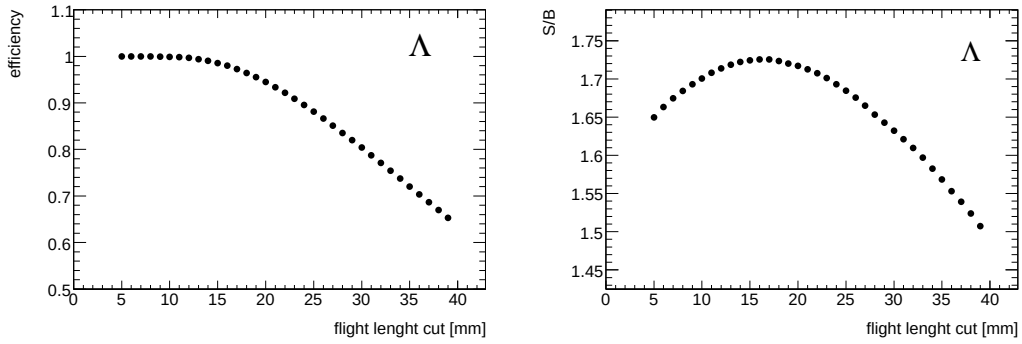

Figure 5.2: Signal reconstruction efficiency (left) and signal to background ratio (right) for Λ^0 candidates reconstructed in MC sample as a function of the cut on the transverse flight distance with all the other selection criteria applied. Only candidates with a reconstructed invariant mass within 7 MeV of the PDG value are considered.

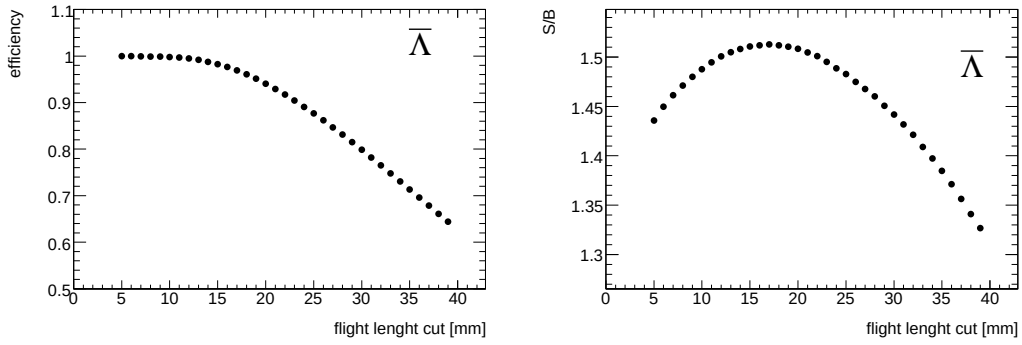

Figure 5.3: Signal reconstruction efficiency (left) and signal to background ratio (right) for $\overline{\Lambda^0}$ candidates reconstructed in MC sample as a function of the cut on the transverse flight distance with all the other selection criteria applied. Only candidates with a reconstructed invariant mass within 7 MeV of the PDG value are considered.

and it is incorrect for a negligible fraction of decays ($\sim 0.2\%$). Please note that the flight distance cut was changed with respect to the one described in chapter 3 used to reconstruct the kinematic distributions of Λ^0 and $\overline{\Lambda^0}$ candidates. The

smaller optimized value for this cut is essential to increase the statistics of Λ^0 and $\overline{\Lambda^0}$ that decay before the first pixel layer: having enough statistic in this region allows to perform a crosscheck of the $\overline{\Lambda^0}/\Lambda^0$ ratio measurement since in this region the contribution of the interacting and secondary production of Λ^0 and $\overline{\Lambda^0}$ is minimal. For the optimization of this cut the MC sample has been used, considering the ratio between the number of signal candidates S over the number of background candidates B in the mass window $|M_{\Lambda^0} - M_{PDG}| < 7$ MeV and $|M_{\overline{\Lambda^0}} - M_{PDG}| < 7$ MeV respectively for Λ^0 and $\overline{\Lambda^0}$. The signal to background ratio and the efficiency for different values of the transverse flight distance cuts are shown in figure 5.2 for Λ^0 candidates and in figure 5.3 for $\overline{\Lambda^0}$ candidates. The S/B distribution has its maximum at 17 mm for both Λ^0 and $\overline{\Lambda^0}$ candidates and the relative signal selection efficiency with this cut is still very high ($\sim 98\%$ with respect to the condition of no cut applied).

5.3 Monte Carlo studies at generator level

With the MC sample it is possible to study and measure the $\overline{\Lambda^0}$-to-Λ^0 ratio at the generator level versus the pseudorapidity, the rapidity[1] and the transverse momentum. The MC sample is also needed in order to find the reconstruction efficiency of Λ^0 and $\overline{\Lambda^0}$ candidates in Monte Carlo simulation. Λ^0 and $\overline{\Lambda^0}$ particles are generated with PYTHIA MC and can be identified using the MC particle numbering convention (PDGID) [66]. These particles are unstable and have a proper decay length of $c\tau \simeq 7.9$ cm. Only primary Λ^0 and $\overline{\Lambda^0}$ decaying in $\Lambda^0 \to p^+\pi^-$ and $\overline{\Lambda^0} \to p^-\pi^+$ are considered. In the selection are cut off all the secondary Λ^0 and $\overline{\Lambda^0}$ particles that are not produced from the hadronization but come from hadronic interaction of other primary particles

[1]It is defined as rapidity with respect to the beam axis $y = \frac{1}{2}\ln\frac{E+p_z c}{E-p_z c}$ where p_z is the component of the particle momentum along the beam axis

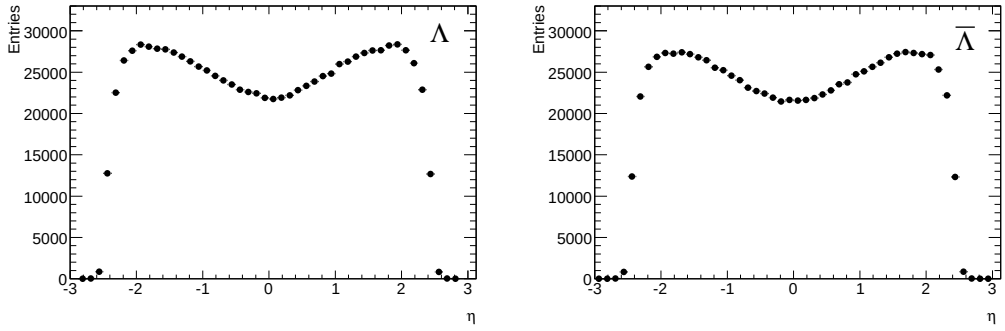

Figure 5.4: PYTHIA Monte Carlo generated pseudorapidity distribution for $\Lambda^0 \to p^+\pi^-$ (left) and $\overline{\Lambda^0} \to p^-\pi^+$ (right). Protons (antiprotons) and pions are required to have $p_T > 100$ MeV and $|\eta| < 2.5$

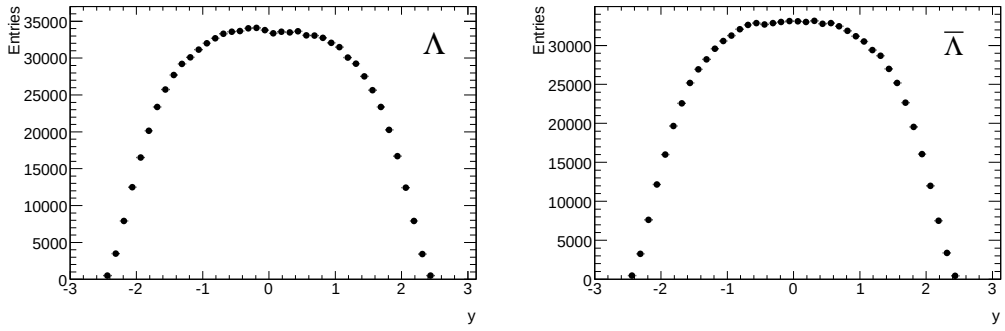

Figure 5.5: PYTHIA Monte Carlo generated rapidity distribution for $\Lambda^0 \to p^+\pi^-$ (left) and $\overline{\Lambda^0} \to p^-\pi^+$ (right). Protons (antiprotons) and pions are required to have $p_T > 100$ MeV and $|\eta| < 2.5$

with the ATLAS detector elements. In order to have a consistent phase-space between the generated and the reconstructed Λ^0 and $\overline{\Lambda^0}$ particles, an additional cut has been imposed to the decay products of these particles: in particular for both p^+ and π^- originating from a Λ^0 decay and for both p^- and π^+ originating from a $\overline{\Lambda^0}$ decay, p_T $(p^{\pm}, \pi^{\mp}) > 100$ MeV and $|\eta(p^{\pm}, \pi^{\mp})| < 2.5$ are requested. Figure 5.4 shows the generated pseudorapidity distribution for Λ^0 (left) and $\overline{\Lambda^0}$ (right) particles with the phase-space cuts imposed to the daughters. The

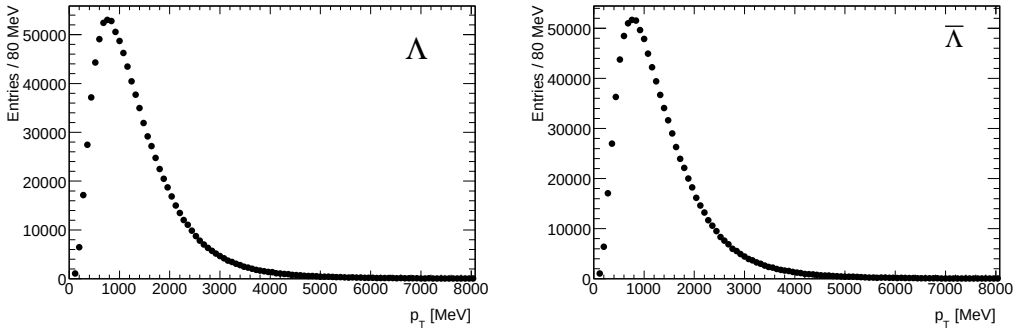

Figure 5.6: PYTHIA Monte Carlo generated transverse momentum distribution for $\Lambda^0 \to p^+\pi^-$ (left) and $\overline{\Lambda^0} \to p^-\pi^+$ (right). Protons (antiprotons) and pions are requested to have $p_T > 100$ MeV and $|\eta| < 2.5$

same cuts for the daughter particles are applied when producing the generated rapidity distributions (figure 5.5) and p_T distributions (figure 5.6) for both Λ^0 and $\overline{\Lambda^0}$. Using the Λ^0 and $\overline{\Lambda^0}$ generated distributions of the transverse momentum, pseudorapidity and rapidity obtained from the Monte Carlo, it is possible to construct the $\overline{\Lambda^0}$-to-Λ^0 ratio produced at generator level. Figure 5.7 shows the ratio versus the pseudorapidity of the Λ^0 and $\overline{\Lambda^0}$ candidates. This distribution is almost flat in the rapidity range $|\eta| < 2.5$ covered by the ATLAS detector and its integrated mean value is 97.6±0.1%. In the same way the figure 5.8 shows the ratio versus the transverse momenta (left) and the rapidity (right).

5.4 Reconstruction Efficiencies for Λ^0 and $\overline{\Lambda^0}$ candidates

The evaluation of the reconstruction efficiency calculated in bins of p_T, η and y is required to correct the measured distributions and obtain the $\overline{\Lambda^0}$-to-Λ^0 ratio corrected for the detector effect. The reconstruction efficiency of $\overline{\Lambda^0}$ and Λ^0 baryons is calculated by the ratio between the reconstructed and generated

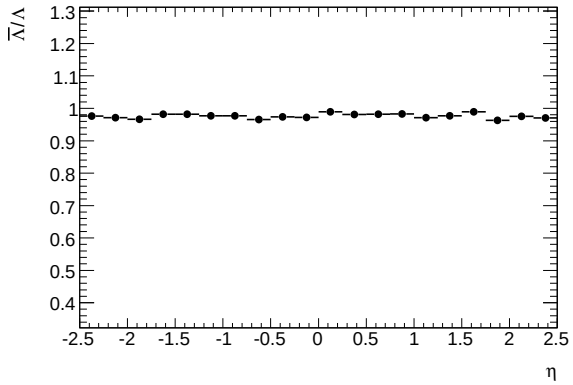

Figure 5.7: $\overline{\Lambda^0}$-to-Λ^0 ratio as a function of pseudorapidity generated in Monte Carlo simulation

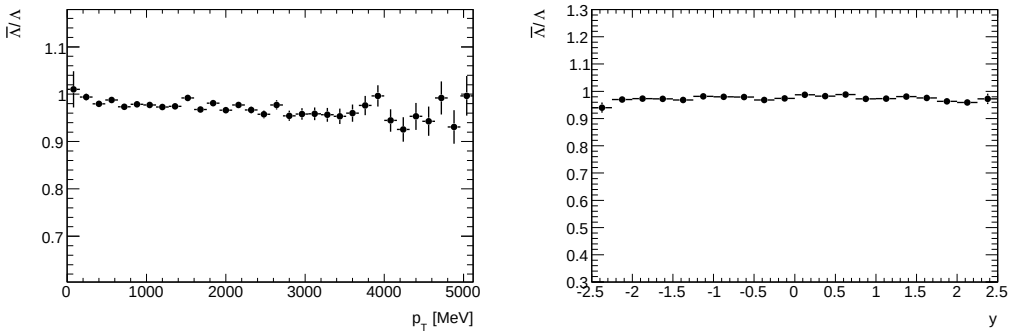

Figure 5.8: $\overline{\Lambda^0}$-to-Λ^0 ratio as a function of transverse momentum (left) and rapidity (right) generated with the Monte Carlo simulation.

Λ^0 and $\overline{\Lambda^0}$ respectively in a given p_T, η or y bin.

$$\varepsilon_{\Lambda^0}(p_T) = \frac{N_{\Lambda^0 reco}(p_T)}{N_{\Lambda^0 gen}(p_T)} \qquad \varepsilon_{\Lambda^0}(\eta) = \frac{N_{\Lambda^0 reco}(\eta)}{N_{\Lambda^0 gen}(\eta)} \qquad \varepsilon_{\Lambda^0}(y) = \frac{N_{\Lambda^0 reco}(y)}{N_{\Lambda^0 gen}(y)} \tag{5.4.1}$$

$$\varepsilon_{\overline{\Lambda^0}}(p_T) = \frac{N_{\overline{\Lambda^0} reco}(p_T)}{N_{\overline{\Lambda^0} gen}(p_T)} \qquad \varepsilon_{\overline{\Lambda^0}}(\eta) = \frac{N_{\overline{\Lambda^0} reco}(\eta)}{N_{\overline{\Lambda^0} gen}(\eta)} \qquad \varepsilon_{\overline{\Lambda^0}}(y) = \frac{N_{\overline{\Lambda^0} reco}(y)}{N_{\overline{\Lambda^0} gen}(y)} \tag{5.4.2}$$

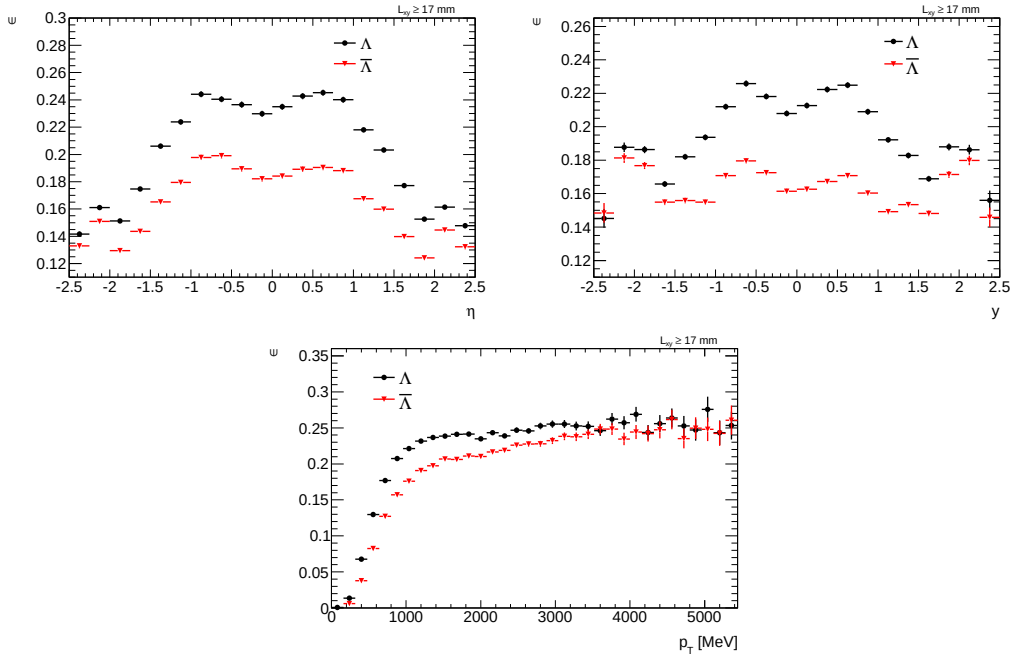

Figure 5.9: The truth-matched efficiency in MC for reconstructing Λ^0 and $\overline{\Lambda^0}$ candidates in data versus η (top-left), y (top-right) and p_T (bottom). The errors are statistical only.

In the numerators of this equations are considered only the reconstructed Λ^0 and $\overline{\Lambda^0}$ candidates for which both the reconstructed daughter tracks are matched to a true proton (antiproton) and to a pion produced in the decay of a primary [2] Λ^0 and $\overline{\Lambda^0}$, respectively. The differences between the Λ^0 and $\overline{\Lambda^0}$ tracking reconstruction efficiency mainly come from the difference in tracking reconstruction efficiency between protons (for Λ^0) and antiprotons (for $\overline{\Lambda^0}$). This efficiency is computed only for those events that pass the minimum bias event selection described in section 5.2. Figure 5.9 shows the efficiencies for Λ^0 (black points) and $\overline{\Lambda^0}$ (red points) as a function of pseudorapidity, rapidity and transverse momenta. As expected, given the higher hadronic interaction

[2] That do not come from the interaction of other particles with the material. This corresponds to generated Λ^0 and $\overline{\Lambda^0}$ with a MC barcode less then 200000

cross section of the antiprotons with respect to the protons with the material, the reconstruction efficiency for Λ^0 is higher compared to the $\overline{\Lambda^0}$ and this difference mainly comes from the low-p_T region (since here the difference between the hadronic interaction cross section for protons and antiprotons is higher).

5.5 Background subtraction procedure

5.5.1 The fit function

The estimation of the number of candidates in a given p_T, η or rapidity bin has been performed fitting the invariant mass spectrum of the Λ^0 and $\overline{\Lambda^0}$ reconstructed in a specific bin. In order to do that, the RooFit [67] ROOT libraries have been used, which provide a toolkit for modeling the expected distribution of events in a physics analysis. The fit function used is the following:

$$\exp\left(-0.5 \cdot x^{1+\frac{1}{1+0.5\cdot x}}\right) + p0 + p1 \cdot M + p2 \cdot M^2$$
$$x = \left|\frac{M-\mu}{\sigma}\right| \tag{5.5.1}$$

It corresponds to the sum of a modified Gaussian for the signal and a second order polynomial function (for the background). The modified Gaussian is a Gaussian distribution with exponential tails. This function has been used since it ensures a better stability and performance in fitting the mass shape in different bins of the kinematics variables.
Figure 5.10 shows the invariant mass distribution of Λ^0 (top) and $\overline{\Lambda^0}$ (bottom) candidates reconstructed in the Monte Carlo simulation in the pseudorapidity slice corresponding to the range $-0.75 < \eta < -0.5$ fitted using the function defined in 5.5.1. As expected, the number of reconstructed $\overline{\Lambda^0}$ is lower then the number of reconstructed Λ^0. The χ^2/dof of the fit in the two cases is $\chi^2/dof = 1.081$ for Λ^0 and $\chi^2/dof = 1.216$ for $\overline{\Lambda^0}$. In the Λ^0 case, the number of signal candidates extracted with the fitting procedure is 13025 ± 162

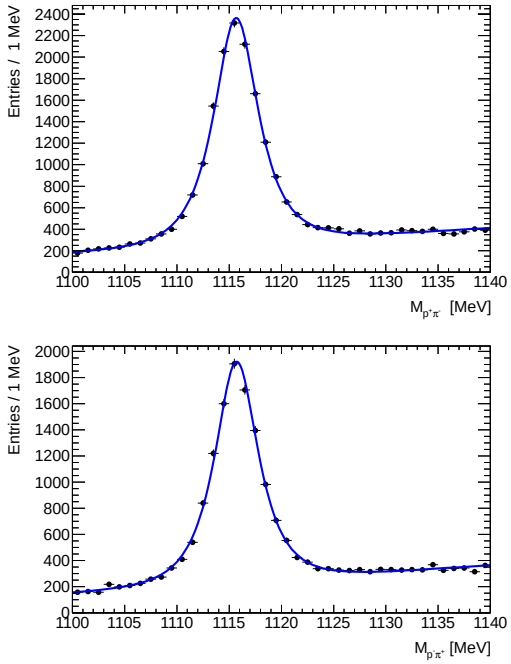

Figure 5.10: Invariant mass distribution of Λ^0 (top) and $\overline{\Lambda^0}$ (bottom) candidates reconstructed in Monte Carlo simulation in the pseudorapidity range $-0.75 < \eta < -0.5$ fitted using the function defined in 5.5.1. The number of candidates extracted from the fit are 13025 ± 162 for Λ^0 and 10264 ± 145 for $\overline{\Lambda^0}$.

while, in the $\overline{\Lambda^0}$ case, the number of signal candidates extracted from the fit is 10264 ± 145.

5.5.2 Background subtraction in MC simulation

Figure 5.11 shows the 2D-histogram of the transverse momenta of reconstructed Λ^0 candidates in the simulation versus their invariant mass with also the projection of p_T slices showing the mass distribution for two particular p_T bins; similarly figure 5.12 show the 2D-histogram for η and y versus the invariant mass of Λ^0 candidates and figure 5.13 the projection of two of η and y slices. It is clear from the different slices shown in these figures that the

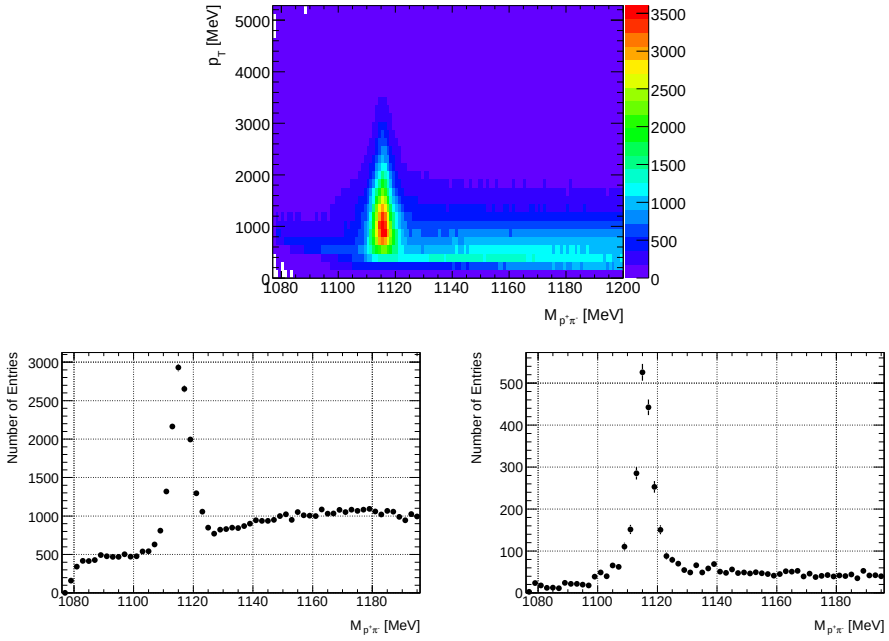

Figure 5.11: (up) 2D histogram of the transverse momentum versus the invariant mass of the Λ^0 candidates reconstructed in simulation (down). The invariant mass distribution for the reconstructed Λ^0 candidates with 1.44 $<p_T$ $<$ 1.6 GeV (left) and 2.8 $<p_T <$ 2.96 (right).

shape of the signal and background can change heavily in different kinematic and detector regions (high-p_T low-p_T or barrel-endcap). Thus the fit function distribution of the signal has to be stable enough and the correlation between the various parameters have to be relatively small in order to accommodate with the same pdf the different mass shapes that can appear when fitting some particular slices. The same function is used to fit both Λ^0 and $\overline{\Lambda^0}$ candidates invariant mass distributions.

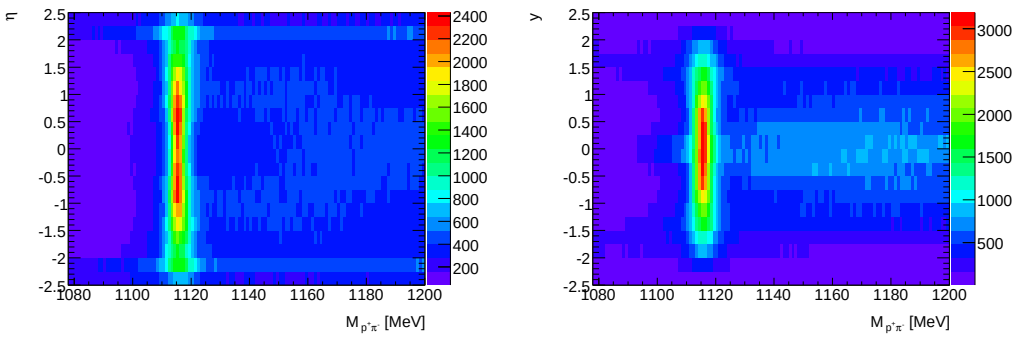

Figure 5.12: 2D histograms of the pseudorapidity (left) and rapidity (right) versus the invariant mass of the Λ^0 candidates reconstructed in simulation.

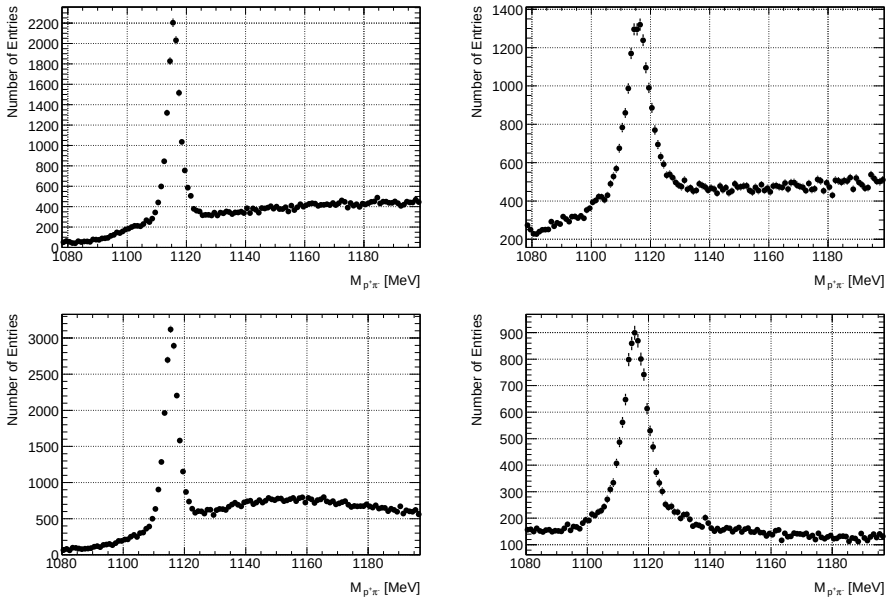

Figure 5.13: (up) The invariant mass distribution for the reconstructed Λ^0 candidates with $0 < \eta < 0.25$ (left) and $1.5 < \eta < 1.75$ (right). (down) The invariant mass distribution for the reconstructed Λ^0 candidates with $0.25 < y < 0.5$ (left) and $1.75 < y < 2.0$ (right).

5.5.3 Background subtraction in Data

The same background subtraction procedure used for the Monte Carlo sample has been applied also to the data. Figures 5.14 and 5.15 show the p_T background-subtracted distributions in both linear and logarithmic scale for the reconstructed Λ^0 and $\overline{\Lambda^0}$ candidates in data. The maximum of these distribution for both Λ^0 and $\overline{\Lambda^0}$ is at ~ 1050 MeV. In Figure 5.16 and figure 5.17 are shown the pseudorapidity and the rapidity data distributions for Λ^0 and $\overline{\Lambda^0}$ respectively.

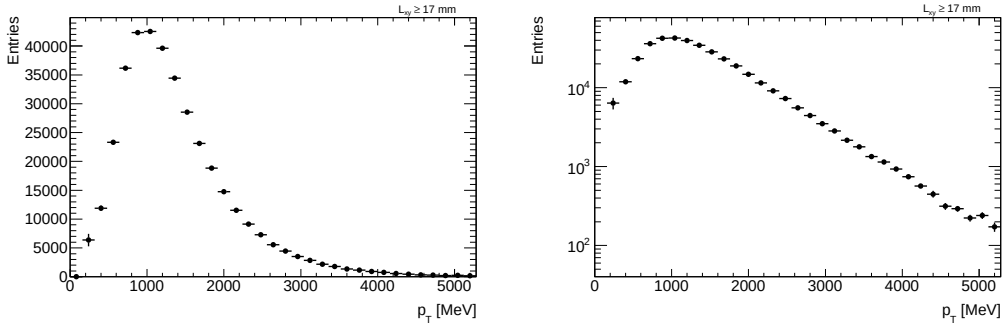

Figure 5.14: Transverse momentum distribution of Λ^0 candidates reconstructed in data after background subtraction in linear (left) and logarithmic (right) scale.

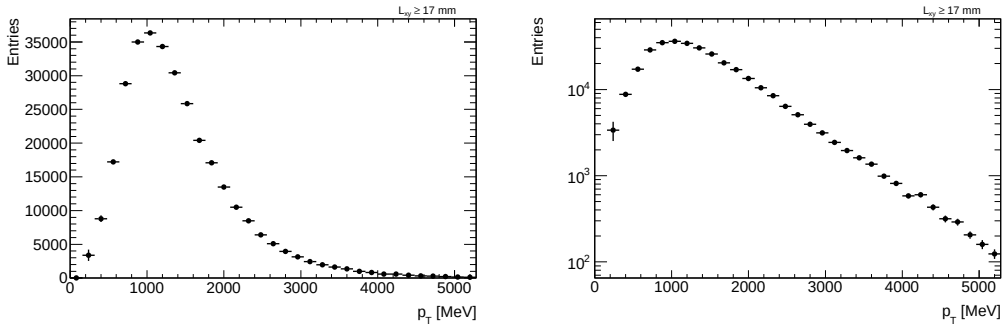

Figure 5.15: Transverse momentum distribution of $\overline{\Lambda^0}$ candidates reconstructed in data after background subtraction in linear (left) and logarithmic (right) scale.

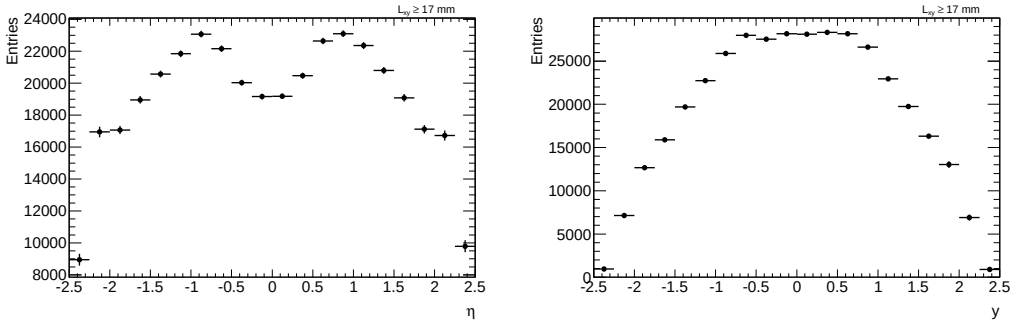

Figure 5.16: Pseudorapidity (left) and rapidity (right) distributions of Λ^0 candidates reconstructed in data after background subtraction.

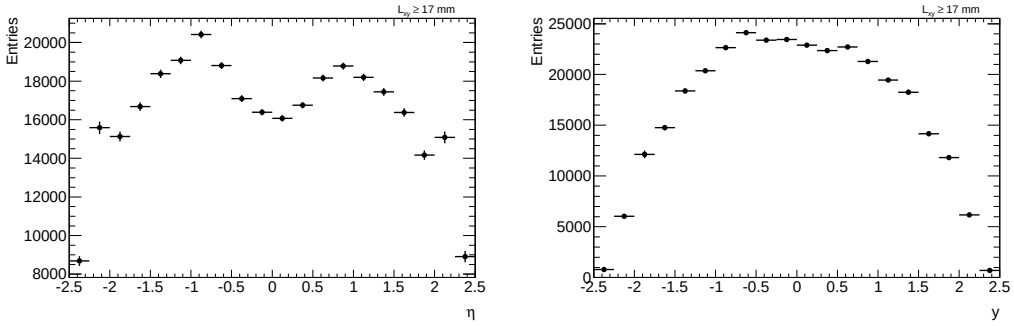

Figure 5.17: Pseudorapidity (left) and rapidity (right) distributions of Λ^0 candidates reconstructed in data after background subtraction.

5.6 Uncorrected and efficiency corrected $\overline{\Lambda^0}/\Lambda^0$ ratio

In the production ratio most of the systematic effects related to the tracking cancels out, but the expected ratio can be changed by different other effects:

- the difference in the reconstruction efficiency for Λ^0 and $\overline{\Lambda^0}$;
- the different in the contamination due to secondary production of Λ^0 and $\overline{\Lambda^0}$ originating from the interaction of other particles with the material of the ATLAS Inner Detector;

- the difference in the interaction cross section of Λ^0 and $\overline{\Lambda^0}$ with the material.

The $\overline{\Lambda^0}/\Lambda^0$ ratio has been corrected for the difference in the reconstruction efficiencies between Λ^0 and $\overline{\Lambda^0}$ while the other effects have been treated as systematic uncertainties (described in section 5.8) for the $\overline{\Lambda^0}/\Lambda^0$ ratio measurement.
The pseudorapidity, rapidity and transverse momentum distributions (background-subtracted) for both Λ^0 and $\overline{\Lambda^0}$ are used to produce the uncorrected $\overline{\Lambda^0}/\Lambda^0$ ratio plots versus each one of the three kinematic variables. These are shown in figure 5.18 with the error bars that represent the statistical error.
In order to obtain the production ratio versus η, y and p_T corrected, each single kinematic background subtracted distribution for Λ^0 and $\overline{\Lambda^0}$ is bin-by-bin cor-

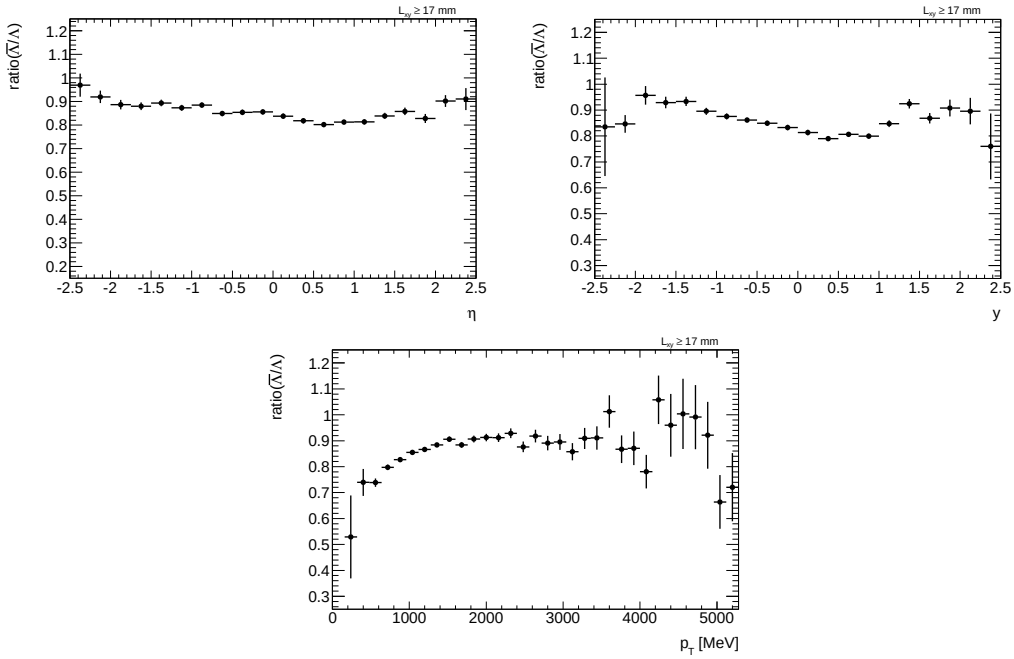

Figure 5.18: Ratio between $\overline{\Lambda^0}$ and Λ^0 candidates reconstructed in data after the background subtraction procedure versus η (top left), y (top right) and p_T (bottom). The error bar represent the statistical error.

rected for the reconstruction efficiency calculated in section 5.4. This is done in order to take into account the difference in reconstruction efficiency between Λ^0 and $\overline{\Lambda^0}$ that mainly comes from the difference in reconstruction efficiencies between protons (for Λ^0) and antiprotons (for $\overline{\Lambda^0}$). The corrected kinematic distributions of $\overline{\Lambda^0}$ and Λ^0 are then divided bin-by-bin in order to obtain the corrected $\overline{\Lambda^0}/\Lambda^0$ ratio and the result is shown in figure 5.19. Since the $\overline{\Lambda^0}$-to-Λ^0 ratio is almost certainly bound to be less than unity it appears that the correction for the $\overline{\Lambda^0}$ (where a lack of knowledge is expected) is overestimated in most of the bins. In particular it is known that the GEANT4 nuclear interaction cross section is overestimated for antiprotons (section 5.8.1), corresponding to a ratio larger than unity in most of the p_T, η and y bins.

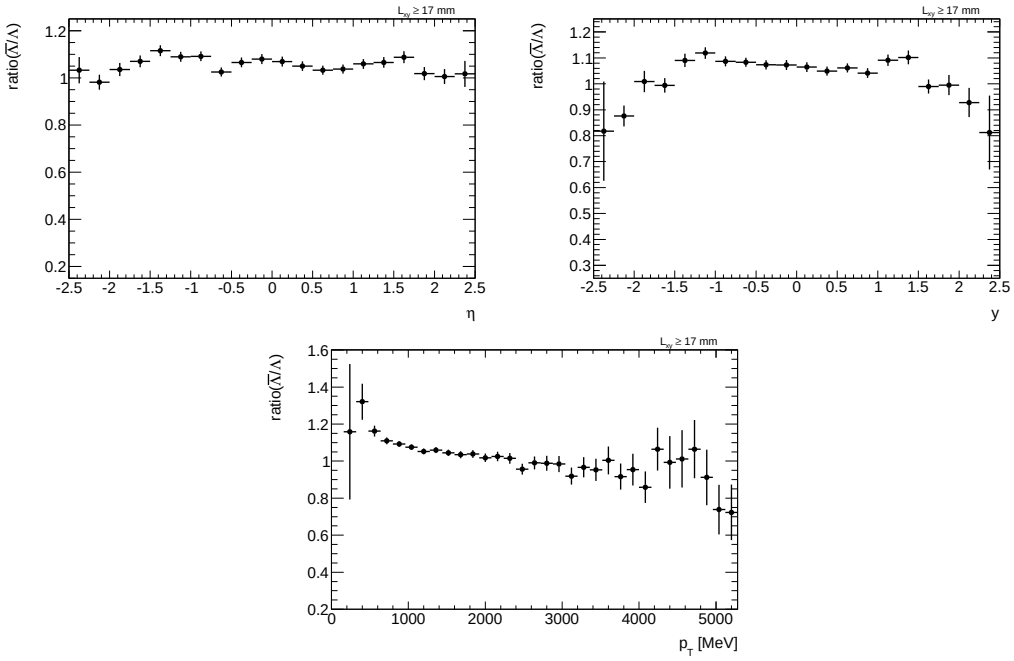

Figure 5.19: Ratio between $\overline{\Lambda^0}$ and Λ^0 candidates reconstructed in data corrected for detector effects using MC efficiencies versus η (top left), y (top right) and p_T (bottom). The error bar represent the statistical error

5.7 Closure test for the $\overline{\Lambda^0}/\Lambda^0$ ratio

In order to test the validity of the efficiency correction procedure used, a closure test has been performed on the Monte Carlo simulation. The η, y and p_T background-subtracted distributions of Λ^0 and $\overline{\Lambda^0}$ candidates reconstructed after simulation, are corrected for the efficiencies calculated in section 5.4. The $\overline{\Lambda^0}$-to-Λ^0 ratio versus the three kinematic variables taken into account is then calculated for the candidates reconstructed in MC and efficiency corrected and the result is then compared with the Monte Carlo truth predictions. Figure 5.20 shows the closure test for the truth and reconstructed $\overline{\Lambda^0}/\Lambda^0$ ratio versus

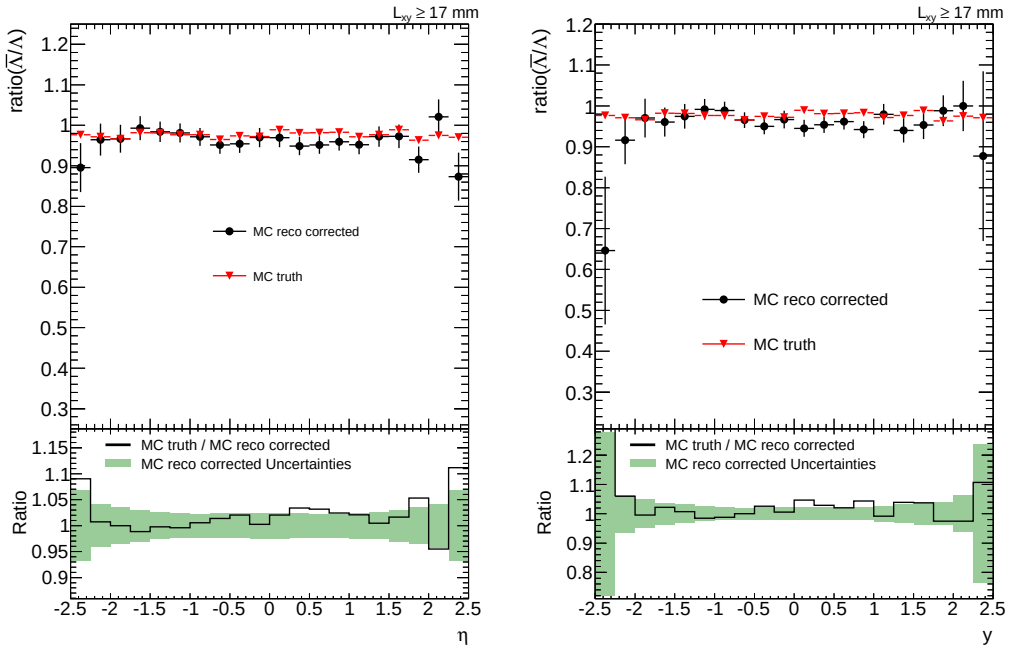

Figure 5.20: Closure test for the $\overline{\Lambda^0}$-to-Λ^0 ratio as a function pseudorapidity (left) and rapidity (right). The red and black points corresponds to the $\overline{\Lambda^0}/\Lambda^0$ ratio in the truth and for the candidates reconstructed in MC and efficiency corrected respectively. The errors are statistical only. The ratio between the truth and the corrected $\overline{\Lambda^0}/\Lambda^0$ is shown in the bottom, where the green band represents the statistical error of the reconstructed and corrected $\overline{\Lambda^0}/\Lambda^0$ ratio.

the pseudorapidity and the rapidity while figure 5.21 shows the closure test of the ratio versus p_T. The truth and the reconstructed $\overline{\Lambda^0}/\Lambda^0$ ratio agree and no evidence of non closure is present at this level of sensitivity. The non closure could be present because the reconstructed ratio is corrected only in its primary component and not for the secondary Λ^0.

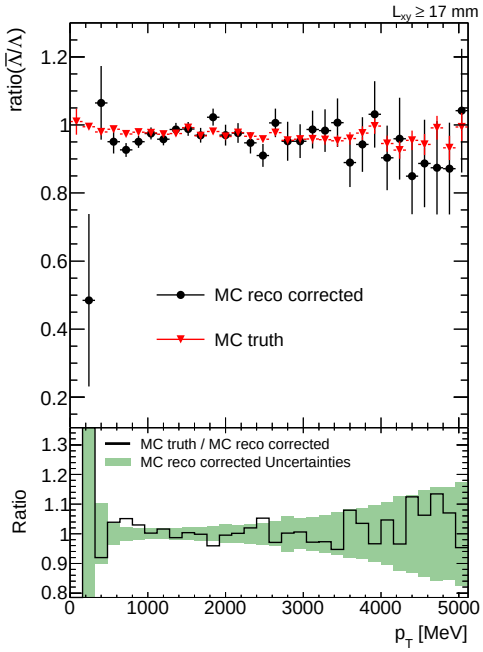

Figure 5.21: Closure test for the $\overline{\Lambda^0}$-to-Λ^0 ratio as a function of the transverse momentum. The red and black points corresponds to the $\overline{\Lambda^0}/\Lambda^0$ ratio in the truth and for the reconstructed in MC and efficiency corrected candidates respectively. The errors are statistical only. The ratio between the truth and the corrected $\overline{\Lambda^0}/\Lambda^0$ is shown in the bottom, where the green band represent the statistical error of the reconstructed and corrected $\overline{\Lambda^0}/\Lambda^0$ ratio.

5.8 Systematic uncertainties

The main systematic effects that have been considered for the $\overline{\Lambda^0}/\Lambda^0$ production ratio measurements are the following:

- the difference of the proton and antiproton interaction cross section with the material of the Inner Detector;
- contamination from secondary production of $\overline{\Lambda^0}$ and Λ^0 candidates originating from the decay of other particles or generated by the interaction of other primary particles with the material);
- the interactions of Λ^0 and $\overline{\Lambda^0}$ with the material before decaying;
- the uncertainty on the material budget.

All these effects are strictly related to the material model in Monte Carlo. Thus, the optimal way to study these systematics is to consider variations of the ratio following the material distribution in the Inner Detector. Figure 5.22 shows the schematic view of the ATLAS Inner Detector in the barrel region. In this region, the beam pipe and the different layers of the Inner Detector

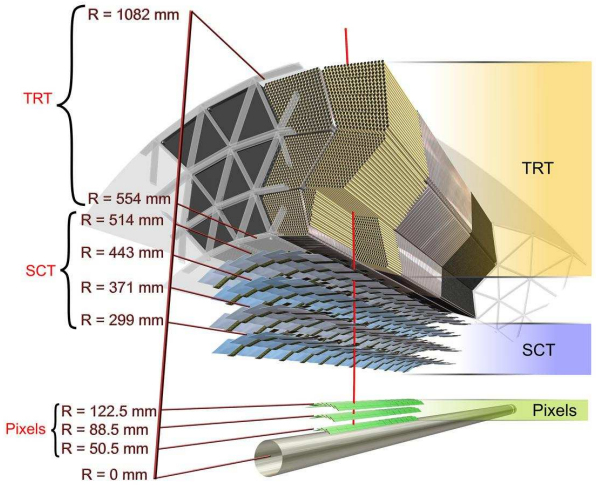

Figure 5.22: Schematic view of the ATLAS Inner Detector in the barrel region. The beam pipe is located at a radius of ∼3 cm while all the other radial position of the Pixel and SCT layer are reported in the picture.

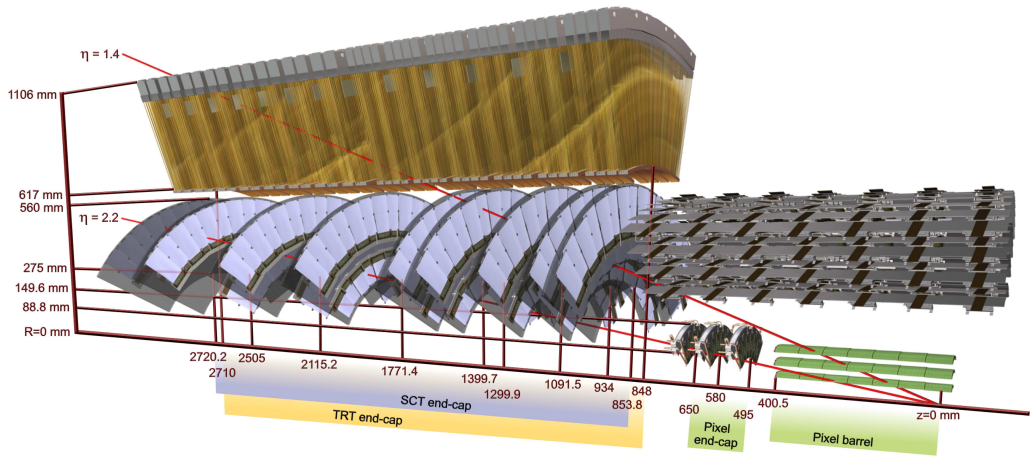

Figure 5.23: Schematic view of the ATLAS Inner Detector in the endcap region. The $|z|$ position of the first Pixel ring is at 49.5 cm while the barrel coverage of innermost Pixel layer is at $|z| = 400.5$ mm.

are located radially: the beryllium beam pipe is located at ∼30 mm from the beam axis; the three pixel layers are located respectively at 50.5 mm, 88.5 mm and 122.5 mm; the SCT layers are located between 299 mm and 514 mm; finally the TRT detector span between 554 mm and 1082 mm. Figure 5.23, instead, shows the z (longitudinal) position of sensors and structural elements of the ATLAS Inner Detector in the endcap region.

The $\overline{\Lambda^0}$-to-Λ^0 ratio reconstructed in barrel and endcap regions of the Inner Detector as a function of the radial position of the decay vertex are shown in figure 5.24 for both data and simulation. This is shown separately for $|\eta| < 0.9$, $0.9 < |\eta| < 2$ and $2 < |\eta| < 2.5$. In MC, where the reconstructed candidates are also matched with primary Λ^0 or $\overline{\Lambda^0}$, it is clearly visible how the ratio changes sharply at the beam pipe and at the first Pixel layer and, although not so pronounced, also at the radius of the other Inner Detector layers. Between the structures, the ratio is relatively flat. The radial shape of the ratio in data shows a similar behavior. Moreover, the different jumps are clearly visible in the region $|\eta| < 2$ while, as expected by geometrical considerations, no radial

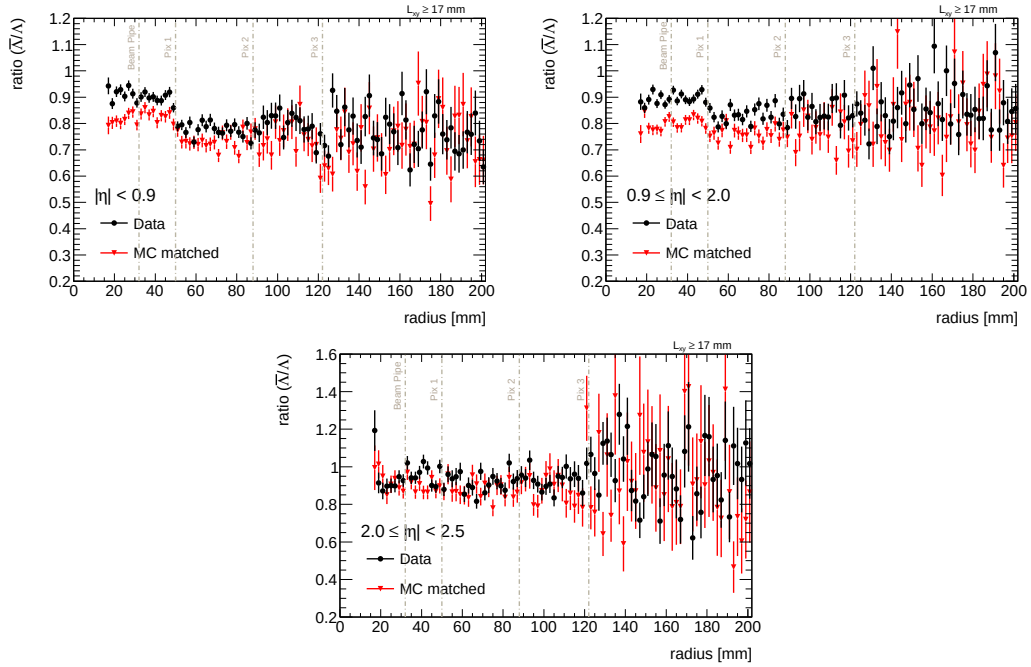

Figure 5.24: $\overline{\Lambda^0}$-to-Λ^0 ratio versus the radial position of the decay vertex for reconstructed candidates in MC simulation and matched with the Monte Carlo truth (red) and for candidates reconstructed in data in a mass window of $\pm$ 7 MeV around the Λ baryon mass PDG value. The candidates are required to have $|\eta| < 0.9$ (top left), $0.9 < |\eta| < 2$ (top right) and $2 < |\eta| < 2.5$ (bottom).

structure is visible in the endcap region [3].

5.8.1 Proton and Antiproton hadronic interaction cross section

The interactions of charged particles with material are the main efficiency-loss mechanism. A charged particle that interacts with the detector material does not have hits on track after interacting, thus decreasing the efficiency of pattern

[3] In that region the distance from the interaction point to the first detector layer is larger than the mean flight length path of Λ^0 and $\overline{\Lambda^0}$ and so most of the candidates decays before to reach it.

recognition, which has implicit hit requirements (e.g. a minimum of three space points is required to form a track seed). Since the protons and antiprotons originating from the decay of Λ^0 and $\overline{\Lambda^0}$ traverse different active detector layers (Pixel, SCT, TRT) in order to be reconstructed, the knowledge of the hadronic interaction cross section for protons and antiprotons is important for the $\overline{\Lambda^0}$-to-Λ^0 ratio measurement. Figure 5.25 shows the inelastic cross section as a function of the proton (or antiproton) momentum for proton with carbon (left) and antiproton with carbon (right) measured and compared to the curves implemented in different simulation packages: GEANT3, GEANT4 (used for the ATLAS simulation) and FLUKA [69, 70]. For the inelastic cross section of protons with carbons, both GEANT3 and GEANT4 agree with the existing data. On the other hand, for the antiprotons, both GEANT3 and GEANT4[4] overestimate the cross section with respect to data while the FLUKA package is in agreement with data. Thus, a lower reconstruction efficiency for antiprotons in Monte Carlo simulation with respect to data is expected, giving a lower $\overline{\Lambda^0}$

[4]For GEANT4 different transport models are possible. For all of them the stated consideration are valid .

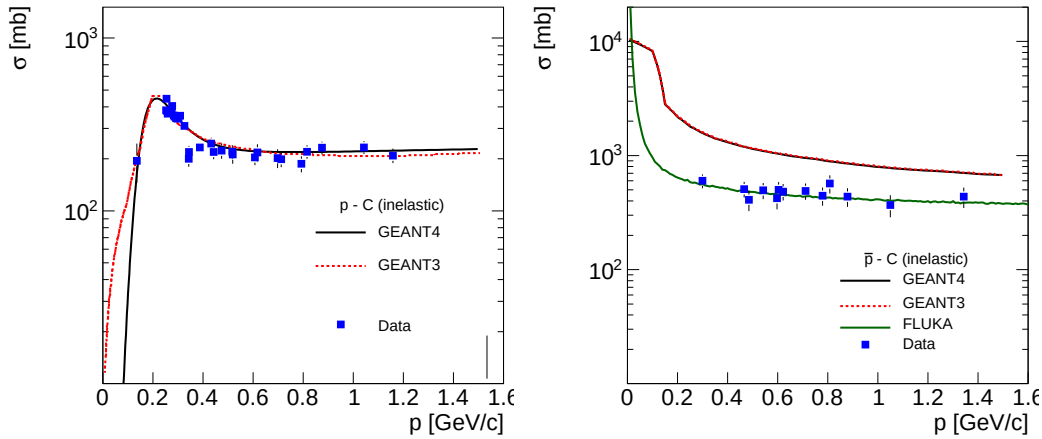

Figure 5.25: Inelastic hadronic cross section for protons (left) and antiprotons (right) with carbon in experimental data and in several simulation packages.

MC reconstruction efficiency. The effect of this cross section overestimation is to have an MC correction applied to the data that is higher for $\overline{\Lambda^0}$, bringing the $\overline{\Lambda^0}$-to-Λ^0 ratio to a higher value than the physical one. This can explain the behavior of the corrected $\overline{\Lambda^0}$-to-Λ^0 ratio showed in figure 5.19 that is higher than unity for most of the bins. In order to correct for this effect, two different methods can be explored: the track-length study and the proton-antiproton SCT extension efficiency study based on the dE/dx tagging of the tracklets.

Track-length study

The track-length study method is based on the comparison in both data and MC simulation between the fractions of tracks that have different pattern of hits (hit mask) in the last two SCT layer (and having the hits in all the others). Figure 5.26 shows two out of three different possible masks that will be considered. Different hadronic cross section for protons and antiprotons

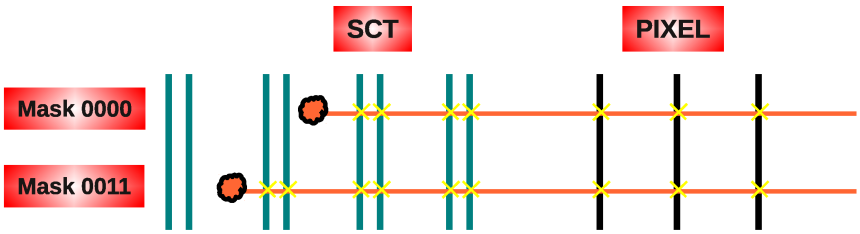

Figure 5.26: Schematic view of the hit masks corresponding to track having all th pixel hits and all the SCT hits without the last two layers (Mask 0000) or without hits in the last SCT layer (Mask 0011).

in data and MC simulation will give different fractions among the different masks. For example, a higher cross section for antiprotons in Monte Carlo simulation with respect to the data will give a higher fraction of tracks with missing hits in the last SCT layer due to the fact that in MC they have a higher probability to interact with the material there. As source of protons and antiprotons, the tracks with the higher transverse momentum of Λ^0 and $\overline{\Lambda^0}$

candidates can be used, with the possibility to threat the background applying a subtraction using the sidebands of the invariant mass peak.

dE/dx study

An approach similar to the track-length study is to use the dE/dx measurement performed with the Pixel detector to constrain and correct the difference in antiproton and proton reconstruction efficiency. The track or pixel tracklet dE/dx can be measured starting from the charge collected in the pixel clusters associated with the track (or the tracklet) itself. To have a good measurement at the track level, a selection at the cluster level is applied in order to be sure that the charge has been properly collected. Figure 5.27 shows the dE/dx measured as a function of momentum for tracks in $\sqrt{s}$ =7 TeV minimum bias data having at least 3 good pixel clusters associated with the tracks. One way that can be used to constrain the antiproton interaction modeling in MC is to use the SCT extension efficiency. In this method the matching efficiency of a pixel tracklet to a combined silicon track is calculated. The matching procedure can be performed using a hit based or a ΔR matching. The dE/dx measurement can be used to reliably tag proton and antiproton tracklets only

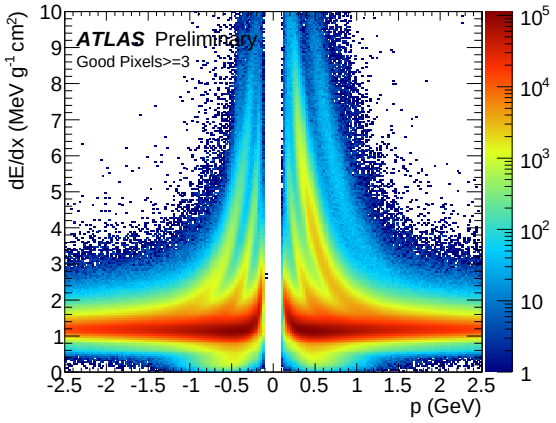

Figure 5.27: dE/dx measured as a function of momentum for tracks in 7 TeV minimum bias data having at least 3 good cluster.

in the momentum range between ∼400 MeV and ∼1.2 GeV. The antiproton-to-proton in data and MC simulation will be compared in this this range in order to have to correct MC-data adjustment.

5.8.2 Secondary Λ^0 and $\overline{\Lambda^0}$ production

Secondary production of Λ^0 and $\overline{\Lambda^0}$ particles can be obtained both from the interaction of particles with the material of the Inner Detector and from the decay of higher masses strange baryons like Σ or Ξ. These Λ^0 have an invariant mass peak as the primary Λ^0 and $\overline{\Lambda^0}$ produced; thus they are counted as signal component in the background-subtracted p_T, η and y distributions. Figure 5.28 shows for example the production vertex position in the transverse plane for the secondary generated Λ^0 baryons in the barrel region ($|z| < 420$ mm of the production vertex) in Monte Carlo simulation . This plot shows :

- the secondary Λ^0 originating from the decay of Σ or Ξ for which the production vertex is mainly located before the beam pipe and the other detector layers;
- the Λ^0 baryons with the production vertex located close to a detector

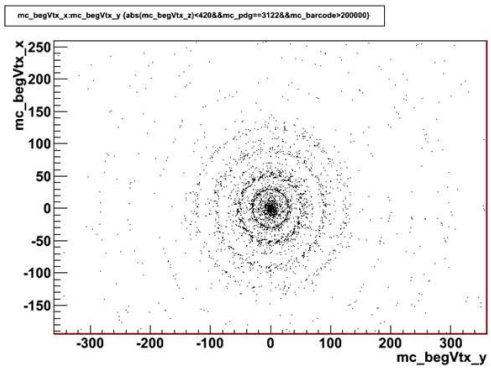

Figure 5.28: Production vertex position in the transverse plane for the secondary generated Λ^0 in Monte Carlo simulation. Only Λ^0 with $|z| < 420$ mm are considered (barrel region).

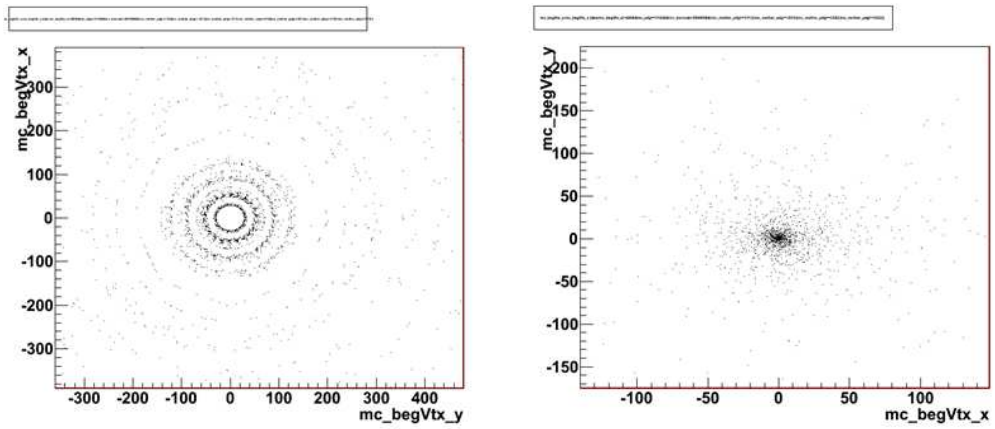

Figure 5.29: Production vertex position in the transverse plane for the secondary generated Λ^0 in Monte Carlo simulation that come from Σ and Ξ decay (left) or not (right). Only Λ^0 with $|z| < 420$ mm are considered (barrel region).

element of the Inner Detector.

These two components can by easily distinguished by requiring that these secondary Λ^0 originate from a Σ or Ξ decay, as shown in figure 5.29 where the candidates in figure 5.28 are splitted according to this requirement.
Most of the contribution from the decay of other strange baryons is then eliminated with the transverse flight length cut.
The secondary Λ^0 and $\overline{\Lambda^0}$ originating from the interaction of other particles with the detector material are expected to be less pointing and with a lower momentum with respect to the primary one. Figure 5.30 shows the ratio of reconstructed Λ^0 candidates in the MC sample matched to secondary and primary baryons in MC truth, evaluated versus the transverse momentum (left) and the cosine of the pointing angle (right). The same secondary to primary ratio as a function of p_T and the cosine of the pointing angle for $\overline{\Lambda^0}$ candidates are shown in figure 5.31. As expected, the contamination is higher at low momenta and lower values of the cosine of the pointing angle for both Λ^0 and $\overline{\Lambda^0}$ candidates. In order to see the effect of the secondary component in the

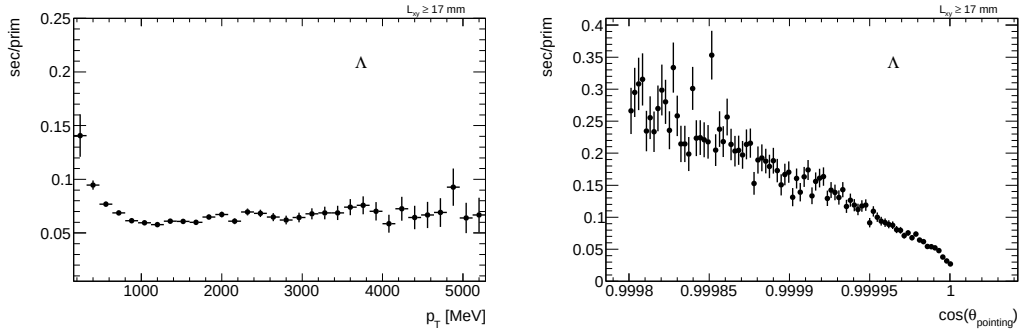

Figure 5.30: Ratio of reconstructed Λ^0 candidates in the Monte Carlo matched to secondary and primary baryons in MC truth, evaluated versus p_T (left) and the cosine of the pointing angle (right) of the Λ^0 candidate.

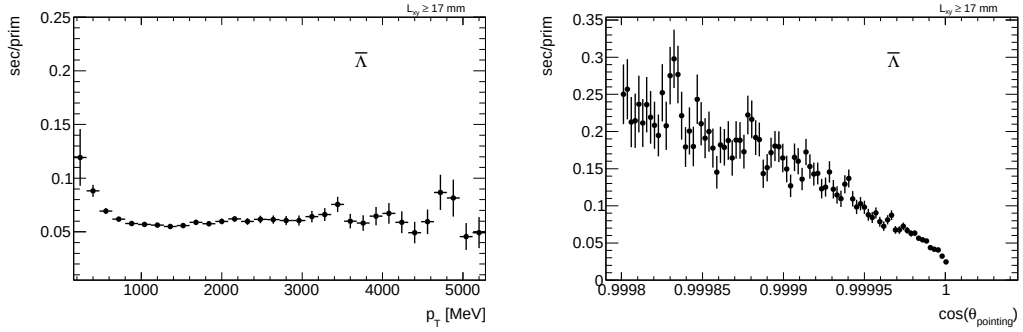

Figure 5.31: Ratio of reconstructed $\overline{\Lambda^0}$ candidates in the Monte Carlo matched to secondary and primary baryons in MC truth, evaluated versus p_T (left) and the cosine of the pointing angle (right) of the $\overline{\Lambda^0}$ candidate.

$\overline{\Lambda^0}$-to-Λ^0 ratio measurement, the selection on the cosine of the pointing angle has been tightened (from $\cos\theta_{pointing} > 0.9998$ to $\cos\theta_{pointing} > 0.99995$) and a new selection on the transverse momentum on the Λ^0 candidates has been added (p_T (Λ^0) >500 MeV). The combined effect of the two tight cuts on the secondary to primary ratio versus p_T and $\cos\theta_{pointing}$ is shown respectively for Λ^0 in figure 5.32 and for $\overline{\Lambda^0}$ in figure 5.33. Table 5.2 summarizes the level

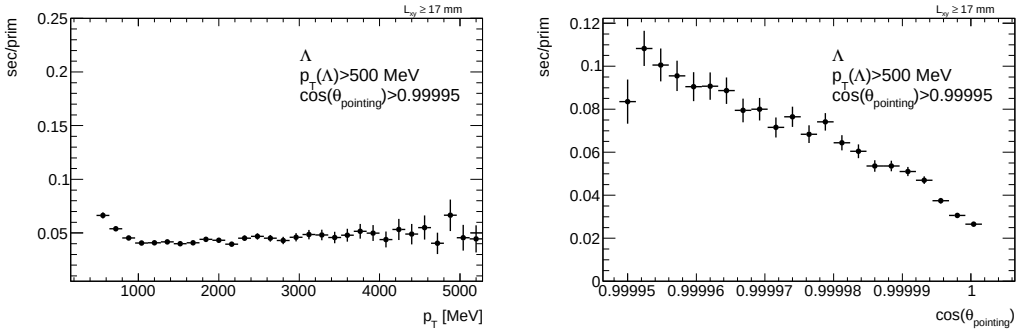

Figure 5.32: Ratio of reconstructed Λ^0 candidates in the Monte Carlo matched to secondary and primary baryons in MC truth, evaluated versus p_T (left) and the cosine of the pointing angle (right) of the Λ^0 candidate. A p_T (Λ^0) >500 MeV cut and $\cos\theta_{pointing} > 0.99995$ cut have been applied.

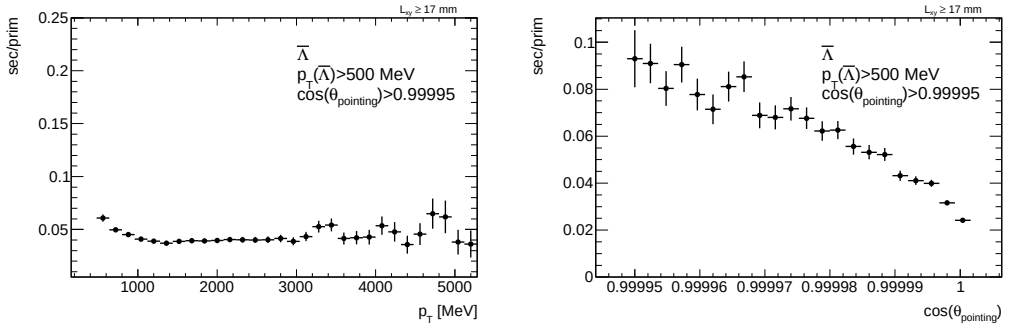

Figure 5.33: Ratio of reconstructed $\overline{\Lambda^0}$ candidates in the Monte Carlo matched to secondary and primary baryons in MC truth, evaluated versus p_T (left) and the cosine of the pointing angle (right) of the $\overline{\Lambda^0}$ candidate. A p_T (Λ^0) >500 MeV cut and $\cos\theta_{pointing} > 0.99995$ cut have been applied.

of contamination separately for Λ^0 and $\overline{\Lambda^0}$ in the full acceptance and in the region $|\eta(\Lambda^0)| < 0.9$.

All candidates			$\|\eta(\Lambda^0)\| < 0.9$		
	Λ^0	$\overline{\Lambda^0}$		Λ^0	$\overline{\Lambda^0}$
Reference cuts	5.2%	4.9%	Reference cuts	5.1%	4.6%
Tight cuts	3.8%	3.6%	Tight cuts	3.6%	3.4%

Table 5.2: Level of contamination from secondaries for Λ^0 and $\overline{\Lambda^0}$ candidates considering all the candidates (left) and only the one satisfying the condition $|\eta(\Lambda^0)| < 0.9$ (right).

5.8.3 Interacting Λ^0 and $\overline{\Lambda^0}$

The interaction of primary Λ^0 and $\overline{\Lambda^0}$ baryons is another effect that has been studied in order to understand how it can change the measured ratio and how well it is described in the MC simulation. This effect can be studied again versus the decay radius since it is strictly related with the material distribution inside the Inner Detector. Λ^0 baryons that interact with the material are no longer reconstructible as V_0 candidates. In particular we expect a higher interaction cross section of $\overline{\Lambda^0}$ with the material with respect to the Λ^0; without this effect or with an equal cross section for Λ^0 and $\overline{\Lambda^0}$ baryons, we expect a flat shape for the truth $\overline{\Lambda^0}$-to-Λ^0 ratio as a function of the decay radius. Figure 5.34 shows the truth ratio (with the kinematical cuts applied to the daughters) versus the decay radius. The truth ratio is almost 99% before the first Pixel layer but then start to decrease as a function of the decay radius itself. Since this is done using the truth information, just requiring primary Λ^0 and $\overline{\Lambda^0}$ decaying in the proton-pion mode with the daughter in the kinematical acceptance without looking at the reconstructed ones, this effect can be explained by the primary Λ^0 and $\overline{\Lambda^0}$ baryons interacting with the material with a higher interaction cross section for $\overline{\Lambda^0}$. This is more clear looking at the ratio of the $\overline{\Lambda^0}$ over Λ^0 that interact with the material versus the interaction vertex radius (figure 5.35) These are chosen in Monte Carlo truth requiring Λ^0 and $\overline{\Lambda^0}$ baryons with more than two daughters. After the first

material layer (the beam pipe) the ratio of the interacting component jumps to a value for the ratio of ~ 2 and decrease with the radius. This is compatible with the hypothesis of a higher interaction cross section for the $\overline{\Lambda^0}$ with respect to the Λ^0. The number of produced Λ^0 and $\overline{\Lambda^0}$ is almost equal but, after the material layer, the available number of $\overline{\Lambda^0}$ that can interact in the next layer is lower than Λ^0 (due to the higher cross section). The left side of figure 5.36 shows the distribution of Λ^0 and $\overline{\Lambda^0}$ baryons interacting with detector material in the MC sample as a function of radius in the barrel region. The beam pipe, the regions covered by the Pixel modules and the support (the spikes at ∼70 mm,∼110 mm and ∼140 mm) are clearly visible. The right side of figure 5.36 shows the cumulative distribution[5] as a function of the radial position of the interacting $\overline{\Lambda^0}$ with $|\eta| < 0.9$.

This information can be used to try to recover the flat distribution in the MC truth of the $\overline{\Lambda^0}$-to-Λ^0 ratio. Since these candidates interact with the material, a priori they could have decayed in each of the possible decay mode accordingly

[5]The y value for a particular radial position represent the integral of the distribution of the radial position of the interaction vertex up this radial position.

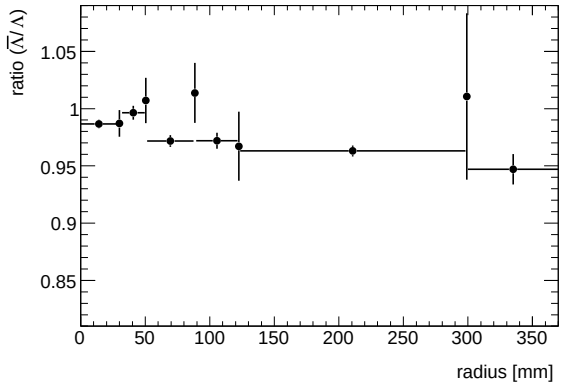

Figure 5.34: Generated $\overline{\Lambda^0}$-to-Λ^0 ratio in Monte Carlo generator as a function of the the decay radius. The plot is binned following the material distribution in the Inner detector. The decreasing behavior is due to the interaction with the material of primary Λ^0 and $\overline{\Lambda^0}$ baryons.

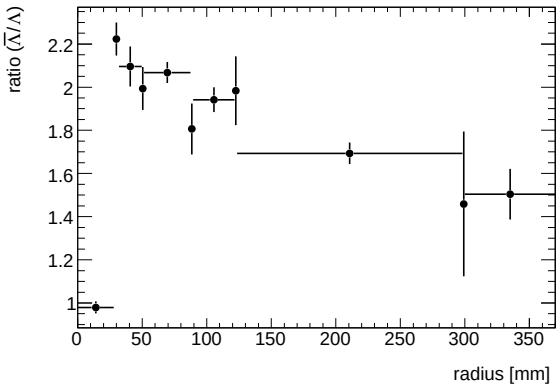

Figure 5.35: Ratio between the interacting $\overline{\Lambda^0}$ and Λ^0 baryons generated in Monte Carlo simulation as a function of the interacting radius.

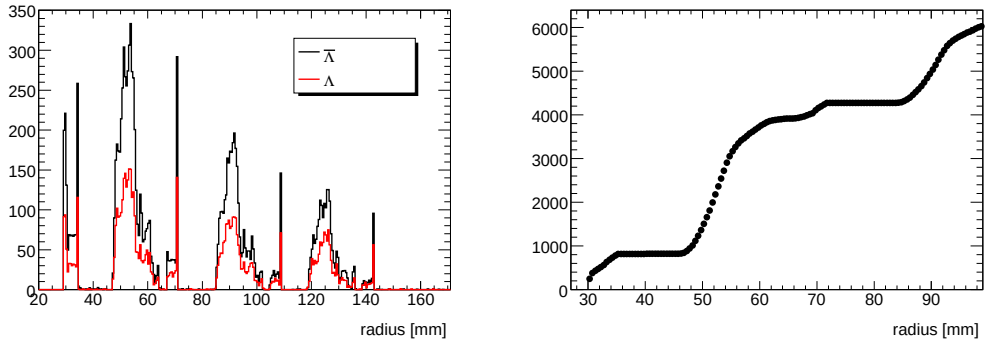

Figure 5.36: (left) Distribution of the radial position of the interaction vertex in Monte Carlo sample for Λ^0 (red) and $\overline{\Lambda^0}$ (black) having $|\eta|$ <0.9. (right) Cumulative distribution as a function of the radial position of the interacting $\overline{\Lambda^0}$ with $|\eta|$ <0.9.

to their branching fraction and so only the 63.9% (that corresponds to the proton(antiproton) pion branching fraction) will contribute. Given a Λ^0 (or $\overline{\Lambda^0}$) that interacts, if it did not interact (no material hypothesis), this Λ^0 (or $\overline{\Lambda^0}$) baryon could have contributed to any of the following decay radius bins according to the decay-time distribution. Each MC truth bin of the transverse

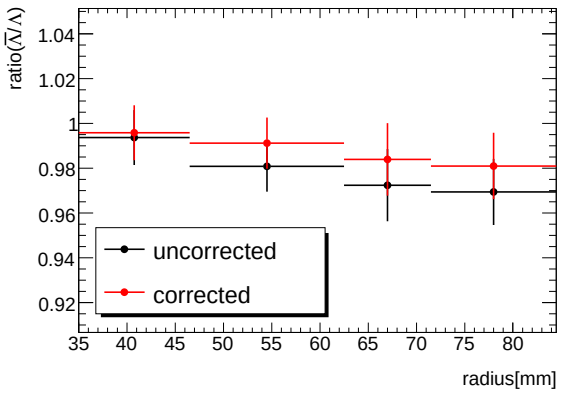

Figure 5.37: MC truth $\overline{\Lambda^0}$-to-Λ^0 ratio versus the decay radius in the range 35-80 mm uncorrected (black) and corrected (red) with the correction procedure described in the text. The errors are statistical.

decay radius of Λ^0 (or $\overline{\Lambda^0}$) is corrected with the following factor

$$Correction = N \cdot \frac{A}{B + C} \tag{5.8.1}$$

where

- **N** is the number of Λ^0 (or $\overline{\Lambda^0}$) that interact in the bin that is going to be corrected, adding also any remainder from the previous bins;
- **A** is the number of Λ^0 (or $\overline{\Lambda^0}$) that decay in the radial bin that is going to be corrected;
- **B** is the number of Λ^0 (or $\overline{\Lambda^0}$) that decay after the radial bin that is going to be corrected;
- **C** is the number of Λ^0 (or $\overline{\Lambda^0}$) that interact after the radial bin that is going to be corrected.

The impact of this correction applied for both the Λ^0 and $\overline{\Lambda^0}$ decay radius distributions in the $\overline{\Lambda^0}$-to-Λ^0 ratio versus the decay radius in the range 35-80 mm is shown in figure 5.37. This procedure corrects the truth ratio for the in-

teraction component in the right direction, even if it is not completely perfect. This is due to implicit assumptions done of an equal p_T distribution for the interacting and non-interacting Λ^0 (or $\overline{\Lambda^0}$) and for the fact that the material is assumed to be only at the beginning of each bin.
It is clear from the arguments treated in this paragraph that the truth distribution has inside these Λ^0 and $\overline{\Lambda^0}$ interactions and it is impossible to recover for all of them. This means that the truth distributions that we have used to evaluate the Λ^0 and $\overline{\Lambda^0}$ reconstruction efficiencies are not completely correct and this is true only when we consider Λ^0 and $\overline{\Lambda^0}$ with a decay radius that goes over the first Pixel layer. To take into account this effect, a systematic of 1.5% calculated as the difference in the truth ratio after and before the first Pixel layer weighted by the number of candidates reconstructed after and before the first Pixel layer is assigned.

5.8.4 Extra-material samples

An additional systematic due to the total amount of material knowledge is evaluated using two additional Monte Carlo simulation samples[6] for which the amount of material has been increased by 5% and 10% respectively. These samples are used to calculate new efficiencies that have been used to correct the Λ^0 and $\overline{\Lambda^0}$ p_T, η and y background-subtracted data distributions. Figure 5.38 shows the $\overline{\Lambda^0}$-to-Λ^0 ratio in the data corrected for detector effects using the nominal and extra-material Monte Carlo samples. Due to the lower statistics for the extra-material Monte Carlo samples, the sensitivity of this method is

[6]Non diffractive events generated with PYTHIA like the nominal one. The statistics for these samples is limited to 5 million events.

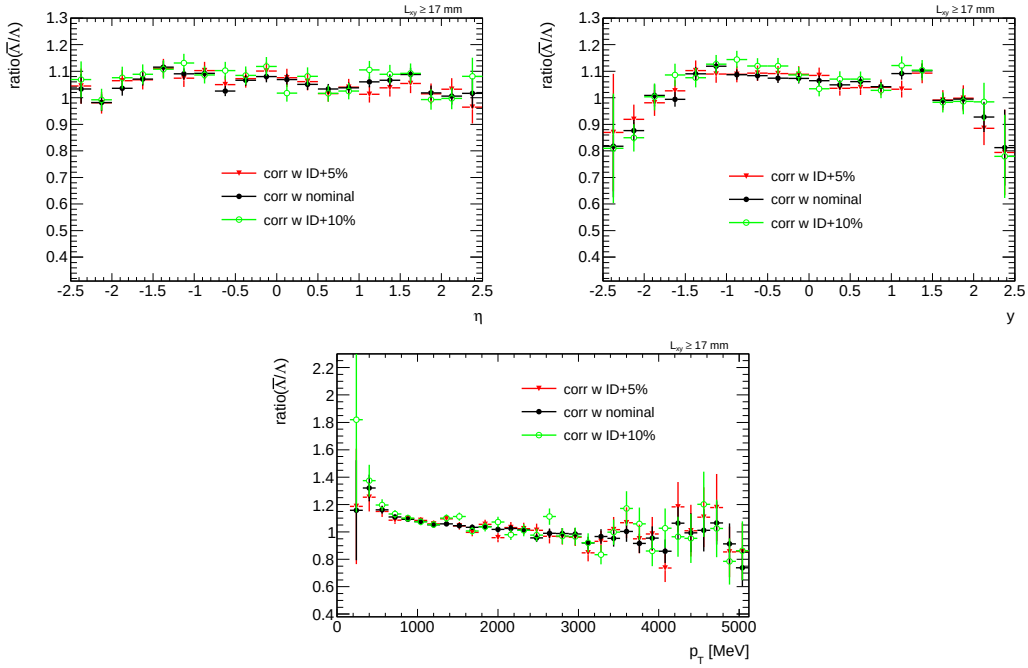

Figure 5.38: $\overline{\Lambda^0}$-to-Λ^0 ratio in data corrected for detector effects using MC efficiencies derived from the nominal (black) and extra-material (red for 5% and green for 10% ID extra-material) Monte Carlo samples versus pseudorapidity (top left), rapidity (top right) and transverse momentum (bottom).

at the level of few percent. Thus no significant deviation is visible with this precision, even for the sample with 10% of extra-material.

5.8.5 Systematics summary

Figure 5.39 shows the background-corrected reconstructed $\overline{\Lambda^0}$-to-Λ^0 candidates ratio in data and MC versus decay radius, binned according to the material geometry in the barrel (top left), in the transition region (top right) and versus the $|z|$ position of the decay vertex for candidates with $2.0 < |\eta| < 2.5$. As discussed in the previous paragraphs, the jumps in correspondence of detector bins are mainly caused by the effect of the secondary production of Λ^0

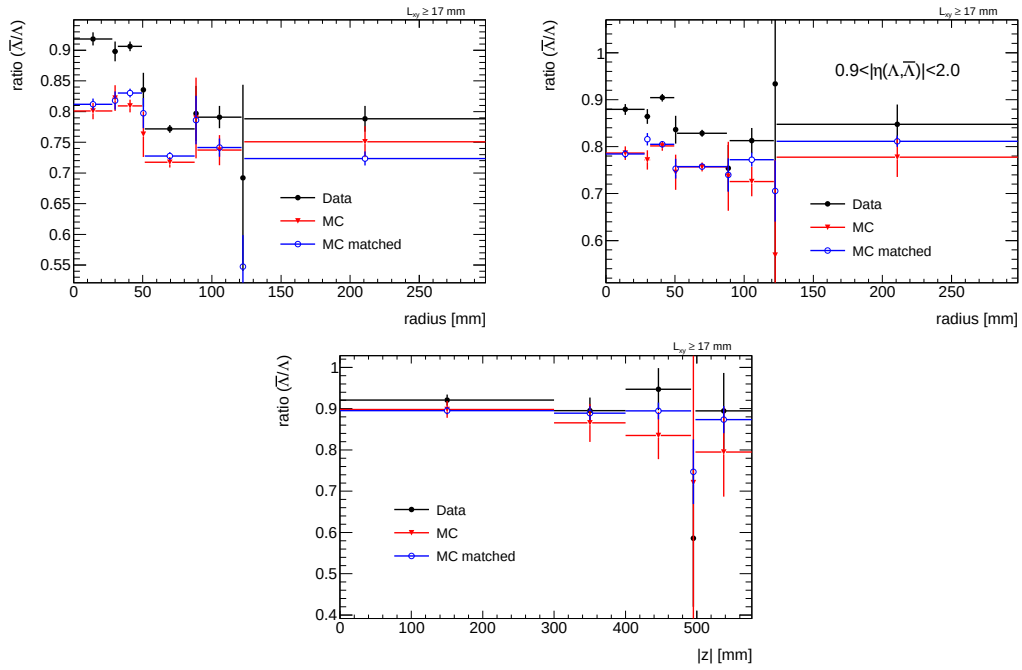

Figure 5.39: $\overline{\Lambda^0}$-to-Λ^0 ratio evaluated versus the radial position of the decay vertex for data (black), MC (red), and MC primary-matched (blue) for candidate with $|\eta| < 0.9$ (top left) and $0.9 < |\eta| < 2.0$ (top right). $\overline{\Lambda^0}$-to-Λ^0 ratio evaluated the z position of the decay vertex for data (black), MC (red), and MC primary-matched (blue) for candidate with $2.0 < |\eta| < 2.5$ (bottom)

and $\overline{\Lambda^0}$ and the interaction of Λ^0 and $\overline{\Lambda^0}$ with the material while the overall mismodeling of the antiproton cross section affects all the bins and cannot be disentangled from the truth physical ratio we want to measure. In particular before the first Pixel layer only the proton-antiproton effect and the physical one enter causing the discrepancy between data and MC; after the first pixel layer, also the effect of the interaction and secondary production of Λ^0 and $\overline{\Lambda^0}$ contributes.

A global systematic is evaluated in order to take into account the differences between data and MC simulation given by these two effect: a systematic is assigned on the shape of the $\overline{\Lambda^0}$-to-Λ^0 ratio versus the decay radius (or $|z|$ in for candidates with $2.0 < |\eta| < 2.5$). In particular this contribution is evaluated calculating the difference of the jumps after and before each material bin in data and simulation weighted by the variance (that contains the informations on the amount of Λ^0 and $\overline{\Lambda^0}$ that decay in a particular bin and the quality of the fit).

In the barrel region the following four jumps have been considered: before and after the beam pipe, before and after the first pixel layer, before and after the second pixel layer and before and after the third pixel layer. The final systematics for each region has been evaluated using the following formula:

$$Sys = \frac{\sum_j \frac{\Delta(jump)_j}{\sigma_j^2}}{\sum_j \frac{1}{\sigma_j^2}} \tag{5.8.2}$$

where $\Delta(jump)_j$ is the value of the difference of a particular jump between data and MC while σ_j is the error associated to this difference. The values of the difference of these jumps between data and Monte Carlo simulation for the candidate with $|\eta| < 0.9$ with the relative $1/\sigma^2$are reported in table 5.3. For the candidates in the region $0.9 < |\eta| < 2.0$ the systematic error has been evaluated in the same way, obtaining a value of 2.7%. In the forward region, the systematic evaluated using the same procedure for the jumps along the $|z|$ bins of the $\overline{\Lambda^0}$-to-Λ^0 ratio is 2.5%.

These systematic errors are applied only for the candidates that decay after

$\|\eta\| < 0.9$		
Jump	(Data - MC) [%]	$1/\sigma^2$
After-Before Beam Pipe	1.73	0.227
After-Before Beam Pix 1	3.86	0.364
After-Before Beam Pix 2	0.18	0.098
After-Before Beam Pix 3	3.11	0.051
Weighted Mean		
2.7%		

Table 5.3: Values of the difference of the jumps of the $\overline{\Lambda^0}$ t Λ^0 ratio between data and Monte Carlo simulation for the candidate with $|\eta| < 0.9$ with the relative $1/\sigma^2$.

Systematic Uncertainty	Systematic		
	$\|\eta\| < 0.9$	$0.9 < \|\eta\| < 2.0$	$2.0 < \|\eta\| < 2.5$
Interaction on truth	1.5%	1.5%	1.5%
Systematic on the ratio shape	2.7%	2.7%	2.5%

Table 5.4: Summary of the systematic uncertainties considered for the $\overline{\Lambda^0}$-to-Λ^0 ratio measurement. The values correspond to the absolute uncertainty on the ratio.

the first pixel layer.

The summary of all the systematics evaluated, organized in the three different pseudorapidity regions considered, are reported in table 5.4.

5.9 Final Results

Figure 5.40 shows the $\overline{\Lambda^0}$-to-Λ^0 ratio corrected for the efficiency effects versus the rapidity, the pseudorapidity and the transverse momentum. The green band corresponds to the sum in quadrature of the statistical and systemati-

cal uncertainties. The correction for the mismodeling of the antiproton cross section effect is missing because still under investigation. In order to cross-

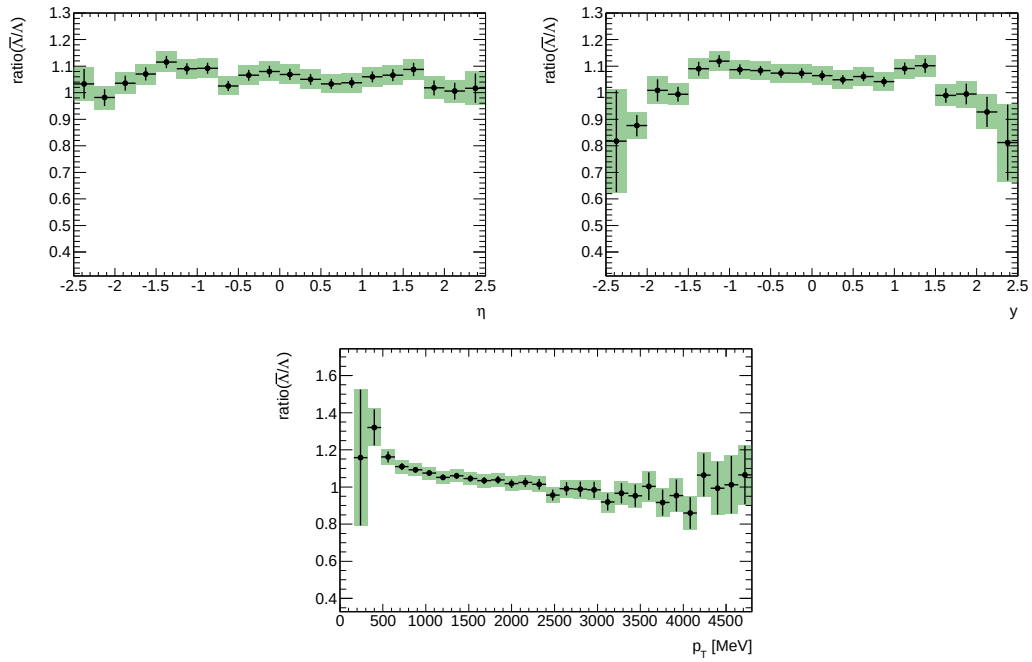

Figure 5.40: $\overline{\Lambda^0}$-to-Λ^0 ratio evaluated versus η (top left), y (top right) and p_T (bottom). Black points are data with the error bars representing the statistical uncertainty while the green area represent the sum in quadrature of the statistical and systematic uncertainties.

check the evaluation of the systematics due to the effects of the secondary production and the interaction of Λ^0 and $\overline{\Lambda^0}$, the ratio was also measured only for candidates that decay before the first pixel layer ($r < 49.5$ mm)[7]. These candidates in fact are affected only by the mismodeling of the antiproton cross section effect and are free from the secondary production or interaction of Λ^0 and $\overline{\Lambda^0}$. Thus the systematic uncertainties evaluated in the previous section should cover the difference between the two measurements. The cut at $r < 49.5$ mm reflects in a half of the statistics available. Figure 5.41 shows $\overline{\Lambda^0}$-to-Λ^0

[7]Also the efficiencies have been recalculated imposing the same radial cut also in the Monte Carlo truth

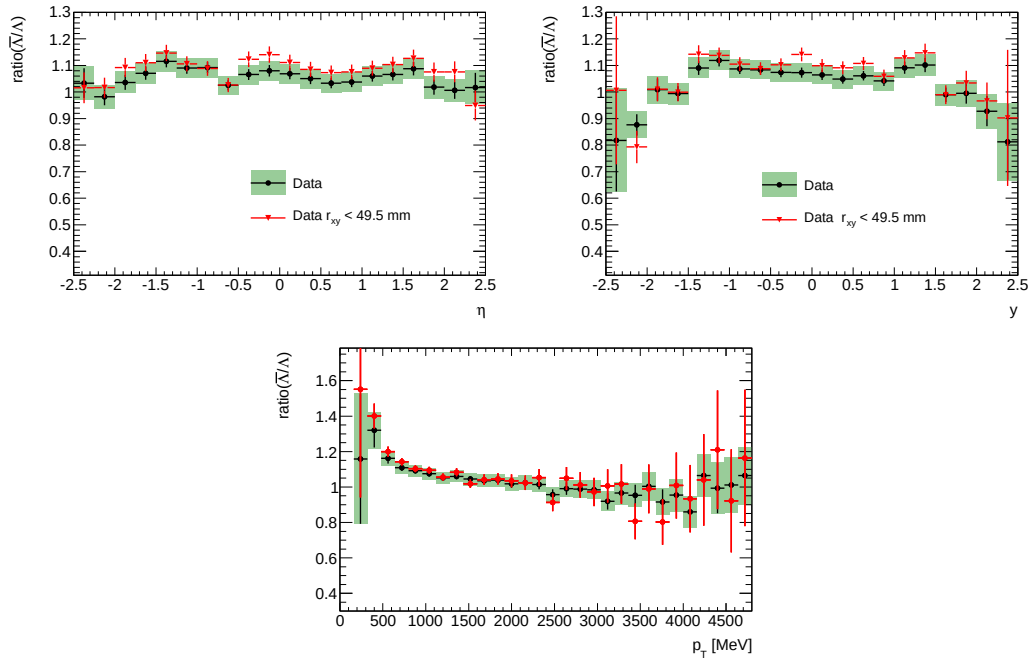

Figure 5.41: $\overline{\Lambda^0}$-to-Λ^0 ratio evaluated versus η (top left), y (top right) and p_T (bottom). Black points are data with the error bars representing the statistical uncertainty while the green area represents the sum in quadrature of the statistical and systematic uncertainties. The red points represent the same measurement done with Λ^0 and $\overline{\Lambda^0}$ candidates having a decay radius that satisfy the condition $r < 49.5$ mm.

ratio versus the rapidity, the pseudorapidity and the transverse momentum for all the candidates (black points and green area) and for candidates with the decay radius $r < 49.5$ mm (red points). As expected, the ratio is ∼2% higher (in rapidity and pseudorapidity), due to the fact that the secondary and interacting effect are absent and the systematic uncertainty assigned to the full measurement covers this difference.

Finally a preliminary $\overline{\Lambda^0}$-to-Λ^0 ratio versus the transverse momentum has been evaluated correcting for the effect due to the mismodeling of the antiproton cross section with material using the preliminary result of the track-lenght study. The result is shown in figure 5.42. The correction factor is obtained

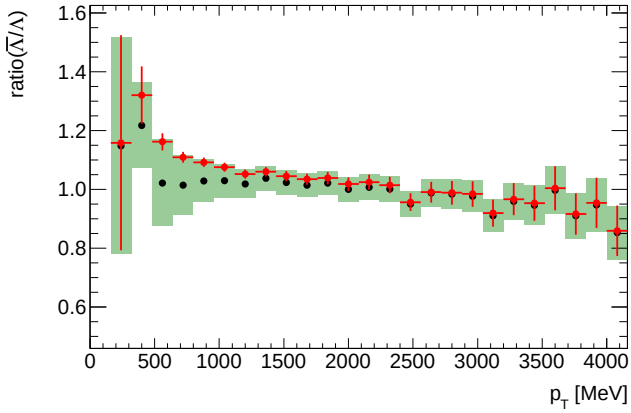

Figure 5.42: The ratio between $\overline{\Lambda^0}$ and Λ^0 baryons in data versus p_T, corrected for detector effects using the track-length study (black points, with the band showing statistical and systematic uncertainties added in quadrature). The red points with statistical-uncertainty bars show the $\overline{\Lambda^0}$-to-Λ^0 ratio without this additional correction.

calculating the ratio between Monte Carlo and data of the antiproton/proton ratio. This double ratio represents a scale factor for the antiproton mismodeling in data and it deviates from unity at low p_T and approaches the unity above 1.3 GeV. This correction factor has been calculated as a function of the proton p_T. The proton correction has been used, weighted by the distribution of the proton p_T in a given Λ^0 p_T bin, to convert this scale factor from the proton transverse momentum to the p_T of the Λ^0. The difference of the scale factor from unity has been taken as a additional conservative systematic uncertainty.

Chapter 6

Conclusions and Future Prospectives

The study of the production of the K^0_s meson, Λ^0 and $\overline{\Lambda^0}$ baryons using the first $190\mu b^{-1}$ of proton-proton collision data collected with a Minimum Bias Trigger in the ATLAS experiment has been the main subject of this thesis. After the description of the LHC accelerator and of the ATLAS experiment, I have presented the main features of the soft proton-proton collisions and the first measurement of the charged particle distributions at the center-of-mass energy of $\sqrt{s} = 900$ GeV and $\sqrt{s} = 7$ TeV.

The analysis developed for the reconstruction of K^0_s, Λ^0 and $\overline{\Lambda^0}$ particles and the comparison of their kinematical distribution with the Monte Carlo prediction are widely discussed in chapter three. A good agreement in most of the distributions has been found demonstrating an excellent modeling of the Inner Detector response in the Monte Carlo simulation. Moreover the mass values have been compared with the PDG values showing a good agreement. Correlations between the average p_T of K^0_s and Λ^0 candidates with the number of charged tracks reconstructed and of the mean number of K^0_s with the number of charged tracks reconstructed have also been studied. These variables are related to the general characteristics of strangeness production in Minimum Bias events.

In the chapter four I have discussed the theoretical background on the baryon number transport in hadronic interactions and summarized the results from other experiments. Finally, in chapter five, I have presented the preliminary measurement of the ratio between $\overline{\Lambda^0}$ and Λ^0 particles versus pseudorapidity, rapidity and transverse momentum. The ATLAS measurement complements the recent measured result on baryon-number transport from the ALICE experiment using the primary antiproton-proton ratio [53].

Appendix A

Track reconstruction in the ATLAS Inner Detector

The reconstruction of the track of charged particles proceeds in two steps: the pattern recognition and the track fitting. The pattern recognition is needed in order to associate to a single charged particle the collection of hits generated in the detector through the deposit of energy by ionization in the detector sensitive elements when the charged particles go through it. Fake hits, coming mainly from other charged particles or detector noise, have to be excluded since they decrease the reconstruction accuracy. The track fitting consists in the estimation of the track parameters that describes the particle trajectory using the collection hits founded by the pattern recognition algorithms. With the fitting procedure the fake hits can be eliminated looking at the one that contribute disproportionately to the fit quality (typically the χ^2). The expected hit on tracks that are not found are commonly called holes.
The track reconstruction efficiency and the track parameter resolution are the two criteria to quantify the quality of a specific track reconstruction algorithm; however these criteria are not fully independent[1]. The tracking reconstruction algorithms that are used in ATLAS are called *New Tracking* or NEWT [71]:

[1]Hits that are wrongly associated to tracks during the pattern recognition decrease the quality of the measured track parameters.

this includes configurable algorithms run in a sequential way in order to reconstruct tracks in the most efficient way as possible.
The first sequence is known as the inside-out sequence, in which the tracks are reconstructed from the center of the Inner Detector outwards. Figure A.1 shows the different steps of the pattern recognition of the inside-out track reconstruction sequence. This sequence begins finding seed from groups of three space points in the silicon layers and proceeds using these seeds to build roads to find other hits moving towards the outer edge of the silicon detector. A single hit can be associated to more than one track and the ambiguity is solved rejecting poor track candidate until the hit is only attached to the most promising track candidates. The silicon track is then fitted and an extension to the TRT is probed; finally a complete track fit is performed to obtain the final estimation of the track parameters. The trajectory that a charged particle follows in a uniform magnetic field is approximately helical. Energy loss and multiple scattering, that depends from the energy of the particle and the amount of material the particle has traversed, are not taken into account in a perfect helical trajectory assumption but they can be considered in the track fit and in the propagation of the track parameters.

The trajectory parametrization can be made using a set of five parameters

$$\zeta = (d_0, z_0, \phi_0, \cot\theta, q/p_T) \tag{A.0.1}$$

where:

- d_0 is the transverse impact parameter corresponding to the distance of closest approach of the track to the reference point in the transverse (x-y) plane;

- z_0 is the longitudinal impact parameter corresponding to the z coordinate of the trajectory the point of closest approach;

- ϕ_0 is the azimuthal angle between the track and the tangent at the point of closest approach;

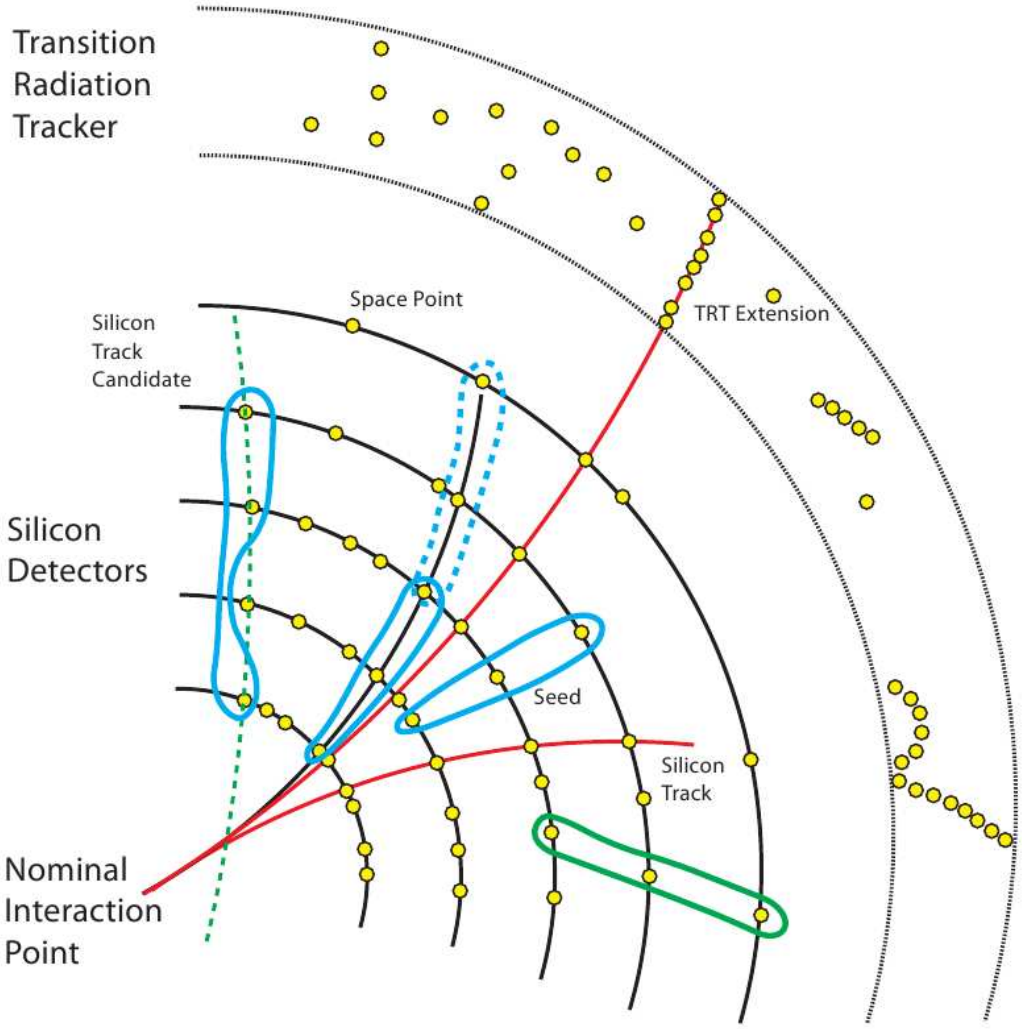

Figure A.1: Simplified model of the stages of the pattern recognition in the inner detector. Detector elements are shown in black while the hits are in yellow. The seeds are shown in blue. The dashed blue seed illustrates two seeds corresponding to the same track. The green seed is rejected because it is not consistent with a particle coming from the interaction point. Also the green dashed track candidate rejected because it is inconsistent with the nominal interaction point. The black track candidate is a fully reconstructed silicon track with no TRT extension while one of the red one have this extension.

- θ corresponds to the polar angle defined between the beam direction and the track in the r-z plane;
- q/p represents the curvature determined as the inverse of the momentum with the sign defined by the charge of the particle.

Figure A.2 shows the five track parameters in the transverse and longitudinal plane. The sign of the transverse impact parameter is determined by the following convention:

$$sign(d_0) = sign((\vec{p} \times \hat{z}) \cdot \vec{d}) \tag{A.0.2}$$

where $\vec{d}$ is the vector from the reference point to the point of closest approach, $\hat{z}$ is the versor pointing the positive $z-$axis and $\vec{p}$ is the momentum vector. The impact parameters d_0 and z_0 can be both calculated with respect to any appropriate reference point like the nominal interaction point (0,0,0) in the ATLAS coordinate frame, the reconstructed primary vertex or the beam spot. The distribution of the transverse impact parameters is frequently used in track selection since it can separate efficiently primaries from secondary particles.

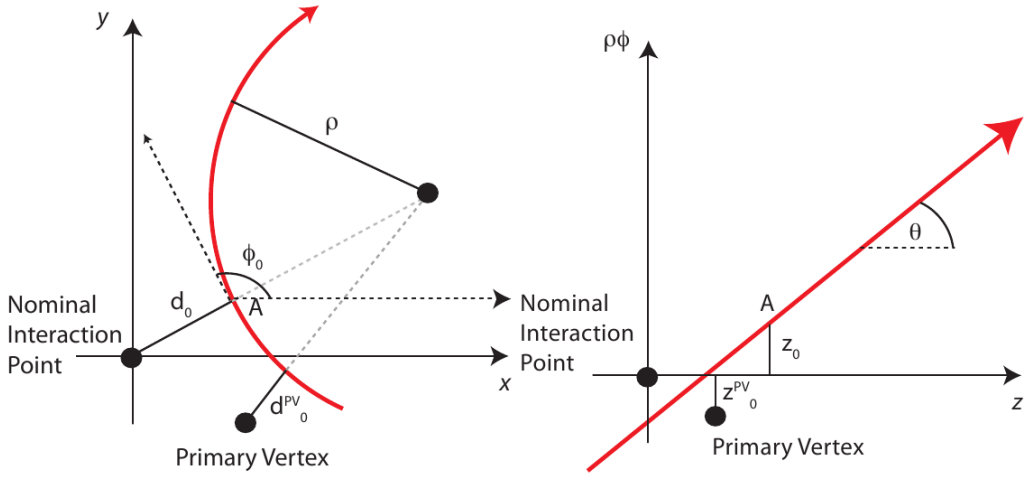

Figure A.2: The five track parameters in the transverse (left) and longitudinal (right) plane.

Bibliography

[1] L. Evans and P. Bryant (editors) 2008 "LHC Machine" JINST. 3 (2008) S08001.

[2] The LEP Study Group, "LEP Design Report", Vol. II, CERN LEP-TH/84-01 (1984).

[3] The ATLAS Collaboration, G. Aad et al, "The ATLAS Experiment at the CERN Large Hadron Collider", 2008 JINST 3 S08003

[4] The CMS Collaboration, S. Chatrchyan et al, "The CMS experiment at the CERN LHC", 2008 JINST 3 S08004

[5] The LHCb Collaboration, A. Augusto Alves Jr et al, "The LHCb Detector at the LHC", 2008 JINST 3 S08005

[6] The ALICE Collaboration, K. Aamodt et al, "The ALICE experiment at the CERN LHC", 2008 JINST 3 S08002

[7] The TOTEM Collaboration, G. Anelli et al, "The TOTEM Experiment at the CERN Large Hadron Collider", 2008 JINST 3 S08007

[8] The LHCf Collaboration, O. Adriani et al, "The LHCf detector at the CERN Large Hadron Collider", 2008 JINST 3 S08006

[9] The ATLAS Collaboration, "Magnet System Technical Design Report", CERN/LHCC/97-18, CERN, 1997.

[10] A. Yamamoto et al., "The ATLAS central solenoid", Nucl. Instrum. Meth. A 584 (2008) 53.

[11] The ATLAS Collaboration, "ATLAS Inner Detector: Technical Design Report. Vol. 1", CERN-LHCC-97-16.

[12] The ATLAS Collaboration, "ATLAS Inner Detector: Technical Design Report. Vol. 2", CERN-LHCC-97-17.

[13] ATLAS LAr Unit, "Liquid Argon Calorimeter Technical Design Report", Technical Report CERN/LHCC/96-41, CERN, 1996.

[14] ATLAS Tile Calorimeter Collaboration, "Tile Calorimeter Technical Design Report", Technical Report CERN/LHCC/96-42, CERN, 1996.

[15] ATLAS Muon Collaboration, "ATLAS Muon Spectrometer Technical Design Report", Technical Report CERN/LHCC/97-22, CERN, 1997.

[16] J. C. Barriere et al., "The alignment system of the ATLAS barrel muon spectrometer", ATL-MUON-PUB-2008-007 (2008).

[17] S. Aefsky et al., "The Optical Alignment System Of The Atlas Muon Spectrometer Endcaps", JINST 3 (2008) P11005.

[18] The ATLAS Collaboration,"Level 1 Trigger Technical Design Report", CERN/LHCC/98-14, CERN, 1998.

[19] The ATLAS Collaboration, "ATLAS DAQ, EF, LVL2 and DCS Technical Progress Report", CERN/LHCC/98-16, CERN, 1998.

[20] P. Lebrun, "Interim Summary Report of the Analysis of the 19 September 2008 Incident at the LHC", CERN EDMS 973073, ver. 1 (2008), available at:https://edms.cern.ch/document/973073/1.

[21] C. Ohm and T. Pauly, "The ATLAS beam pick-up based timing system", ATL-DAQ-PROC-2009-005 ; ATL-COM-DAQ-2009-022.

[22] D.S.J. Collins, "The Theorems of Perturbative QCD", Ann. Rev. Nucl. Part. Sci., 37 (1987), pp. 383-409.

[23] L.N. Lipatov, Sov. J. Nucl. Phys. **20** (1975) 95;
V.N. Gribov and L.N. Lipatov, Sov. J. Nucl. Phys. **15** (1972) 438;
G. Altarelli and G. Parisi, Nucl. Phys. **B126** (1977) 298;
Yu.L. Dokshitzer, Sov. Phys. JETP **46** (1977) 641.

[24] T. Regge. Nuovo Cimento, 14:951, 1959.

[25] V.N. Gribov. Sov. Phys. JETP, 53:654, 1967.

[26] A. Donnachie and P. V. Landsho , Phys. Lett. B 296 (1992) 227

[27] T. Sjostrand et al. "Pythia 6.4 Physics and Manual." JHEP, 05:026, 2006.

[28] T. Sjostrand and P.Z. Skands. "Multiple interactions and the structure of beam remnants." JHEP, 03:053, 2004.

[29] T. Sjostrand and M. van Zijl. "PA Multiple Interaction Model for the Event Structure in Hadron Collisions." Phys. Rev., D36:2019, 1987.

[30] R. Engel, "PHOJET Manual", http://physik.uni-leipzig.de/ eng/phojet.html

[31] A. Capella, U. Sukhatme, C.-I. Tan, J. Tran Thanh, "Dual parton model", Physics Reports, Volume 236, Issue 4-5, p. 225-329.

[32] B. M. Waugh et al., "HZTool and Rivet: Toolkit and Framework for the Comparison of Simulated Final States and Data at Colliders", 2006, arXiv:hep-ph/0605034.

[33] A. Buckley et al., "Systematic Event Generator Tuning for the LHC", Eur. Phys. J., C65:331-357, 2010.

[34] P. Z. Skands. "The Perugia Tunes", 2009. arXiv:0905.3418.

[35] Bonn-Brussels-Cambridge-CERN-Stockholm Collaboration and J G Rushbrooke, "The UA5 streamer chamber experiment at the SPS $p\bar{p}$ collider", 1981 Phys. Scr. 23 642

[36] M. Albrow et al. "Tevatron-for-LHC Report of the QCD Working Group". 2006.

[37] The ATLAS Collaboration,"Charged particle multiplicities in pp interactions at $\sqrt{s} = 0.9$ and 7 TeV in a diffractive limited phase-space measured with the ATLAS detector at the LHC and new PYTHIA6 tune", ATLAS-CONF-2010-031

[38] The ATLAS Collaboration,"Charged-particle multiplicities in pp interactions at $\sqrt{s}$= 900 GeV measured with the ATLAS detector at the LHC", Phys Lett B 688, 1, 21

[39] The ATLAS Collaboration,"Charged particle multiplicities in pp interactions for track $p_T > 100$ MeV at $\sqrt{s} = 0.9$ and 7 TeV measured with the ATLAS detector at the LHC", ATLAS-CONF-2010-046

[40] The ATLAS Collaboration,"Charged particle multiplicities in pp interactions at $\sqrt{s} = 2.36$ TeV measured with the ATLAS detector at the LHC" ATLAS-CONF-2010-047

[41] The ATLAS Collaboration,"Charged-particle multiplicities in pp interactions measured with the ATLAS detector at the LHC", Submitted to New J Phys (22 Dec 2010)

[42] G. Cohen-Tannoudji, A. E. Hssouni, J. Kalinowski, R. Peschanski, Phys. Rev. D19 (1979) 3397;
A. B. Kaidalov, Phys. Lett. B52 (1982) 459;
A. Capella, J. Tran Thanh Van, Phys. Lett. B114 (1982) 450.

[43] G.C. Rossi and G. Veneziano, Nucl. Phys B123 (1977) 507.

[44] B.Z. Kopeliovich, B.G. Zakharov, Phys. Lett. B211, (1988) 221;
B.Z. Kopeliovich and B. Zakharov, Z. Phys. C43 (1989) 241.
B.Z. Kopeliovich, B. Povh, Phys. Lett. B446, (1999) 321.

[45] The BRAHMS Collaboration, "The BRAHMS Experiment at RHIC", Nucl. Instr. Meth. A499, 437 (2003)

[46] The STAR Collaboration, "STAR detector overview", Nucl. Instrum. Meth. A 499 (2003) 624

[47] The BRAHMS Collaboration, "Forward and midrapidity like-particle ratios from p+p collisions at $\sqrt{s}$ =200 GeV", Phys. Lett. B607, 42-50 (2005)

[48] S.E. Vance, M. Gyulassy, X.N. Wang, Phys. Lett. B 443 (1998) 45, nucl-th/9806008.

[49] C. Adler et al. (STAR Collaboration), "Midrapidity Antiproton-to-Proton Ratio from $Au+Au$ Collisions at $\sqrt{s_{NN}} = 130GeV$", Phys. Rev. Lett. 86, 4778â4782 (2001)

[50] The H1 Collaboration, "H1-Detector at HERA", Nucl. Instr. and Meth.A. 386, 1997, (in two parts: pages) 310 - 347 and 348 - 396)

[51] The H1 Collaboration, "Measurement of the Baryon-Antibaryon Asymmetry in Photoproduction at HERA", Submitted to the 29th Int. Conf. on High-Energy Phys. ICHEP98, Vancouver, Canada, July 1998. Abstract 556.

[52] The H1 Collaboration,"Strangeness Production at low Q^2 in Deep-Inelastic ep Scattering at HERA" Eur.Phys.J.C61 (2009) 185

[53] A.K. Aamodt et al. (ALICE Collaboration), "Midrapidity antiproton-to-proton ratio in pp collisions at $\sqrt{s}$ = 0.9 and 7 TeV measured by the ALICE experiment", Phys. Rev. Lett. **105** (2010) 072002

[54] A.B. Kaidalov, L.A. Ponomarev, K.A. Ter-Martirosyan, Sov. J. Nucl. Phys. 44, 468 (1986).

[55] C. Merino et al., Eur. Phys. J. C 54, 577 (2008); C. Merino, M.M. Ryzhinskiy, and Yu.M. Shabelski, arXiv:0906.2659.

[56] R. Aaij et al. (LHCb Collaboration) "Measurement of the $\bar{p}/p$ ratio in LHCb at s = 900 GeV and 7 TeV", CERN-LHCb-CONF-2010-009

[57] R. Aaij et al. (LHCb Collaboration) "Measurement of prompt $\overline{\Lambda^0}/\Lambda^0$ and $\overline{\Lambda^0}/K^0_s$ production ratios in inelastic non-diffractive pp collisions at $\sqrt{s}$ = 0.9 and 7 TeV", CERN-LHCb-CONF-2010-011

[58] B. I. Abelev et al. (STAR Collaboration), "Strange particle production in p-p collisions at $sqrts$=200 GeV", Phys. Rev. C 75, 064901 (2007)

[59] G.Aad et al. (The ATLAS Collaboration), "ATLAS Monte Carlo Tunes for MC09". ATL-PHYS-PUB-2010-002.

[60] S. Agostinelli et al.: "Geant4 - a simulation toolkit", Nuclear Instruments and Methods in Physics Research A 506 (2003) 250-303

[61] J.Podolansky and R.Armenteros, Phil.Mag. 45 (1954) 13

[62] K. Nakamura et al. (Particle Data Group), J. Phys. G 37, 075021 (2010)

[63] M.Aleksa et al.: "Measurement of the ATLAS solenoid magnetic field", 2008 JINST 3 P04003

[64] http://home.fnal.gov/ skands/leshouches-plots/

[65] S. van der Meer, CERN-ISR-PO-68-31, 1968.

[66] http://pdg.lbl.gov/2010/reviews/rpp2010-rev-monte-carlo-numbering.pdf

[67] W. Verkerke, D. Kirkby, "RooFit Users Manual", http://root.cern.ch/download/doc/RooFit_Users_Manual_2.91-33.pdf

[68] R. Brun et al. "GEANT3 User Guide", 1985, CERN459 Data Handling Division DD/EE/841

[69] G. Battistoni et al., "The FLUKA code: Description and benchmarking", AIP Conf. Proc. **896** (2007) 31.

[70] A. Ferrari, A. Fasso, J. Ranft, P.R. Sala, "FLUKA: a multi-particle transport code", CERN 2005-10 (2005), INFN/TC_05/11, SLAC-R-773

[71] T. Cornelissen et al., "Concepts, Design and Implementation of the ATLAS New Tracking (NEWT)", ATL-SOFT-PUB-2007-007, ATL-COM-SOFT-2007-002, Mar 2007.

Acknowledgments

With these few words i would like to thank all the people that, in different ways, have contributed to make all this possible. First of all I would like to thank my supervisor, prof. Anna Di Ciaccio, for her precious suggestions, support, ideas during these years and all the revision work of this thesis. I'm very grateful for her contagious enthusiasm for the research and for giving me the opportunity to join and work in a so exciting experiment.
I would like also to thank all the ATLAS Tor Vergata group, in particular Andrea and Giordano, for a lot of fruitful scientific discussions (and for the unforgettable raclette in Gruyere). A special thank is for Barbara, for her valuable advice since the beginning of the master thesis when I was moving my first step in the understanding of the RPC, her friendship, helpfulness and support throughout these years.
I would like to express my gratitude to Jed Biesiada, for the infinite stimulating discussions we had at CERN and all the suggestions for the work presented in this thesis. I'm very glad to have worked with him since this completely boosted my professional growth. Moreover I would like to acknowledge all the K^0_s *and* Λ^0 *Analysis* ATLAS working group and in particular Simona.
I would like to thank also all my dear friends, in particular Adriano, Barbara, Laura, Manuele, Francesco, Francesca, Antonio, Flavio, Gabriele, Marianna. Your friendship is very precious for me. I am also grateful to Elisa for helping me in my personal growth.
Last but not the least, I would like to express all my gratitude to my parents and my brother for their infinite love and encouragement.